REVMAT 2 (2026) 100230

Contents lists available at ScienceDirect

Review of Materials Research

journal homepage: www.sciencedirect.com/journal/review-of-materials-research

Comprehensive Survey

Magnesium-based hydrides and high-entropy alloys: A review of advancements and pathways for next-generation hydrogen storage materials

Joseph Dela Aziafor [a], Bongani Ramatsoma [b,c], Nihad Omer Hassan [d], Abdalrhaman Koko [e,f], Michael Bodunrin [b], Desmond Klenam [b,*]

[a] Department of Materials and Metallurgical Engineering, Kwame Nkrumah University of Science and Technology, Ghana
[b] Next Frontiers in Advanced Materials Laboratory, School of Chemical and Metallurgical Engineering, University of the Witwatersrand, Johannesburg, South Africa
[c] School of Chemical and Metallurgical Engineering, University of Johannesburg, South Africa
[d] Department of Petroleum Transportation and Refining Engineering, Sudan University of Science and Technology, Khartoum, Sudan
[e] Advanced Engineering Materials, National Physical Laboratory, Hampton Road, Teddington, TW110LW, United Kingdom
[f] Department of Materials, Royal School of Mines, Imperial College London, United Kingdom

A B S T R A C T

The increase in global emissions, primarily from the burning of fossil fuels, has created an urgent need for green energy solutions. Hydrogen holds significant promise as a clean energy alternative because of its potential to reduce greenhouse gas emissions. However, hydrogen storage remains a major hurdle that impedes its widespread use. This is because traditional high-pressure gas or cryogenic liquid storage methods are inefficient, bulky, and pose safety risks. Solid-state hydrogen storage using metal hydrides offers a safer and more compact alternative by chemically bonding hydrogen within the solid material. This allows for higher storage density at lower pressures and moderate temperatures. However, challenges with solid-state storage persist because of the difficulty in achieving onboard storage capacity and meeting practical requirements. Magnesium hydride (MgH_2) remains one of the most promising solid-state hydrogen storage materials, offering 7.6 wt. % gravimetric capacity. However, its high thermodynamic stability and slow sorption kinetics restrict practical application. This review presents a comprehensive and critically integrated analysis of strategies to overcome these limitations: alloying, catalytic doping, nanostructuring, metastable phase engineering, and destabilisation with complex hydrides. Mg-containing complex concentrated alloys (CCAs) and high-entropy alloys (HEAs) are examined as an emerging design paradigm that leverages configurational entropy to tune thermodynamic and kinetic properties. The roles of CALPHAD, density functional theory, and machine learning in accelerating alloy design are critically assessed. This review identifies both compositional and computational strategies as concrete pathways toward next-generation Mg-based hydrogen storage materials capable of meeting practical requirements.

1. Introduction

The increasing demand for clean energy is one of the most pressing challenges in the 21st century [1,2]. This is driven by the need to mitigate climate change and reduce dependency on fossil fuels, which remain the primary contributors to greenhouse gas emissions. The rise in the Earth's temperature has led to environmental and socio-economic consequences, including erratic weather patterns, melting ice caps, and rising sea levels. These impacts underscore the need to transition to clean energy alternatives [3]. Solar and wind energy play crucial roles in the just energy transition. However, they are insufficient for daily consumption demand and can sometimes be unreliable due to intermittent supply and storage issues [4]. These limitations highlight the need for complementary energy carriers that can ensure grid stability and meet variable energy demands.

Hydrogen, as an alternative energy source, is playing a crucial role in this transition. Hydrogen offers a clean, versatile, and high-gravimetric energy density alternative for various applications, including transportation, industrial processes, and grid-scale energy storage. Hydrogen stands at the forefront of renewable energy solutions, boasting a high gravimetric energy density of 120 MJ/kg, nearly three times that of gasoline. Moreover, hydrogen produces only water as a byproduct of combustion [5]. However, storage and delivery remain a critical setback impeding widespread adoption [6]. Conventional methods, such as compressed gas (40 g/L at 700 bar) and cryogenic liquid hydrogen (70.8 g/L at −253 °C), face intrinsic limitations in volumetric efficiency, high costs, and safety concerns [7]. In response to these issues, solid-state hydrogen storage, particularly through metal hydrides, has

* Corresponding author.
E-mail address: desmond.klenam@wits.ac.za (D. Klenam).

https://doi.org/10.1016/j.revmat.2026.100230
Received 6 March 2026; Received in revised form 1 June 2026; Accepted 6 June 2026
Available online 7 June 2026
3050-9130/© 2026 The Authors. Published by Elsevier B.V. on behalf of Chinese Materials Research Society. This is an open access article under the CC BY license (http://creativecommons.org/licenses/by/4.0/).

garnered increasing interest due to their ability to store hydrogen safely and compactly at moderate pressures, offering a viable alternative to conventional methods [8,9].

Solid-state hydrogen storage encompasses a range of materials and mechanisms, each with its own distinct advantages and limitations. Adsorbents such as metal-organic frameworks and carbon-based materials (e.g., nanotubes, MOFs, and COFs) store hydrogen via physisorption [10]. Hydrogen molecules adhere to their surfaces, allowing for operation near room temperature and low pressure, which facilitates safer storage. However, their hydrogen capacity is often inconsistent and insufficient for practical use. Chemical hydrides, such as ammonia borane, store hydrogen through chemical bonds and can achieve high storage capacities [11,12]. However, releasing hydrogen is typically irreversible or requires complex energy-intensive regeneration. Hydrogen can also be absorbed into metal or alloy structures to form metal hydrides. These metals can release hydrogen when needed, usually upon heating. They offer reversible storage methods with varying thermal requirements depending on the metal properties, processing route, and microstructure of the material. Frequently sought metal hydrides for solid-state hydrogen storage include, but are not limited to, $LiBH_4$ [13], $NaAlH_4$ [14,15], NaH [16], $FeTiH_2$ [17], and LiH [18].

Among the metal hydrides explored for solid-state hydrogen storage, magnesium hydride (MgH_2) has shown great promise for practical application. This is because of its high hydrogen storage capacity of 7.6 wt.% and a volumetric density of 110 g H_2/L [19], surpassing many competing hydrides, such as $LaNi_5$-based alloys or complex hydrides like $LiBH_4$. These properties align with the U.S. Department of Energy's targets for onboard hydrogen storage systems [20,21]. Magnesium is also known to be the eighth most abundant element in the Earth's crust (2.9% mass fraction), coupled with its low cost and environmental friendliness [22]. These remarkable qualities make MgH_2 an attractive candidate for large-scale deployment in both stationary and mobile applications. The strategic importance of MgH_2 is further emphasized by its role in the broader hydrogen economy, which is projected to account for 2-15% of global energy consumption by 2050 [23] (see Fig. 1 for graphical abstract).

Despite these advantages, MgH_2 faces significant hurdles that impede its widespread application. The reversibility of MgH_2 de/hydrogenation remains a challenge [24]. High desorption temperatures, sluggish hydrogen sorption kinetics, and thermodynamic stability pose challenges for practical applications in mobile and portable systems [19, 25]. The strong Mg–H ionic bonding results in a high decomposition enthalpy ($\Delta H \sim 74.7$ to 76 kJ/mol H_2). Hydrogen release requires temperatures above 300 °C [26]. The process is further hindered by slow H_2 dissociation on Mg surfaces with a high activation energy ($E_a = 160$ kJ/mol) and slow bulk diffusion ($D \sim 10^{-14}$ cm^2/s at 300 °C) [27].

To address the limitations of MgH_2 for hydrogen storage, recent research shows that nanostructuring MgH_2 to <5 nm crystallites via high-energy ball milling reduces interfacial energy barriers, lowering desorption temperatures to 200 °C with a 6.5 wt.% capacity [28,29]. Moreover, catalytic doping strategies demonstrate remarkable kinetic enhancements. A study by Vajo et al. demonstrates that adding MgH_2 to $LiBH_4$ reduces the de/hydrogenation enthalpy by 25 kJ/mol H_2 compared to pure $LiBH_4$. The mechanically milled $LiBH_4$ + ½MgH_2 composite can achieve a reversible capacity of 8–10 wt.% at temperatures ranging from 315 to 400 °C [30]. Yinghui Li and co-workers showed that doping with 2 mol% Ni nanoparticles decreases E_a to 60 kJ/mol, enabling 90% H_2 desorption within 2 min at 150 °C [29]. Additionally, alloying introduces electronic structure modifications that destabilize MgH_2. Ternary alloys of magnesium, such as $Mg_{85}Ni_{10}La_5$, have good reaction kinetics and favourable pressure–composition–temperature characteristics. The isotherms at 240–330 °C show a flat two-stage plateau with small hysteresis and a maximum H-capacity of ~4.6 wt.%, as shown in Fig. 2 [31].

Beyond conventional thermomechanical strategies, the high energy consumption required to drive MgH_2 dehydrogenation ($\Delta H \approx -74.5$ kJ/mol H_2, T_des >300 °C) represents a materials challenge and a system-level energy efficiency problem. Using electrical resistance heating as the sole energy input to drive dehydrogenation reduces the net energy output of the hydrogen storage system significantly. Solar-driven hydrogen storage has emerged as a promising approach to address this challenge by substituting concentrated solar irradiation for electrical heating. This is achieved by coupling the photothermal effect of light-absorbing catalytic additives with their thermochemical catalytic role to simultaneously supply heat and lower the activation energy for hydrogen release [32–36]. The concept was first demonstrated for $NaAlH_4$ using TiO_2@C composites that achieved complete hydrogen release under 10-sun irradiation [32], and has since been extended to MgH_2 through photothermal-catalytic co-functional materials including Cu@MXene composites [33], TiN@N-TiO2 microspheres [34], Mg2Ni (Cu) alloys formed by atomic reconstruction [35] and via

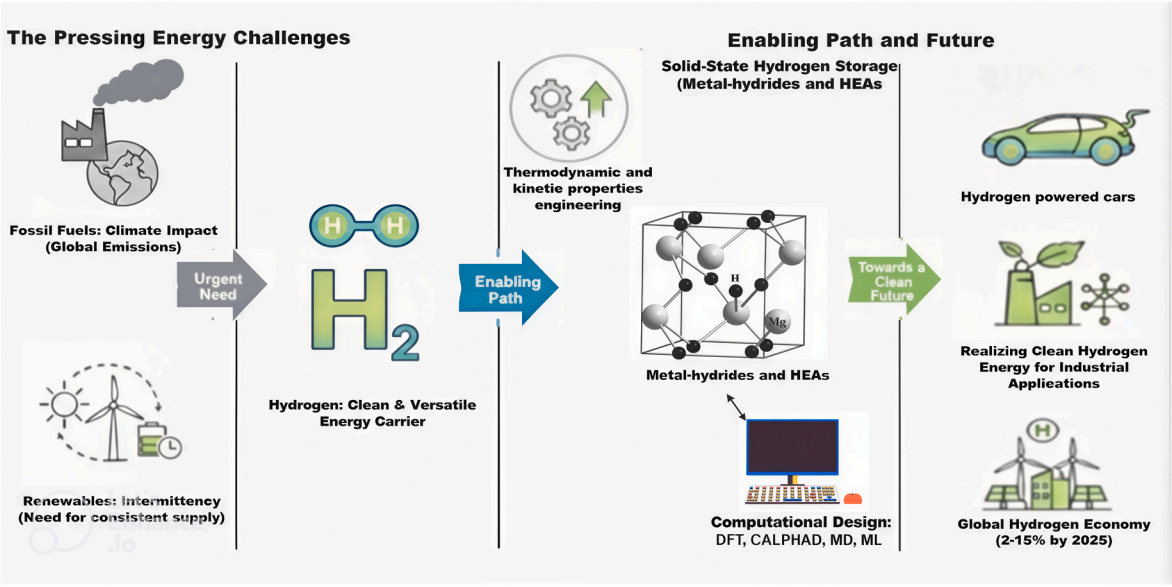


Fig. 1. Graphical abstract.

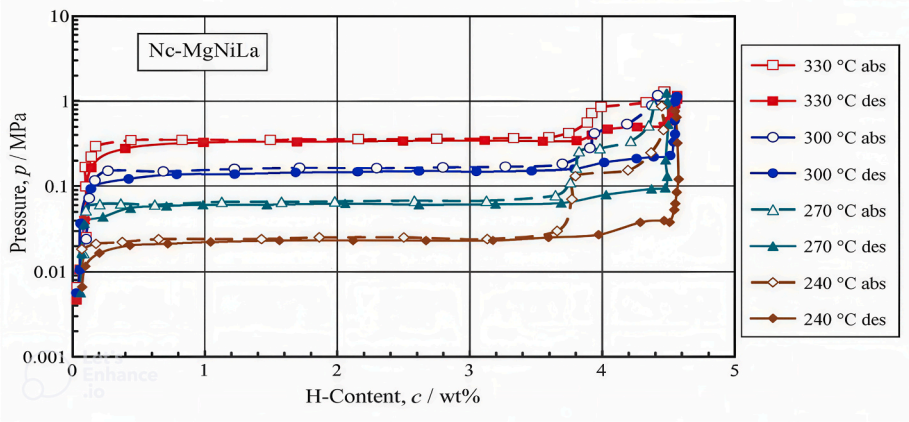


Fig. 2. Pressure-composition isotherms for Nc-MgNiLa alloy [31] (Reproduced with permission from Elsevier).

photogenerated vacancy-mediated destabilisation of complex borohydrides [36]. These advances are discussed in Section 3.5.

Furthermore, high-entropy alloys (HEAs), a novel class of multicomponent materials that leverage configurational entropy to stabilize single-phase structures, have been the focus of recent research. HEAs typically consist of five or more principal elements in near equiatomic ratios, resulting in unique microstructures and tunable properties for hydrogen storage applications [37,38]. HEAs offer several advantages compared with traditional MgH_2 and its binary or ternary derivatives. Although HEAs may exhibit slightly lower gravimetric hydrogen capacity than pure MgH_2, their superior kinetics, lower desorption temperatures, and excellent cycling stability make them highly attractive for practical hydrogen storage [39]. They are also excellent candidates for both mobile and stationary hydrogen storage applications due to their multicomponent design, which allows for targeted tuning of kinetic and thermodynamic properties. This design helps overcome the limitations of binary and ternary Mg-based hydrides.

Although several reviews treat Mg-based hydrides or HEAs for hydrogen storage in isolation, no prior work has systematically bridged these two subfields within a unified design framework. Specifically, the structural and thermodynamic principles that govern classical MgH_2 destabilisation, enthalpy tuning, catalytic doping, and nanoconfinement are not yet consistently applied as design rules in the growing HEA hydrogen storage literature. This review fills that gap by situating both material classes within a common analytical framework defined by the four central practical challenges of Mg-based hydrogen storage: high thermodynamic stability ($\Delta H \approx -74.5$ kJ/mol H_2), sluggish sorption kinetics, limited reversibility under real operating conditions, and degradation of capacity over cycling. Rather than cataloguing modification strategies in isolation, the sections that follow evaluate alloying, nanostructuring, metastable phase engineering, complex hydride destabilisation, and CCA/HEA design through the lens of how effectively each addresses these four challenges. In doing so, this review (i) establishes a common set of performance benchmarks across both material classes, (ii) extracts transferable design rules from classical Mg hydrides for application to Mg-containing HEAs and CCAs, and (iii) presents an integrated computational-experimental roadmap that treats CALPHAD, DFT, and machine learning as complementary rather than independent tools for alloy design.

2. Fundamental properties of magnesium-based hydrides

2.1. Microstructures of magnesium hydrides and HEAs

Pure Mg has a hexagonal close-packed (HCP) crystal structure [40]. When exposed to a hydrogen-rich environment, it initially forms the α-MgH_2 phase with a low hydrogen concentration. Upon subsequent hydrogenation under ambient conditions, this phase transforms into a tetragonal rutile structure (β-phase, P42/mnm, space group No. 136). In this β-phase, magnesium atoms are octahedrally coordinated by hydrogen atoms [41]. This occurs after a nucleation and growth stage. The rutile structure provides well-defined interstitial sites that are all occupied by hydrogen atoms, resulting in a high volumetric hydrogen density within the material [42,43]. At elevated temperatures and pressures (above 400 °C and 2.5 GPa), MgH_2 can further transform into a cubic γ-phase. However, this phase is less important for practical hydrogen storage. Further deformation at elevated temperature and pressure results in the formation of δ-MgH_2 phase (see Fig. 3) [44]. The strong ionic bond that exists between magnesium and hydrogen gives MgH_2 its high thermodynamic stability, even at elevated temperatures.

This strong Mg–H bond makes the dehydrogenation process challenging, as it requires breaking Mg–H bonds, migration of Mg and H, recombination of H atoms at the surface, and release of H_2 [45]. The nucleation and growth of Mg accompany the process of de/hydrogenation [46].

2.2. Intrinsic thermodynamic properties of MgH_2

The thermodynamics of hydrogen sorption in MgH_2 is governed by the reaction in Equation (1). This is a reversible reaction, with sorption being the forward process (hydrogen absorption or hydrogenation) and desorption the reverse (hydrogen release or dehydrogenation). Enthalpy (ΔH) measures the change in energy. For the formation of MgH_2, the enthalpy is approximately −74.5 to −75.2 kJ/mol H_2, indicating that it is an exothermic reaction and favours absorption at low temperatures [45,47]. Entropy (ΔS) measures the degree of disorder in a system. The entropy of MgH_2 is approximately -135 J/K/mol H_2 [47], reflecting the loss of translational entropy as H_2 gas is incorporated into the solid MgH_2 structure, affecting the equilibrium. These parameters affect the Gibbs free energy given by Equation (2t) which determines whether the reaction is spontaneous. For a reaction to be spontaneous, ΔG must be negative. At equilibrium, $\Delta G = 0$. The Gibbs free energy of formation (ΔG) is reported as −35.9 kJ/mol at standard conditions, further confirming the stability of MgH_2 at low temperatures. The relationship between temperature (T), pressure, and the equilibrium constant (K) is described by the van't Hoff equation (Equation (3)) where K is related to the partial pressure of hydrogen (PH_2) for gas-solid reactions, and R is the gas constant (8.314 J/mol·K). This equation links thermodynamics to PCT behaviour, which is crucial for understanding the performance of MgH_2.

$$Mg + H_2 \leftrightarrow MgH_2 \quad (1)$$

$$\Delta G = \Delta H - T\Delta S \quad (2)$$

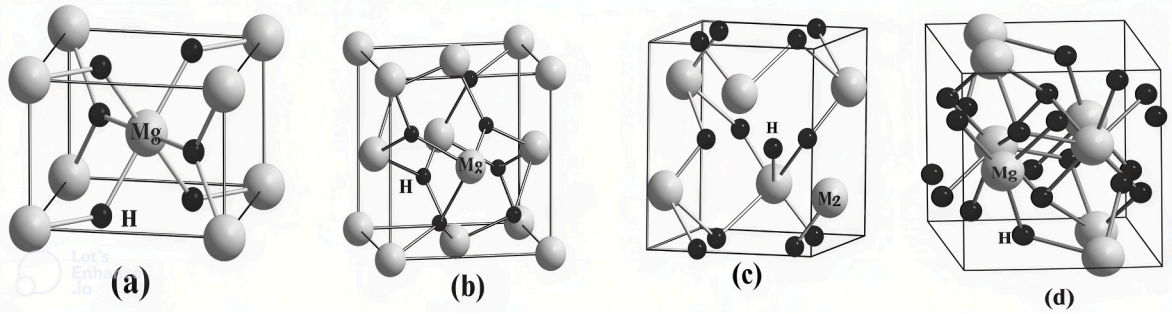


Fig. 3. Crystallographic unit cells of (a) α-MgH_2 (b) β-MgH_2, (c) γ-MgH_2 and (d) δ-MgH_2 showing sites occupied by hydrogen atoms.

$$\ln(K) = -\frac{\Delta H}{RT} + \frac{\Delta S}{R} \quad (3)$$

2.3. Kinetics and mechanism of sorption in MgH_2 and its derivative alloys

The steps for the hydrogen adsorption process in MgH_2 are outlined by Saeid and co-workers as follows: (I) Physisorption and the transport of hydrogen gas to surfaces, which involve the hydrogen adsorption onto the MgH_2 surface through the formation of Mg–H bonds or intermolecular forces; (II) Chemisorption and hydrogen dissociation on the MgH_2 surface; (III) Permeation and hydrogen diffusion into the α phase of MgH_2; and (IV) Growth and nucleation of the β phase of MgH_2 in the region of H_2 supersaturation [48]. Fig. 4 shows a schematic representation of the hydrogen absorption mechanism in MgH_2. The kinetics of hydrogen absorption and desorption in MgH_2 are limited by multiple factors, including diffusion barriers, activation energy, adsorption energy, surface dissociation, nucleation of hydride/metal phase, and chemical stability at every stage [47].

Absorption rates are generally faster than desorption due to the exothermic nature of absorption (ΔH is negative). The rate-limiting step for absorption is impeded by the high activation energy for hydrogen recombination at the surface [49]. The activation energy (E_a) for hydrogen desorption in bulk MgH_2 is ~140–160 kJ/mol [50]. This reflects the energy barrier for breaking Mg–H bonds and recombining H atoms into H_2 molecules. The absorption process involves dissociative chemisorption of H_2 into H atoms on the surface, followed by diffusion into the bulk material. The process typically occurs at a lower Ea of ~60–80 kJ/mol. The addition of catalysts, such as transition metals (Ni, Ti, Fe) or their oxides (Nb_2O_5, TiO_2), significantly reduces E_a. For instance, ball-milled MgH_2 with 5 wt.% Ni and 5 wt.% Nb_2O_5 exhibits a low desorption E_a for β-phase (68 kJ/mol) and γ-phase (74 kJ/mol), enabling faster hydrogen release at a lower temperature of 250 °C [51]. Carbon-based additives, like graphene, also enhance kinetics by improving surface reactivity and preventing particle agglomeration [52].

Alloying and nanostructuring also improve kinetics by reducing diffusion path lengths and increasing surface area. In a study by Zeng and coworkers [53], integrating 10 wt.% Ni_3S_2@C into MgH_2 significantly improved MgH_2's de/hydrogenation kinetics. The MgH_2-Ni_3S_2@C-4 nanocomposite absorbed 5.68 wt.% H_2 at 100 °C and released 6.35 wt.% H_2 at 275 °C. The composite's hydrogenation and dehydrogenation enthalpy values were 7.3 kJ/mol^{-1} and 11.0 kJ/mol^{-1}, respectively, lower than pure MgH_2 (−74.7 kJ/mol^{-1} and 76 kJ/mol^{-1}, respectively). This enhancement stems from the synergistic catalytic effect of the C, Mg_2Ni, and MgS phases formed during the initial cycle, resulting from reactions between Mg and Ni_3S_2. See Fig. 5 for the hydrogenation and dehydrogenation curves for the various MgH_2, MgH_2-C, MgH_2-Ni_3S_2, and MgH_2-Ni_3S_2@C composites.

Understanding these rate-limiting steps provides the mechanistic basis for interpreting the modification strategies reviewed in Section 3. Strategies that primarily target surface H_2 dissociation, such as transition-metal catalytic doping, reduce the activation energy for step (II) without substantially altering the bulk diffusion barrier of step (III). Nanostructuring strategies reduce particle and grain size. This compresses diffusion distances in step (III) and increases the density of nucleation sites in step (IV), but leaves the intrinsic Mg–H bond strength unchanged. Structural destabilisation strategies modify the electronic

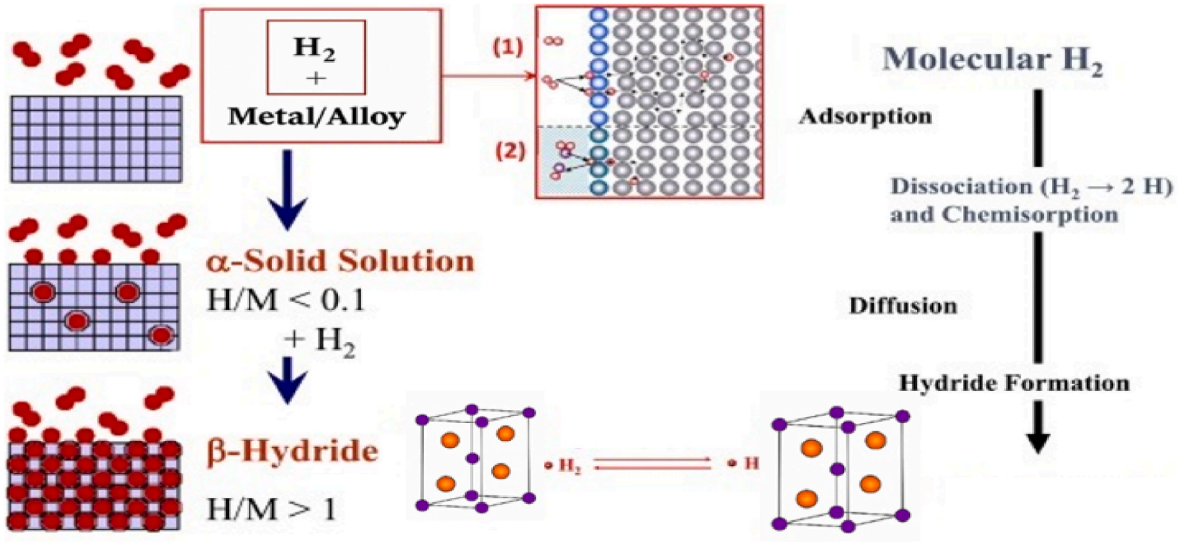


Fig. 4. Schematic diagram of hydrogen absorption mechanism in MgH_2.

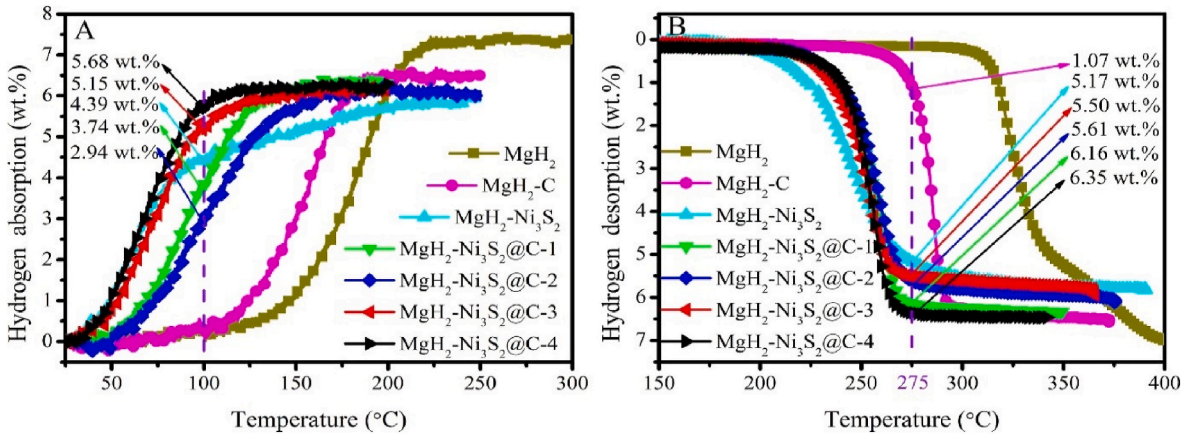


Fig. 5. (A) Hydrogenation and (B) dehydrogenation curves of MgH_2, MgH_2-C, MgH_2-Ni_3S_2, and MgH_2-Ni_3S_2@C composites [53] (Reproduced with permission from Elsevier under Open Access CC BY-NC-ND 4.0).

structure of the Mg–H bond through alloying with Pd, Rh, In, or Ba. This approach directly reduces the energy of step (IV) by lowering the formation enthalpy of the hydride phase. Composite and interface engineering strategies operate across all four steps simultaneously, which is the mechanistic explanation for their consistently superior performance relative to single-strategy approaches.

2.4. Microstructures and phases of HEAs

High-entropy alloys can exist in various microstructures and phases, including body-centered cubic (BCC), face-centered cubic (FCC), intermetallic structures, Laves phases, and multiphase structures. Researchers generally aim to develop HEAs with a single-phase microstructure that can reversibly transform during repeated cycles of hydrogen absorption and desorption. The formation of multiple phases and disproportionation (phase segregation) tends to limit the hydrogen storage capacity. Among these, BCC structures are most favoured for hydrogen storage due to their open lattice framework and larger interstitial sites, allowing for easier hydrogen diffusion and higher storage capacities. HEAs with a BCC matrix generally exhibit faster kinetics and higher reversible hydrogen uptake compared to FCC and multiphase alloys. Examples such as TiVZrNbTa [54], TiVZrNb [55], TiVZrNbHf [56] undergo a single-step, reversible transition from BCC structures into likely BCT/FCC dihydrides. These alloys have shown good reversibility and viability for practical use. FCC phases generally provide denser lattices. Certain TiVNbCr-M (M = Fe, Mn, Ni) HEA systems show phase transformations of BCC to FCC through a pseudo-BCC structure [57].

Although single-phase BCC HEAs are preferred, certain intermetallic structures such as C-14 Laves phases found in CoFeMnTiVZr [58], ZrTiVCrFeNi [59], and TiZrCrMnFeNi [60] show promise for hydrogen storage. These Laves phases maintain their structure after de/hydrogenation cycles, with a slight variation in lattice constant due to the hydrogen retention effect. This stability and ability to accommodate hydrogen are suitable for hydrogen storage applications. This explains the interest in Laves phases despite the general preference for single-phase BCC alloys [60].

2.5. Kinetics and mechanism of sorption in HEAs

The hydrogen sorption mechanism in HEAs is similar to that of traditional Mg-based hydrides. The process has been described by Marques et al. [61] as follows: (I) Surface activation, which involves the adsorption of hydrogen molecules onto the alloy surface, followed by dissociation into atomic hydrogen. This step is influenced by factors such as surface area, grain boundaries, and oxidation state [62]. (II) Diffusion of atomic hydrogen into the alloy's lattice, occupying interstitial sites. Lattice defects and strain fields influence the diffusion rate. (III) Hydride begins to form once a critical concentration is reached. Hydrogen forms stable hydride phases. In BCC HEAs, hydrogen can occupy both tetrahedral and octahedral sites, leading to high H/M ratios (up to 2.5). (IV) Desorption: hydrogen is released upon heating the alloy or upon pressure reduction. The desorption temperature and activation energy depend on alloy composition and phase stability. The phase stability in HEAs is governed by a complex interplay of valence electron concentration (VEC), atomic size mismatch (δr), electronegativity mismatch, and thermodynamic parameters (ΔHm, ΔSm), as well as kinetic and temperature factors [63]. For example, a lower VEC (<7.6) is a critical design guideline for destabilizing hydrides, thereby lowering the hydrogen desorption temperature and enhancing reversible hydrogen storage.

The rate of hydrogen absorption in HEAs is faster than the rate of desorption. HEAs often contain multiple transition metals (e.g., Ti, V, Nb, Cr), which serve as catalytic sites for the rapid dissociation of H_2. This step is typically fast and exothermic, meaning it releases energy and proceeds readily. Moreover, HEAs, especially those of BCC structures, have open lattice channels and more interstitial sites than FCC structures. These interstitial sites facilitate hydrogen diffusion. Lattice distortion and atomic size mismatch provide more room for hydrogen atoms. The presence of hydride-forming elements in HEAs facilitates the absorption rate. In contrast, the desorption rate is usually slower because it involves the breaking of bonds between the H atoms and the metallic elements. This is an endothermic process and requires energy input (usually heat) to overcome the energy barrier. Moreover, the rate-determining step is dependent on the bulk diffusion of H atoms out of the alloy, especially if the alloy undergoes structural changes during cycling (e.g., phase transformation, nucleation, or grain growth). Surface oxidation and contamination can further impede recombination and release.

2.6. Mg-containing complex concentrated alloys

Mg has a low atomic mass and forms magnesium hydride, which has a high hydrogen storage capacity. Replacing heavier transition metals in HEAs with Mg typically increases the gravimetric (weight-based) hydrogen storage of the alloy. However, studies show that substituting transition metals with Mg can compromise the ease and speed of hydrogen release. This is because Mg forms a very stable hydride, making it more difficult to release hydrogen at moderate temperatures and slowing desorption kinetics. $Mg_{0.10}Ti_{0.30}V_{0.25}Zr_{0.10}Nb_{0.25}$ alloy adopts a single-phase BCC lattice and can absorb hydrogen within 1 min at room temperature, forming a hydride phase with 1.7 H/M (2.7 wt.%)

capacity [64]. MgH_2-40 wt.% TiCrMnFeZr HEA can absorb and desorb 0.72 wt.% H_2 even at room temperature [65]. In addition, $Mg_{10}Ti_{30}V_{25}Zr_{10}Nb_{25}$ HEA prepared by mechanical alloying exhibited excellent absorption kinetics at room temperature, while the hydrogen absorption capacity is about 1.196 wt.% [65]. Zr_2MgV_2CrNi and $Zr_2MgVFeCrNi$ HEAs can rapidly absorb 0.8 wt.% (0.43 H/M) and 0.9 wt.% (0.48 H/M) hydrogen at room temperature, respectively, three times higher than those of the Zr-based alloys without Mg-substitution. More importantly, the absorbed hydrogen of Zr_2MgV_2CrNi and $Zr_2MgVFeCrNi$ HEAs can be partially released at room temperature with distinct desorption processes [66]. These results indicate a trade-off between hydrogen storage capacity and kinetics when comparing HEAs with conventional MgH_2 and its derivative alloys. However, recent studies on HEAs have focused on enhancing the storage capacity, kinetics, and thermodynamics to enable rapid absorption rates even at room temperature, and enable desorption at lower temperature within shorter times.

The hydrogen storage behaviour of Mg-containing HEAs is governed by three interacting effects that have no direct analogue in binary or ternary Mg-based hydrides. First, the configurational entropy of the multi-principal-element lattice stabilizes the solid-solution phase against disproportionation during cycling. This provides an intrinsic structural resilience that nanostructured MgH_2 composites must engineer artificially through confinement matrices. Second, the heterogeneous local chemical environment arising from the coexistence of multiple elements with different hydrogen affinities distributes hydrogen binding energies across a continuous spectrum of interstitial sites. This results in the characteristically sloped PCT isotherms that reflect a more flexible thermodynamic landscape than the flat plateaus of classical Mg hydrides. Third, the intermediate ΔH values of Mg-containing HEAs (−35 to −59 kJ/mol H_2) arise from a balance between Mg's strong hydride-forming tendency and the electronic and strain effects of surrounding TM neighbours. This balance can be tuned through compositional adjustment without the sharp capacity penalties associated with increasing alloying element content in binary MgH_2 systems. These three effects collectively define the design space of Mg-containing HEAs as qualitatively distinct from modified MgH_2, and justify their treatment as a genuinely new design paradigm rather than simply an extension of classical alloying strategies.

3. Modification of thermodynamic and kinetic properties of Mg-based hydrides and their derivatives

The strategies examined in this section address the four central challenges of Mg-based hydrogen storage to varying degrees. Alloying and metastable phase engineering primarily target thermodynamic stability by modifying the Mg–H bond enthalpy, while nanostructuring and composite design predominantly address kinetic barriers and cycling durability through surface area enhancement, diffusion pathway shortening, and particle coarsening resistance.

3.1. Alloying

Alloying is the most direct thermodynamic intervention for MgH_2 because it introduces elements that form less stable hydrides or modify the electronic structure of the Mg–H bond. Alloying strategies aim to reduce the desorption enthalpy below the −74.5 kJ/mol H_2 baseline for pure MgH_2 and, secondarily, to improve sorption kinetics through catalytic transition metal additions. AB_5 and AB_2 intermetallic hydrides represent the classical precursors to this strategy. AB_5 hydrides (e.g., $LaNi_5$, $LaNi_{4.7}Co_{0.3}$) offer fast, reversible hydrogen absorption and desorption at near-ambient conditions, excellent cycling stability, and moderate storage capacity (~1.5–2 wt.%), for low-pressure and safe hydrogen storage applications [67]. AB_2 hydrides often crystallize in Laves phases, providing high hydrogen storage densities and fast kinetics, capable of rapid uptake and release within minutes over a broader pressure range, though sometimes challenged by surface passivation [68]. Ti-Mn-based AB_2-type hydrogen storage alloys are a promising solid-state hydrogen storage material, offering good de/hydriding kinetics, high storage capacity, and relatively low cost [69]. However, their practical applications are hindered by critical drawbacks, notably the high plateau pressure required for hydrogen absorption and desorption. Fundamental knowledge of AB_5 and AB_2 hydrides and the ongoing advances in Mg-based alloying represent critical pathways forward in the development of efficient, safe, and high-performance hydrogen storage systems.

Beyond these classical intermetallics, Mg-based alloying strategies can be organized around three primary mechanisms: (i) catalytic enhancement of surface reactions, where transition metal additions provide active sites that lower the activation energy for H_2 dissociation without substantially modifying the Mg–H bond enthalpy; (ii) thermodynamic destabilisation of the Mg–H bond, where specific alloying elements directly weaken Mg–H bonding through structural or electronic modification, reducing the desorption enthalpy; and (iii) microstructural engineering of diffusion pathways, where multi-element alloys generate secondary phases and grain boundary networks that shorten hydrogen diffusion distances and increase nucleation density. In practice, the most effective systems combine two or more of these mechanisms simultaneously, as discussed below.

Subgroup 1: Catalytic effects: The most extensively studied alloying strategy exploits transition metals as surface catalysts for H_2 dissociation. Ni, Ti, and Co each function through distinct but related mechanisms [70,71]. This is accomplished by adjusting the reaction enthalpy through the introduction of elements that form less stable hydrides than MgH_2 [72]. The alloying process can be achieved through various mechanical alloying techniques, including high-energy ball milling, reactive ball milling, arc melting, and induction melting.

Mg_2Ni, prepared by ball milling, achieves 3.5 wt.% capacity with a desorption Ea of ~100 kJ/mol at ~250 °C. The kinetic improvement arises from Ni's partially filled d-orbitals, which lower the dissociation barrier for H_2 at the alloy surface [73]. The MgH_2–Ti system operates through an in-situ catalytic species: during ball milling, elemental Ti reacts with MgH_2 to form active $TiH_{1.971}$, which drives desorption and reduces Ea from 161.3 to 103.9 kJ/mol, a 35.8% reduction, while preserving a capacity of 6.18 wt.% [74]. The $Mg_{10}Co$ system similarly benefits from in-situ phase formation, with Mg_2CoH_5 and $Mg_6Co_2H_{11}$ providing lower absorption plateaus that accelerate kinetics at 350 °C (5.93 wt.% absorbed in 5 min, Ea = 124.89 kJ/mol). Across these binary systems, the common pattern is clear: catalytic TM additions substantially reduce Ea and modestly lower T_des, but leave the fundamental Mg–H bond enthalpy largely unchanged. This means thermodynamic stability remains a challenge even when kinetics are well optimized [75].

A systematic review by Ding et al. [76] benchmarked nano-engineering and catalysis strategies across a broad range of MgH_2 systems, demonstrating that combined approaches consistently outperform single-variable interventions and identifying bidirectional catalysts and nanoconfinement with in-situ catalysis as the most promising near-term directions for achieving hydrogen release at lower temperatures with improved cycle stability.

Subgroup 2: Thermodynamic destabilisation of the Mg–H bond: A more direct attack on the thermodynamic stability challenge comes from elements that structurally or electronically modify the Mg–H bond itself rather than acting as surface catalysts. The clearest example is the rutile-to-fluorite structural transition induced by alloying MgH_2 with Ba or transition metals (Sc, Ti, Y): at approximately 20 at% TM or 40 at% Ba, the fluorite phase $Mg_{0.5}Ba_{0.5}H_2$ forms with a formation enthalpy higher than pure rutile MgH_2, lowering the equilibrium desorption temperature at atmospheric pressure [77]. Noble metals Pd and Rh represent the most thermodynamically aggressive destabilizers reported in this section, forming alloys with exothermic dehydrogenation enthalpies that fundamentally alter the reaction energy landscape [78].

Indium achieves a related effect through a different mechanism and increases the equilibrium H_2 pressure over the composite and weakens the Mg–H bond electronically, producing measurably lower T_des and higher desorption driving force [79]. Solid solutions of the form Mg-A (A = Group II, III, IV, post-transition, or noble elements) operate through lattice strain and electronic perturbation that destabilize the rutile MgH_2 structure more broadly [78]. This group of strategies is the most thermodynamically targeted in Section 3.1 and represents the clearest path to reducing ΔH; however, kinetic and cycling data for these systems remain the least frequently reported, constituting a significant evidence gap.

Subgroup 3: Improved diffusion pathways through multi-element phase engineering: Ternary and quaternary alloys introduce a third mechanism: the deliberate engineering of secondary phases and microstructural features that improve hydrogen diffusion and nucleation kinetics without relying solely on a single catalytic element. The $AlMg_2TiZn$ multi-principal-element alloy, prepared by high-energy ball milling, achieves Ea = 148 ± 1 kJ/mol with a capacity of 1.35–1.4 wt.% H_2. The Ea reduction relative to pure Mg arises from a distribution of diffusion channels across multiple grain boundary networks and secondary phases rather than from a single dominant catalytic species [80]. $Mg_{93}Ni_{7-x}Si_x$ alloys (x = 0.4, 1.6, 5) were prepared via arc melting followed by ball milling. The alloys exhibited enhanced hydrogen storage due to a synergistic effect of Ni and Si. The optimal $Mg_{93}Ni_3Si_5$ alloy system illustrates how this mechanism can be combined with catalytic effects to particularly good effect: Mg_2Si precipitation and refined Mg_2Ni_3Si phases create nucleation sites and diffusion channels (improved diffusion pathway mechanism), while Ni simultaneously catalyzes H_2 dissociation (catalytic mechanism). The combined effect results in a dehydrogenation onset at 180 °C with Ea = 105.21 kJ/mol [81]. This dual-mechanism character of the best-performing ternary systems confirms that the three mechanistic categories are not mutually exclusive, and that compositionally targeted multi-element alloys designed to exploit two or more mechanisms simultaneously represent the most effective direction for alloying-based Mg–H storage improvement.

The catalytic and microstructural roles of rare-earth doping in reconfiguring hydrogen diffusion pathways have been further elucidated by a recent multiscale experimental-theoretical study on Mg–Ni–Er ternary alloys [82]. Er preferentially partitions into the Mg_2Ni phase rather than the α-Mg matrix, reducing the hydrogen diffusion barrier from 0.505 eV in pure Mg to 0.278 eV in ErH_2-doped Mg as confirmed by first-principles calculations, with the Mg-7.8Ni-2.2Er alloy achieving 6.15 wt.% absorption capacity at 300 °C. This demonstrates that targeted rare-earth additions can simultaneously modify intermetallic phase architecture and hydrogen diffusion kinetics without sacrificing gravimetric capacity.

Alloying plays a critical role in MgH_2-based hydrogen storage materials by reducing decomposition temperatures and enhancing kinetics. Nevertheless, challenges remain, including that some alloys still require high temperatures and face capacity trade-offs. The future lies in carefully tailoring multi-element blends to strike a balance between speed,

Table 1
Comparison of Alloying Strategies for Mg-Based Hydrogen Storage (Effects of alloying strategy on thermodynamic stability, sorption kinetics, and cycling durability).

Alloying Strategy	Representative System	Capacity (wt.%)	T_{des} (°C)	Ea (kJ/mol)	Thermodynamic Effect	Kinetic Effect	Cycling Stability	Ref
AB_5 Intermetallic	$LaNi_5$, $LaNi_{4.7}Co_{0.3}$	1.5–2.0	Near-ambient	Not reported	Well-tuned; low desorption enthalpy; operates near room temperature	Excellent; fast reversible absorption and desorption	Excellent — field benchmark for durability	[67]
AB_2 Intermetallic (Laves phase)	Ti-Mn Laves phase	High (not reported)	Moderate	Not reported	Acceptable; limited by high plateau pressure for absorption and desorption	Fast; uptake and release within minutes over broad pressure range	Moderate; surface passivation limits long-term durability	[64] [69]
Binary TM — Ni	Mg_2Ni (ball milled)	3.5	~250	~100	Moderate; complex anion $[NiH_4]^{4-}$ formation reduces enthalpy	Strong; Ni catalyzes H_2 dissociation at surface	Good; intermetallic phase resists coarsening	[73]
Binary TM — Ti	MgH_2–Ti (ball milled)	6.18	~257	103.9 (↓ from 161.3)	Modest; T_{aes} lowered by 51 °C; limited enthalpy reduction	Strong; ~36% Ea reduction via active $TiH_{1.971}$ species driving desorption	Not reported	[74]
Binary TM - Co	$Mg_{10}Co$ (mechanical alloying)	5.93	350 (absorption)	124.89	Moderate; lower absorption plateau via Mg_2CoH_5 and $Mg_6Co_2H_{11}$ formation	Improved absorption rate; desorption kinetics less well characterized	Not reported	[75]
Quaternary: Multi-principal	$AlMg_2TiZn$ (ball milled)	1.35–1.40	Not reported	148 ± 1	Limited; Ea still high relative to binary TM systems despite multi-element design	Moderate improvement over pure Mg; no synergistic catalytic effect identified	Not reported	[80]
Ternary - Ni + Si	$Mg_{93}Ni_3Si_5$ (arc melting + ball milling)	Not reported	Onset 180	105.21	Good; Mg_2Si precipitation and eutectic structures lower T_{aes} significantly	Strong; Ni catalyzes H_2 dissociation; eutectic phases create nucleation sites and diffusion channels	Not reported	[81]
Structural Destabilisation - Fluorite transition	$Mg_{0.5}Ba_{0.5}H_2$ (rutile → fluorite)	Not reported	Below pure MgH_2	Not reported	Direct; structural transition raises formation enthalpy, lowering T_{aes} at atmospheric pressure	Indirect benefit from modified phase structure; not quantified	Not reported	[77]
Structural Destabilisation - Noble metals	MgH_2 + Pd, Rh	Not reported	Not reported	Not reported	Strong; exothermic dehydrogenation enthalpies — most direct enthalpy reduction reported in this section	Not quantified	Not reported	[78]
Structural Destabilisation — Post-transition metal	MgH_2 + In	Not reported	Lower than pure MgH_2	Not reported	Clear; higher equilibrium H_2 pressure and direct Mg–H bond weakening	Indirect benefit from increased thermodynamic driving pressure	Not reported	[79]

Note: T_{aes} = desorption temperature; Ea = activation energy for dehydrogenation unless stated otherwise (abs. = absorption, des. = desorption).

stability, and storage density for practical applications. Table 1 shows a comparison of alloying strategies.

The TM-based binary alloys improve kinetics through catalytic H_2 dissociation and active hydride phase formation. Thermodynamic gains are real but partial. AB_5 and AB_2 systems demonstrate that thermodynamic tuning and kinetic performance can be simultaneously achieved, but only at the cost of gravimetric capacity. They serve as the design baseline that Mg-based alloys must exceed. Ternary and quaternary alloys outperform binary systems by combining catalytic and destabilisation roles across multiple elements simultaneously. However, capacity remains compromised and cycling stability data are largely absent from these studies. Structural destabilisation strategies are the most thermodynamically targeted interventions in this section. They act on the Mg–H bond directly rather than through surface catalysis, making them the most promising route for genuine enthalpy reduction. However, kinetic and cycling data for these systems are consistently absent, a critical gap for future study.

3.2. Nanostructuring

Nanostructuring targets the kinetic challenge primarily: by reducing particle, crystallite, and grain size, it shortens hydrogen diffusion pathways, multiplies active surface sites, and increases grain boundary density, lowering the activation energy for dehydrogenation. Importantly, nanostructuring also confers a secondary thermodynamic benefit through surface energy destabilisation of the Mg–H bond, though this effect diminishes as particles coarsen during cycling, linking kinetic and durability challenges directly [83]. Reducing the particle, crystal, and grain size leads to a significant increase in surface area, which accelerates hydrogen diffusion and increases the number of active sites for hydrogen adsorption and desorption [84]. The high surface energy of nanosized MgH_2 destabilizes the strong Mg–H bonds, lowering the decomposition enthalpy and facilitating hydrogen release at lower temperatures. Additionally, the abundance of grain boundaries in nanostructured materials provides more pathways for hydrogen diffusion, while the shortened diffusion distances in smaller crystals and grains enhance the overall reaction rates [85].

It is important to distinguish between the effects of particle size, crystal size, and grain size, as each uniquely influences the hydrogen storage behaviour. Particle size affects the surface area-to-volume ratio, crystal size impacts nucleation and phase growth, and grain size relates to the polycrystalline structure and diffusion efficiency [84]. Various synthesis methods, such as ball milling, vapor deposition, plasma metal reduction, chemical reduction, and nanoconfinement techniques, are employed to produce nanosized MgH_2 with tailored structures [86,87]. These nanostructuring techniques enhance hydrogen absorption/desorption kinetics while also contributing to a reduction in thermodynamic stability, making MgH_2 a more viable material for future energy storage applications.

Mg-based materials' hydrogen storage properties can be enhanced by forming core-shell nanostructures. The catalytic atoms at the core-shell nanostructure interface can react with or alter the electronic structure of the adjacent magnesium atoms, creating numerous active sites that accelerate the dissociation, transport, and recombination of hydrogen atoms. Furthermore, during the thermal hydrogen storage process, the shell structure can act as a barrier to stop the oxidation and agglomeration of micro-Mg/MgH_2. The Fe-covered core-shell nanostructured composites (Mg@Fe) show a lower absorption activation energy of 54.6 kJ mol^{-1} H_2 and the hydrogenation enthalpy of −78 kJ mol^{-1} H_2. In contrast to pure magnesium powder, the Mg@Fe nanostructure exhibits a decreased hydrogen absorption activation energy of 54.6 kJ/mol H_2 at 347 °C. The catalytic effects of nano α-Fe covering on the Mg ultrafine particles were responsible for the enhanced hydrogen sorption kinetic properties of the composite [88].

A core-shell nanostructured Mg@Pt composite, consisting of many icosahedral Mg particles as the core with nano-sized Pt particles distributed homogeneously on different surfaces, was synthesized through an arc plasma method followed by the generic solid-state method [89]. The Pt on Mg particles demonstrated a "spillover" effect that enhanced the early stages of hydrogen absorption kinetics and reduced the dehydrogenation temperature compared to pure MgH_2. Similarly, Mg-PMMA core-shell composite was produced by nano-confining Mg in PMMA, which permits hydrogen to flow through while blocking oxygen and water molecules. The hydrogen absorption and desorption capabilities of the alloys were then investigated. Microstructural studies revealed that Mg particles had an average diameter of 5 nm. The material exhibited a rapid rate of hydrogen absorption, achieving a reversible cycle at 200 °C, and could absorb 4 wt.% H_2 within 30 min. PMMA could simultaneously maintain the hydrogen storage capacity and effectively prevent the oxidation and agglomeration of Mg/MgH_2 [90].

Porous carbon nanostructures also improve hydrogen storage properties by enhancing diffusion in MgH_2-C systems. For example, Nielsen et al. [91] investigated the kinetics of hydrogen uptake and release by embedding MgH_2 nanoparticles in nanoporous carbon aerogel scaffolds. Sieverts' measurements and thermal desorption spectroscopy were used to investigate the hydrogen storage characteristics of nanoconfined MgH_2. The results showed that the confined hydride's dehydrogenation kinetics are dependent on the scaffold material's pore size distribution; that is, smaller pores facilitated faster desorption rates, potentially due to the confined magnesium hydride's size reduction.

Carbon nanotubes (CNTs) enhance hydrogen storage capacity and lower desorption temperatures. These improvements arise from the formation of thousands of 10-50 nm grains in Mg nanoparticles, thereby creating diffusion channels to drive hydrogen diffusion. Moreover, a synergistic effect is observed when catalytic species are incorporated [92]. For instance, Chen and coworkers [93] synthesized carbon-encapsulated ZrO_2 (5–10 nm) nanoparticles (ZrO_2/C) which acted as a catalyst in MgH_2–ZrO_2/C. The nanostructure exhibits a reduced onset operating temperature of 208 °C, which is significantly lower than that of undoped MgH_2 (309 °C).

Kinetic enhancement of Mg-based materials was achieved through a synergistic effect of carbon shells that prevent particle aggregation and nonstoichiometric TiCx, which catalyzed H_2 dissociation for rapid H_2 sorption. A TiC_x-decorated Mg nanoparticle composite confined in 2–3 nm carbon shells was synthesized via reactive gas evaporation, achieving controlled particle sizes (<50 nm). The optimal $Mg_{88}(TiC_{0.6})_{12}$@C (88% Mg loading) demonstrated superior hydrogen storage: 5.5 wt.% H_2 absorption in 25 min at 250 °C and 4.5 wt.% H_2 desorption in 60 min at 300 °C, with stable performance over 10 cycles [94]. Building on these confinement strategies, Ding et al. [95] have identified spatially programmed confinement catalysis as an emerging design paradigm that goes beyond conventional catalytic doping by engineering the local reaction environment of MgH_2 at multiple length scales simultaneously. This demonstrates that the dimensionality of confinement geometry (1D axial, 2D interlayer, or 3D porous frameworks) is itself a critical determinant of interfacial catalytic performance [95].

MOF scaffolds enhance the hydrogen storage properties of MgH_2. The diffusion path of hydrogen can be significantly shortened when Mg nanoparticles are confined inside a scaffold with fine porosity. This improves the thermodynamics, kinetics, and reversibility of hydrogen storage. The incorporation of MOFs introduces numerous defects, forming specific interactions between Mg–H bonds. MOFs can provide a balance between high storage capacity and low operating temperatures [92]. For instance, a core-shell Mg/ZIF-67 nanostructured composite reduced the dehydrogenation Ea by 43.2 kJ/mol compared to pure Mg. Only 44% of the hydrogen in Mg was liberated when the hydrogen adsorbed by Mg/ZIF-67 was fully released at 338 °C. Even after 100 cycles, the hydrogen capacity of the Mg/ZIF-67 composites remained unchanged [96]. Jia and coworkers used in situ bottom-up reduction of Ni-MOF-74 precursor to create ultrafine (2-3 nm) metallic Ni

nanoparticles incorporated in a crushed MgH_2 matrix. The composite absorbed 6.2 wt.% hydrogen in 30 s at a low temperature of 150 °C and completely released hydrogen in 20 min at 300 °C [97]. Furthermore, TMA-TM MOF (TM = Co, Fe) was prepared by Ma et al. [98] using trimesic acid. The MgH_2-Fe-MOF's activation energy for hydrogenation decreased to 66.8 kJ/mol H_2 after ball-milling with MgH_2. Additionally, the MgH_2-Fe-MOF composite shows a dehydrogenation Ea of 142.3 kJ/mol H_2, which is lower than that of pure MgH_2.

A comprehensive framework for understanding these multi-scale interface effects has been provided by Jiang et al. [99], who established that atomic-scale control of metal–metal interfaces and engineered mass transport channels, spanning 1D confined channels, 2D catalytic platforms, and 3D porous networks, can simultaneously address both kinetic and thermodynamic limitations in Mg-based systems, extending the design logic from core-shell composites to the full dimensional spectrum of confinement architectures [99].

Taken together, the nanostructuring and confinement strategies reviewed above consistently reduce the apparent activation energy for dehydrogenation from ~160 kJ/mol toward 60–90 kJ/mol, with the most effective systems combining particle size reduction below 20 nm with catalytic surface decoration. However, these kinetic gains come with persistent trade-offs: thermodynamic stability is only marginally

Table 2
Comparison of Nanostructuring Strategies for Mg-Based Hydrogen Storage (Assessing the effect of nanostructuring approach on thermodynamic stability, sorption kinetics, and cycling durability).

Nanostructuring Strategy	Representative System	Capacity (wt.%)	T_{des} (°C)	Ea (kJ/mol)	Thermodynamic Effect	Kinetic Effect	Cycling Stability	Ref
Core-shell - Metal coating	Mg@Fe (nano α-Fe shell)	Not reported	347 (absorption)	54.6 (absorption)	Modest; hydrogenation enthalpy −78 kJ/mol H_2 — marginal thermodynamic change from pure MgH_2	Strong; Fe shell creates active catalytic sites accelerating H_2 dissociation, transport, and recombination	Shell prevents oxidation and agglomeration of Mg particles; long-term cycling not quantified	[88]
Core-shell - Noble metal coating	Mg@Pt (arc plasma method)	Not reported	Lower than pure MgH_2	Not reported	Secondary; T_{aes} reduced relative to pure MgH_2 via Pt-induced surface modification	Strong early-stage absorption kinetics via Pt spillover effect; H_2 dissociation accelerated at Pt sites	Not reported	[89]
Core-shell - Polymer confinement	Mg@PMMA (5 nm Mg particles)	4.0	200 (reversible cycle)	Not reported	Moderate; 5 nm particle size lowers T_{aes} via surface energy destabilisation of Mg–H bond	Fast absorption; 4 wt. % H_2 absorbed within 30 min at 200 °C; PMMA shell permits H_2 diffusion while blocking O_2 and H_2O	Good; PMMA shell prevents oxidation and agglomeration, maintaining capacity	[90]
Carbon scaffold - Nanoporous aerogel	MgH_2 in carbon aerogel	Not reported	Not reported	Not reported	Indirect; pore-size confinement reduces effective MgH_2 particle size, contributing to surface energy destabilisation	Strong pore-size dependence; smaller pores → faster desorption rates via shortened diffusion pathways	Not reported	[91]
Carbon nanotube + catalyst	MgH_2–ZrO_2/C (carbon-encapsulated ZrO_2, 5–10 nm)	Not reported	Onset 208 (vs. 309 undoped)	Not reported	Moderate; onset T_{aes} reduced by 101 °C through synergistic CNT + ZrO_2 catalytic effect	Strong; CNTs create diffusion channels (10–50 nm grains); ZrO_2 catalyzes surface reactions	Not reported	[93]
Carbon shell + transition metal carbide	$Mg_{88}(TiC_{0.6})_{12}$@C (<50 nm, reactive gas evaporation)	5.5 (abs.)/4.5 (des.)	250 (abs.)/ 300 (des.)	Not reported	Moderate; carbon shell limits particle growth, maintaining surface-energy destabilisation effect across cycles	Strong; TiC_x catalyzes H_2 dissociation; carbon shell prevents aggregation, preserving active surface area	Good; stable capacity over 10 cycles — one of the few nanostructured systems with direct cycling evidence	[94]
MOF scaffold	Mg/ZIF-67 core-shell composite	44% H_2 release at 338 °C	338	Reduced by 43.2 vs. pure Mg	Moderate; MOF-induced defects create Mg–H bond interactions that lower enthalpy and T_{aes}	Strong; shortened diffusion path within fine MOF porosity; multiple active sites from defect formation	Excellent; hydrogen capacity unchanged after 100 cycles — best cycling stability reported in this section	[96]
MOF-derived catalyst	MgH_2 + Ni nanoparticles from Ni-MOF-74 (2–3 nm)	6.2	300 (full release in 20 min)	Not reported	Limited thermodynamic change; T_{aes} remains at 300 °C	Exceptional; 6.2 wt.% absorbed in 30 s at 150 °C — fastest absorption rate reported in this section	Not reported	[97]
MOF-derived catalyst — Fe	MgH_2–Fe-MOF (TMA-Fe, ball milled)	Not reported	Not reported	66.8 (hydrogenation)/ 142.3 (dehydrogenation)	Limited; dehydrogenation Ea reduced relative to pure MgH_2 but T_{aes} not reported	Moderate; hydrogenation Ea reduced to 66.8 kJ/mol; dehydrogenation improvement less pronounced at 142.3 kJ/mol	Not reported	[98]

Note: T_{des} = desorption temperature; Ea = activation energy for dehydrogenation unless stated otherwise.

affected in most nanostructured systems, and cycling durability remains limited by particle coarsening and agglomeration. The recent work on spatially programmed confinement catalysis [95] and hierarchical interface engineering [99] represents the most promising direction for simultaneously addressing both kinetics and cycle stability through engineered interfaces that resist sintering. However, the scalability of these nanostructured materials for industrial applications remains a critical area for further exploration [100]. Table 2 shows a comparison of nanostructuring strategies of Mg-based hydrogen storage materials.

Nanostructuring strategies consistently reduce E_a from the ~160 kJ/mol baseline toward 54–100 kJ/mol but rarely produce meaningful thermodynamic destabilisation. The most effective systems combine structural confinement with catalytic surface decoration. Those few systems with cycling data (Mg@PMMA, TiC_x@C, Mg/ZIF-67) consistently show better durability than systems without engineered coarsening resistance. The Mg/ZIF-67 system is the overall standout by balancing all three dimensions. The critical gap is that the majority of systems report no cycling data, limiting the ability to assess practical utility.

3.3. Metastable phase formation

Unlike alloying and nanostructuring, which modify the Mg–H bond indirectly through compositional or microstructural changes, metastable phase engineering addresses thermodynamic stability by altering the reaction pathway itself. This creates transient phases with lower formation enthalpies that allow hydrogen release without fully traversing the energy landscape of the stable β-MgH_2 phase. This makes it one of the few strategies capable of simultaneously reducing desorption temperature and preserving gravimetric capacity. It allows for changes in the enthalpy of formation and activation energy without affecting hydrogen capacity, while enhancing hydrogen storage performance [101].

Metastable phases modify the thermodynamic properties, specifically by altering their enthalpy of formation and activation energy of Mg-based hydrides by changing the reaction pathways and reducing the stability of MgH_2 without necessarily sacrificing hydrogen storage capacity, thus facilitating easier hydrogen release and uptake [44]. Metastable phase formation also addresses the issue of high dehydration temperatures and low equilibrium pressures by creating fewer stable phases that require lower energy for hydrogen release, thus reducing the operational temperatures and improving kinetics [72]. By introducing various additives, metastable phases can be achieved, leading to improved hydrogen storage performance [70]. For example, additives such as $LiBH_4$ and YNi_5 in MgH_2 composites form in-situ $MgNi_3B_2$ and YH_3, thereby improving reaction rates and cycle stability. This approach, combined with nanostructuring and alloying, effectively reduces dehydrogenation temperatures and improves kinetics [100]. However, their practical application is limited by slow kinetics and challenges in stabilizing these metastable phases and preventing aggregation during cycling. The creation and stabilization of metastable phases require precise control over synthesis conditions. The long-term stability of these phases under operational conditions remains a concern.

Metastable γ-MgH_2, a high-pressure phase distinct from the stable β-MgH_2, exhibits a distorted octahedral structure around magnesium atoms that leads to significantly lower surface energy and dehydration enthalpy (~45 kJ/mol H_2) compared to β-MgH_2 (~78 kJ/mol H_2) [44]. This structural difference results in improved hydrogen sorption properties, including reduced desorption temperatures and enhanced kinetics. γ-MgH_2 can be synthesized by heating α-MgH_2, ball milling, or hydrogenation of nanosized Mg, often forming nanocomposites with β-MgH_2 [101]. Studies have shown that the presence of γ-MgH_2 lowers the activation energy for hydrogen desorption from about 106 to 69 kJ/mol and reduces reaction enthalpy, indicating a synergistic destabilisation effect that facilitates hydrogen release at lower temperatures [44,102].

Despite these promising features, challenges remain in stabilizing γ-MgH_2 during cycling, as it tends to irreversibly revert to the β-phase or metallic Mg at elevated temperatures (~310 °C) [44]. The proportion of γ-MgH_2 in composites is often limited, and its desorption pathways are not fully understood. Recent theoretical predictions suggest other metastable MgH_2 phases with favourable thermodynamics and mechanical stability, such as a tetragonal structure with an enthalpy of −58 kJ/mol H_2 could further improve hydrogen storage performance [44]. Table 3 shows a comparison of metastable phase formation strategies for Mg-based hydrogen storage materials.

The starkest performance contrast is presented. The γ-MgH_2 row records the most impressive thermodynamic improvement in the entire section, yet its cycling stability is the worst of any characterized system reviewed. This contrast directly illustrates the central challenge of metastable phase engineering: the structural disorder that confers thermodynamic advantage is thermally unstable under cycling conditions. The table effectively communicates that stabilizing metastable phases under cycling conditions represents the field's most important unresolved scientific challenge in this area, and that metastable phase engineering remains the highest-potential but least-developed strategy in Section 3.

3.4. Composite materials design

Composite materials design integrates the benefits of multiple strategies, including catalytic doping, nanoconfinement, and interface engineering into a single material architecture, making it the approach most capable of simultaneously addressing kinetics, thermodynamics, and cycling durability. Rather than optimizing a single variable, composites exploit synergistic interactions between components: confinement matrices resist coarsening over cycling, catalytic additives lower activation energy, and interface strain weakens Mg–H bonds, together delivering improvements across all four challenge dimensions [103]. Nanocomposites enhance the sorption kinetics of Mg due to the shorter diffusion length for hydrogen and the higher nucleation rate, which prevents grain growth and sintering during the de/hydrogenation process [104]. By carefully selecting and integrating these components, the overall hydrogen storage capacity, kinetics, and thermodynamics of MgH_2-based materials can be significantly enhanced.

The remarkable qualities in MgH_2-based nanocomposite hydrogen storage materials stem from the integrated effects of particle confinement, catalytic activation, and interface engineering, which collectively enhance hydrogen sorption kinetics and thermodynamics. Catalytic additives like transition metals (e.g., Ni, V, La) or carbon-based materials (e.g., graphene, CNTs) promote efficient hydrogen molecule dissociation and provide rapid diffusion pathways, lowering activation energies [105]. Nanoconfinement and particle-size reduction prevent agglomeration and sintering, thereby preserving a high surface area and active sites that stabilize both kinetics and cycling properties [29]. Interface modifications induce lattice strain and electronic changes that weaken Mg–H bonds, reducing hydride stability and desorption temperatures. Moreover, conductive materials improve thermal and mass transport, which further accelerates reactions. These factors enable faster hydrogen sorption at lower temperatures without sacrificing storage capacity or cycle life.

A novel Ni-Nb/rGO nanocomposite was designed using a one-step hydrothermal method followed by calcination. The sorption properties of MgH_2 were improved by the remarkable catalytic action of a novel Ni-Nb/rGO nanocomposite. In comparison to undoped MgH_2 (330 °C), the onset desorption temperature of the MgH_2 + 10 wt.% Ni-Nb/rGO composite is lowered to 198 °C. Remarkably, at 245, 260, and 275 °C, the composite could release 5.0, 5.9, and 6.0 wt.% H_2 in 10 min, respectively. Even at room temperature, the dehydrogenated MgH_2 + 10 wt.% Ni-Nb/rGO composite begins to absorb hydrogen, achieving about 2.75 wt.% H_2 absorption at 75 °C at 3 MPa H_2 pressure in 30 min. It also demonstrates exceptional stability, retaining 6.0 wt.% hydrogen

Table 3
Comparison of Metastable Phase Formation Strategies for Mg-Based Hydrogen Storage (Effect of metastable phase engineering on thermodynamic stability, sorption kinetics, and cycling durability).

Metastable Phase Strategy	Representative System	Capacity (wt. %)	T_{aes} (°C)	Ea (kJ/mol)	Thermodynamic Effect	Kinetic Effect	Cycling Stability	Ref
Additive-induced in-situ phase formation	$MgH_2 + LiBH_4 + YNi_5 \rightarrow$ in-situ $MgNi_3B_2 + YH_3$	Not reported	Reduced vs. pure MgH_2	Reduced vs. pure MgH_2	Direct; in-situ formation of $MgNi_3B_2$ and YH_3 creates transient phases with lower formation enthalpies, reducing dehydrogenation temperature	Improved reaction rates through catalytic activity of in-situ formed phases; combined effect with nanostructuring and alloying further accelerates kinetics	Improved cycle stability reported; in-situ phases resist aggregation better than ex-situ additives	[100]
γ-MgH_2 — High-pressure metastable phase	γ-MgH_2/β-MgH_2 nanocomposite (ball milling or hydrogenation of nano-Mg)	Preserved (no capacity loss vs. β-MgH_2)	Below β-MgH_2 baseline	69 (↓ from 106)	Strong and direct; dehydration enthalpy ~45 kJ/mol H_2 vs. ~78 kJ/mol H_2 for β-MgH_2 — a ~42% reduction achieved without alloying or capacity loss	Strong; Ea reduced from ~106 to ~69 kJ/mol; distorted octahedral structure lowers surface energy and facilitates H release at lower temperatures	Poor; γ-phase irreversibly reverts to β-phase or metallic Mg above ~310 °C during cycling; proportion in composites is limited and difficult to control	[44]
Theoretically predicted metastable phase — tetragonal structure	Tetragonal MgH_2 polymorph (DFT-predicted)	Comparable to MgH_2 (predicted)	Below β-MgH_2 (predicted)	Not reported	Promising; predicted enthalpy of −58 kJ/mol H_2 — intermediate between γ-MgH_2 and β-MgH_2; thermodynamically favourable and mechanically stable per DFT	Not yet experimentally characterized; kinetic behaviour is theoretically anticipated but unconfirmed	Not yet experimentally demonstrated; stability under cycling conditions unknown	[44]

Note: T_{aes} = desorption temperature; Ea = activation energy for dehydrogenation unless stated otherwise (abs. = absorption, des. = desorption).

content after 20 cycles at 300 °C. Additionally, the activation energies for the de/hydrogenation of MgH_2 + 10 wt.% Ni-Nb/rGO are reduced to 57.8 kJ/mol and 33.9 kJ/mol, which are significantly lower than those of undoped MgH_2 [106]. Fig. 6 shows the TEM image of the MgH_2 + 10 wt.% Ni-Nb/rGO during the ball milling state.

The Ni@rGO nanocomposite was prepared using the ethylene glycol method, followed by an annealing process. The Ni@rGO nanocomposite exhibited a strong catalytic effect on the dehydrogenation and hydrogenation of MgH2. The ball-milled MgH_2-5 wt.% Ni@rGO composite showed faster sorption kinetics and a comparatively lower sorption temperature than pure MgH_2. The desorption peak temperature for MgH_2-5 wt.% Ni@rGO reduced from 356 °C for pure milled MgH_2 to 247 °C. Even after nine cycles, the MgH_2-5 wt.% Ni@rGO composite was still able to desorb 6.0 wt.% H_2 in 10 min at 300 °C. On the other hand, even after 120 min, the undoped MgH_2 only desorbed 2.7 wt.% H_2. In addition, the Ea decreased significantly compared to MgH_2 [107].

MgH_2@Ni-CNTs nanocomposites were created by ball-milling magnesium with catalytic and restrictive Ni-CNT nanoparticles [108]. Its activation energy of 74.8 kJ/mol, is much lower than that of pure MgH_2 because of the presence of Ni-CNTs. As a result, the kinetics of hydrogen absorption were significantly improved, with 7.20 wt.% H_2 absorbed in 30 min at 200 °C. The incorporation of Ti_3C_2 MXenes and indium

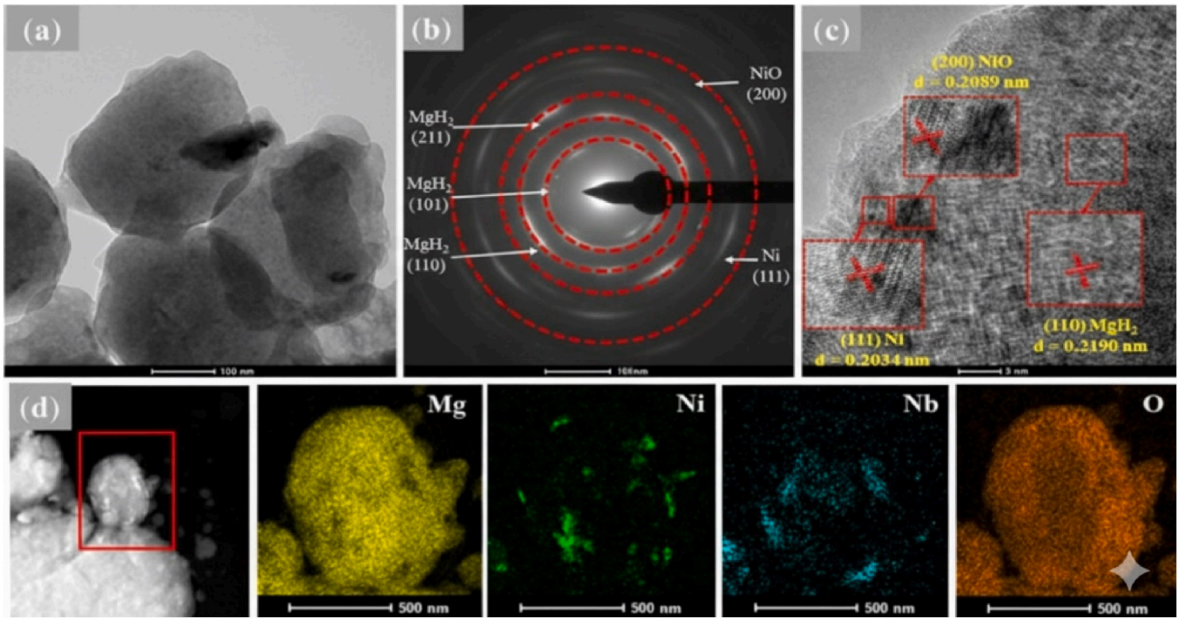


Fig. 6. TEM image of MgH_2 + 10 wt.% Ni-Nb/rGO at ball-milled state showing: (a) SAED diffraction rings, (b); HRTEM d-lattice spacing, (c); STEM-HAADF images with (d) being the corresponding EDS element mapping [106] (Reproduced with permission from Elsevier).

nanoparticles into MgH_2 shows a significant improvement in the hydrogen properties. The Ti_3C_2 MXenes facilitate hydrogen molecule dissociation and recombination, while indium nanoparticles reduce the thermodynamic stability of MgH_2, leading to a lower dehydrogenation temperature by 47 °C compared to commercial MgH_2 [109].

Magnesium with dispersed VH_2 particles (~10 nm) was prepared using the hydrogen plasma metal reaction technique. The MgV composite absorbed 5.0 wt.% H_2 within 5 min at 350 °C and released 4.0 wt.% in 15 min at 200 °C. Activation energies were reduced to 71.2 (absorption) and 119.4 kJ/mol (desorption) [110]. Mg-Zn nanocomposite was synthesized from Mg-10 wt.%Zn alloy via HPMR. This material exhibited a capacity of 6.1 wt.% at 300 °C, with an absorption energy of 56.3 kJ/mol. Amorphous MgZn intermetallic acted as active sites [111].

Table 4
Comparison of Composite Materials Design Strategies for Mg-Based Hydrogen Storage (Effect of composite architecture on thermodynamic stability, sorption kinetics, and cycling durability).

Composite Strategy	Representative System	Capacity (wt.%)	T_{aes} (°C)	Ea (kJ/mol)	Thermodynamic Effect	Kinetic Effect	Cycling Stability	Ref
TM + graphene catalyst composite	MgH_2 + 10 wt.% Ni-Nb/rGO (hydrothermal + calcination)	6.0	Onset 198 (↓ from 330)	57.8 (des.)/ 33.9 (abs.)	Strong; T_{aes} reduced by 132 °C; interface strain from Ni-Nb on rGO weakens Mg–H bonds and lowers hydride stability	Exceptional; 5.0–6.0 wt.% released in 10 min at 245–275 °C; absorption begins at room temperature (2.75 wt.% at 75 °C in 30 min)	Excellent; retains 6.0 wt.% after 20 cycles at 300 °C — strongest combined kinetic and cycling result in this section	[106]
Ni-decorated graphene composite	MgH_2–5 wt.% Ni@rGO (ethylene glycol method + annealing)	6.0	247 (↓ from 356)	Reduced vs. pure MgH_2 (not quantified)	Moderate; T_{aes} reduced by 109 °C via Ni catalytic and rGO confinement effects	Strong; 6.0 wt.% desorbed in 10 min at 300 °C vs. only 2.7 wt.% in 120 min for undoped MgH_2	Good; retains 6.0 wt.% desorption capacity after 9 cycles	[107]
TM-decorated CNT composite	MgH_2@Ni-CNT nanocomposite (ball milling)	7.20	Not reported	74.8	Limited thermodynamic data; no T_{aes} reported	Strong; 7.20 wt.% absorbed in 30 min at 200 °C — highest reported capacity in this section; Ni-CNTs provide both catalytic and diffusion channel functions	Not reported	[108]
2D MXene + post-transition metal composite	MgH_2 + Ti_3C_2 MXene + In nanoparticles	Not reported	Lowered by 47 °C vs. commercial MgH_2	Not reported	Direct dual-mechanism; In nanoparticles reduce thermodynamic stability of MgH_2; Ti_3C_2 provides additional lattice strain	Strong; Ti_3C_2 facilitates H_2 dissociation and recombination; In lowers energy barrier for desorption	Not reported	[109]
TM hydride dispersion composite	Mg + VH_2 (~10 nm, hydrogen plasma metal reaction)	5.0 (abs.)/4.0 (des.)	200 (desorption)	71.2 (abs.)/ 119.4 (des.)	Moderate; desorption achieved at 200 °C, meaningfully below pure MgH_2; VH_2 dispersal modifies local thermodynamic environment	Good; 5.0 wt.% absorbed in 5 min at 350 °C; 4.0 wt.% released in 15 min at 200 °C; V acts as catalytic gateway for H diffusion	Not reported	[110]
Amorphous intermetallic composite	Mg-10 wt.% Zn nanocomposite (HPMR)	6.1	300	56.3 (absorption)	Moderate; amorphous MgZn intermetallics act as active sites that locally destabilize Mg–H bonding	Good; low absorption Ea of 56.3 kJ/mol; amorphous phase provides high density of active sites for H diffusion	Not reported	[111]
Core-shell intermetallic composite	Mg@$Mg_{17}Al_{12}$ (7–27 at.% Al; varying content)	6.2 (at 7 at.% Al)	300	49.3 (absorption)	Moderate; $Mg_{17}Al_{12}$ shell introduces lattice strain that weakens Mg–H bond; also improves oxidation resistance	Strong; absorption Ea of 49.3 kJ/mol — among lowest absorption Ea values in this section; core-shell architecture provides rapid diffusion pathways	Good; improved oxidation resistance of core-shell structure preserves surface activity across cycles; long-term data not reported	[112]
Multicomponent RE + TM composite	Mg-La-Al and Mg-La-Ni (rapid solidification)	>6.5	400 (within 10 min)	Not reported	Moderate; LaH_3 and Mg_2Ni in-situ phases lower local thermodynamic barriers; T_{aes} remains relatively high at 400 °C	Strong; synergistic catalytic effect of La and Al/Ni; >6.5 wt.% achieved within 10 min demonstrating fast kinetics at operating temperature	Not reported	[113, 114]
Nanocrystalline melt-spun composite	Mg-Ni-Mm (melt spinning; Mg_2Ni + $Mg_{12}Mm$ phases)	5.1	Narrowed desorption range	Not reported	Moderate; $Mg_{12}Mm$ rare-earth phase modifies local Mg–H bond environment; narrowed desorption range indicates more uniform thermodynamic landscape	Improved vs. pure MgH_2; nanocrystalline Mg_2Ni phase provides catalytic sites and shortened diffusion paths	Not reported	[115]

Note: T_{aes} = desorption temperature; Ea = activation energy for dehydrogenation unless stated otherwise (abs. = absorption, des. = desorption). HPMR = hydrogen plasma metal reaction; rGO = reduced graphene oxide; RE = rare earth; TM = transition metal.

$Mg@Mg_{17}Al_{12}$ core-shell nanocomposite with varying Al content (7–27 at.%) showed improved oxidation resistance and rapid kinetics. Mg-7 at% Al reached 6.2 wt.% capacity at 300 °C with an absorption activation energy of 49.3 kJ/mol [112]. The Mg-La-Al and Mg-La-Ni composite system was created via the rapid solidification method. The addition of La and Al/Ni produced LaH_3 and Mg_2Ni particles that catalyzed hydrogen sorption. Both systems exceeded 6.5 wt.% capacity at 400 °C within 10 min [113,114]. Similarly, Melt-Spun Mg-Ni-Mm alloy prepared via Rapid solidification generated nanocrystalline Mg_2Ni and $Mg_{12}Mm$ phases. These alloys showed improved kinetics and narrowed desorption ranges. A maximum of 5.1 wt.% was recorded [115].

The incorporation of catalytic additives and conductive materials into MgH_2-based nanocomposites has significantly enhanced hydrogen storage performance by lowering desorption temperatures, reducing activation energies, and improving hydrogen sorption kinetics. Many of these composites are produced via milling or hydrothermal methods; however, these methods can be paired with other techniques, such as severe plastic deformation (SPD) or arc plasma synthesis, to further optimize their properties through grain refinement and defect generation, which promote hydrogen diffusion and catalytic dispersion.

Although research has reported kinetic improvements, only a few studies have probed why these enhancements occur at the atomic scale. For instance, Zhu et al. employed in-situ synchrotron X-ray diffraction (XRD) to monitor phase transitions during hydrogenation in Ti and In-doped MgH_2, revealing that lattice strain and interfacial hydrogen accumulation lower energy barriers for nucleation [116]. Similarly, Lyu et al. combined high-resolution TEM and electron energy loss spectroscopy (EELS) to visualize hydrogen diffusion along grain boundaries in MgH_2@Ni nanoparticles [47]. These results indicate that interfacial charge transfer, lattice distortion, and nanoconfinement effect are key contributors to the improved thermodynamics and kinetics of MgH_2 nanocomposites. Future investigations should integrate in-situ transmission electron microscopy (in-situ TEM), which enables direct observation of nucleation and growth of hydride phases in real time and synchrotron-based XRD, which offers real-time resolved tracking of hydrogen absorption/desorption kinetics. Furthermore, density functional theory (DFT) and molecular dynamics (MD) can simulate adsorption energies, migration pathways and the role of catalyst-matrix electronic interactions [50].

Building upon the recent findings summarized above, future works should move beyond empirical testing towards mechanistically guided composite design. For example, optimizing core-shell architectures (e.g., $Mg@Mg_{17}Al_{12}$ [112]) and 2D heterostructured catalysts (e.g., Ti_3C_2–In Ref. [109]) can simultaneously enhance hydrogen diffusion and thermal conductivity. Similarly, La/Ni co-doped Mg-based composites [113, 114] demonstrate that multicomponent systems yield synergistic catalytic and structural effects, balancing kinetics and capacity of MgH_2 nanocomposites. Table 4 shows a comparison of composite-design strategies for Mg-based hydrogen storage materials.

Across the four modification strategies reviewed in this section, a consistent hierarchy of effects emerges. Alloying delivers the broadest simultaneous impact on thermodynamics and kinetics but introduces unavoidable capacity trade-offs as alloying element content rises. Nanostructuring targets kinetics most aggressively, reducing Ea from ~160 toward 60–90 kJ/mol. However, thermodynamic stability largely remains unaffected, meanwhile, cycling durability risks are introduced from particle coarsening. Metastable phase engineering is the only strategy capable of reducing desorption enthalpy substantially (γ-MgH_2: ~45 kJ/mol H_2) without sacrificing gravimetric capacity, but its practical utility is currently constrained by phase instability above 310 °C. Composite materials design, by integrating catalytic, confinement, and interface engineering effects into a single architecture, consistently delivers the strongest combined performance. The Ni-Nb/rGO system represents the current state-of-the-art across kinetics, thermodynamics, and cycling simultaneously. Cycling durability is the least reported metric across all four strategies, representing the most significant gap between laboratory demonstration and practical deployment. Future material design should prioritize integrated approaches that combine thermodynamic destabilisation with confinement-mediated cycling stability, rather than optimizing any single dimension in isolation.

3.5. Solar-driven hydrogen storage

The modification strategies reviewed in Sections 3.1-3.4 address the thermodynamic and kinetic barriers of MgH_2 hydrogen storage primarily through materials design, with external electrical heating as the default energy input source for dehydrogenation. However, the large enthalpy of dehydrogenation ($\Delta H \approx -74.5$ kJ/mol H_2) means that the energy cost to drive hydrogen release from MgH_2 systems can account for a substantial fraction of the stored energy content, reducing the net system energy density and increasing operational costs. Solar-driven hydrogen storage has emerged as a distinct strategy that directly addresses the energy input problem by replacing electrical heating with concentrated solar irradiation as thermodynamic driving force, while simultaneously deploying photothermal-active materials as catalytic additives that lower the kinetic barrier [33–36].

The concept of solar-driven hydrogen storage rests on the dual function od specially designed additives that serve simultaneously as (i) light absorbers generating localized heat through the photothermal effect, and (ii) thermochemical catalysts that lower the activation energy for H_2 dissociation and Mg–H bond breaking. The combination is necessary because neither function alone is sufficient: photothermal heating without catalysis still requires high light intensities to reach the >300 °C desorption temperature of unmodified MgH_2, while catalysis without photothermal heating still demands an external heat source. The principle exploits MgH_2's poor intrinsic thermal conductivity, which acts as a "heat isolator," allowing locally generated heat from photothermal additives to concentrate at catalytic sites rather than dissipating rapidly into surrounding material [33].

The first demonstration of this concept for metal hydrides was provided by Sun et al. [32], who showed that TiO_2@C nanocomposites, coupling the catalytic effect of TiO_2 with the photothermal property of carbon nanosheets, could drive complete hydrogen release from $NaAlH_4$ within 7 min under 10 sun irradiation, achieving a reversible capacity of 4 wt.% after 10 cycles. This established the TiO_2@C architecture as a template for light-mediated catalytic hydrogen storage and motivated its extention to MgH2-based systems.

Zhang et al. [33] demonstrated the first solar-driven reversible hydrogen storage in MgH_2 using Cu nanoparticles uniformly distributed on MXene (Ti_3C_2) nanosheets (Cu@MXene). The photothermal effect of Cu nanoparticles, driven by their localized surface plasmon resonance (LSPR), heats the MgH_2 to ~209 °C within 5 min under 2.61 W cm^{-2} irradiation. Simultaneously, Ti and TiH_x species formed in-situ by the reduction of MgH_2 on the MXene surface act as a "hydrogen pump," catalytically lowering the barrier for reversible H_2 absorption and desorption. The combined photothermal and catalytic effect achieves a reversible capacity of 5.9 wt.% H_2 after 30 cycles using solar irradiation as the sole energy input. A critical limitation of the first-generation design is the physical separation between the photothermal Cu/MXene and the catalytic Ti/TiH_x sites, which delays heat transfer and reduces light-to-heat conversion efficiency, necessitating light intensity up to 4.0 W cm^{-2} for complete reversible cycling.

Hu et al. [34] addressed the phase separation limitation by designing flower-like TiN@N-doped TiO_2 microspheres that integrate the photothermal light absorber (TiN, LSPR active) and the thermochemical catalyst (TiN_xO_y/Ti/TiH_2 pairs) at the nanometer scale within a single-component material. During cycling, N-doped TiO_2 transforms in-situ into TiN_xO_y and Ti/TiH_2 distributed within the TiN matrix. The direct co-location of heat generation and catalytic activation eliminates the heat transfer delay, reducing the required light intensity to 27 sun for achieving a capacity of 6.1 wt % H_2. The intimate TiH_2–MgH_2 interface simultaneously destabilizes Mg–H bonds thermodynamically

and weakens Ti–H bonds through a mutual catalytic effect, lowering both the hydrogenation enthalpy and kinetic barriers without increasing the gravimetric penalty from additive loading.

Zhang et al. [35] advanced the concept further by designing a single-phase $Mg_2Ni(Cu)$ alloy through an in-situ alloying reaction between MgH_2 and CuNi during the initial dehydrogenation cycle. The ternary $Mg_2Ni(Cu)$ phase combines intra/inter-band optical transitions that absorb over 85% of the solar spectrum with the catalytic "hydrogen pump" effect of $Mg_2Ni(Cu)/Mg_2Ni(Cu)H_4$ cycling. Under 2.6 W cm^{-2} irradiation, the surface temperature reaches 261.8 °C. Moreover, the imbalanced distribution of LSPR-induced hot electrons within the CuNi and $Mg_2Ni(Cu)$ phases facilitates weakening of Mg–H bonds, providing a non-thermal photocatytic contribution to dehydrogenation beyond simple photothermal heating. The reversible hydrogen storage capacity of 6.1 wt.% with 95% retention over multiple cycles under 3.5 W cm^{-2} represents the current state-of-the-art for solar-driven MgH_2 storage, and the atomic reconstruction mechanism that regenerates the $Mg_2Ni(Cu)$ phase upon each dehydrogenation cycles, provides intrinsic cycling stability without requiring external regeneration.

Furthermore, Zhang et al. [36] introduced a mechanistically distinct approach applicable to complex borohydrides, demonstrating that photogenerated hydrogen vacancies in LiH thermodynamically destabilize B–H bonds in adjacent borohydride groups through asymmetric electron redistribution. By encapsulating nanoscale dispersed LiH with borohydrides within "nano-photothermal reactors" that create spatially confined hot spots, this strategy achieved hydrogen release at temperatures approximately 300 °C lower than the corresponding thermal process, effectively bringing complex borohydride dehydrogenation within the range of concentrated solar irradiation.

Despite these advances, one of the major practical challenge for solar-driven hydrogen storage in MgH_2 is that the light intensities required (2.6–4.0 W cm^{-2}, equivalent to ~26–40 sun) substantially exceed the direct normal irradiance available at Earth's surface (~0.1 W cm^{-2}), meaning that solar concentrators are an essential system component whose cost and complexity are not yet accounted for in most material-level studies.

3.6. Practical challenges associated with real-world implementation

Despite the substantial kinetic and thermodynamic improvements documented in Section 33, a significant gap persists between laboratory-scale demonstration and practical deployment of Mg-based hydrogen storage materials. Four challenges define this gap and deserve explicit attention.

Many of the highest-performing systems in this review incorporate noble metals (Pt, Pd, Rh), rare-earth elements (La, Y), or complex nanostructured architectures (MOF scaffolds, core-shell geometries) whose synthesis costs and manufacturing complexity are prohibitive at the kilogram-to-tonne scale required for vehicle or stationary storage applications. The Ni-Nb/rGO and Ni-MOF-74 systems, while outstanding in laboratory performance, require multi-step hydrothermal or bottom-up reduction syntheses that have not been demonstrated at scale. As Zhang et al. [117] note, the use of carbon materials derived from MOF precursors introduces high catalyst costs that currently restrict widespread application despite their excellent catalytic performance. Future work should explicitly evaluate material cost per kilowatt-hour of stored hydrogen alongside gravimetric and kinetic metrics, a point reinforced by the techno-economic analysis of Mg–Ni composites by Falcão et al. [118], who found that cost-effectiveness is highly sensitive to milling parameters and that small variations in synthesis conditions produce significant scatter in both microstructure and hydrogen absorption performance.

As documented in the comparison tables in Section 3, cycling stability data are reported for fewer than a third of the systems reviewed, and where reported, cycle counts rarely exceed 20–100 cycles. Commercial hydrogen storage applications require thousands of cycles over years of operation. The fundamental degradation mechanisms such as particle coarsening in nanostructured systems, phase segregation in composites, surface oxidation in cycling environments are understood qualitatively but rarely quantified across sufficient cycle numbers to extrapolate lifetime performance. El-Eskandarany et al. [119] provide one of the most instructive long-term cycling datasets in the field: their MgH_2/5 wt.% $TiMn_2$ nanocomposite sustained cycling over 1,400 h without significant capacity loss, while bare nanocrystalline MgH_2 degraded severely within 275 h due to grain growth and pore collapse, demonstrating that additive selection is decisive for durability and that such extended cycling studies with post-cycling microstructural characterization must become a standard reporting requirement. Standardized accelerated cycling protocols and cross-laboratory reporting of capacity retention as a function of cycle number are urgently needed [120].

Mg-based hydrides, including even the most optimized composites, operate at temperatures of 200–400 °C, which is significantly above the waste heat available from proton exchange membrane (PEM) fuel cells (~80 °C). This thermal mismatch is a well-documented fundamental barrier: the dehydrogenation temperature of MgH_2 is as high as 350 °C, which is much higher than the vehicle-mounted hydrogen release temperature requirement of the U.S. Department of Energy (DOE) of lower than 85 °C [121]. No system reviewed in this work simultaneously achieves the DOE targets of >6.5 wt.% capacity, T_des <85 °C, and demonstrated cycling stability above 1,000 cycles. These three constraints are the field's most pressing practical challenge. Wang et al. [121] demonstrated that microwave plasma enhancement can reduce the effective MgH_2 dehydrogenation temperature to 109 °C with an energy consumption cost of approximately 1.71 $/kg$H_2$, illustrating that thermal process engineering, not only materials design, is part of the integration solution. At the system level, Tan et al. [8] further showed that solid-state hydrogen storage can be effectively integrated into on-board and stationary applications through composite material and heat management design strategies, though the temperature mismatch with PEM fuel cells remains an unresolved constraint for low-temperature mobile applications.

Moreover, synthesis routes that produce optimal nanostructured or composite materials in milligram quantities such as reactive gas evaporation, arc plasma methods, in-situ MOF reduction face significant engineering challenges in maintaining particle size distribution, phase homogeneity, and surface cleanliness at larger scales. Ball milling, the most scalable of the synthesis methods reviewed, consistently produces inferior kinetic and thermodynamic outcomes compared to more controlled nanostructuring methods, as systematically documented [76] across nanoconfinement and catalysis strategies for MgH_2. The techno-economic analysis by Falcão et al. [118] further demonstrated that variations in milling time and rotational speed modify lattice parameters and particle sizes in ways that directly influence hydrogen absorption behaviour and overall cost. This highlights that the processing–performance tension is not merely a laboratory challenge but an economic one that must be resolved before commercialization.

4. Hydrogen storage properties

The hydrogen storage properties of metal hydrides depend on several factors.These are related to the composition of the alloys, the crystal structure, electronic structure, morphology, and other intrinsic properties of the parent metal and the properties of the metal hydrides. Here, we review important characteristics of metallic hydrides with special emphasis on Mg-based hydrides, including Mg-containing HEAs and their characteristics, such as hydrogen storage capacity, PCT properties, thermal stability, reaction kinetics, activation, and cycling properties.

4.1. Hydrogen storage capacity of Mg-based hydrides and Mg-containing HEAs

Hydrogen storage capacity can be measured either via mass ratio [H/M] or through thermogravimetric analysis (TGA). Researchers have investigated various hydrogen storage materials, including $NaAlH_4$, MgH_2, $LiBH_4$, $Mg(BH_4)_2$ and HEAs. MgH_2 stands out due to its high storage capacity of 7.6 wt.% and relatively low cost. The relatively high desorption enthalpy (~75 kJ/mol) indicates strong Mg–H chemical bonds that require significant energy input (high temperature) to break, resulting in high hydrogen desorption temperatures typically above 300 °C. The stable thermodynamics and sluggish kinetics of MgH_2 present challenges for commercial applications. Several techniques including nanosizing, alloying, and catalyst doping, have been employed to enhance the hydrogen storage properties of MgH_2. Advanced synthesis techniques, such as ball milling and severe plastic deformation, enhance the hydrogen storage properties of Mg-based hydrides through microstructural refinement [87]. Moreover, creating Mg-based nanostructures and alloying with intermetallic compounds like TiFe can improve hydrogen sorption kinetics and reduce desorption temperatures [122].

Mg_2NiH_4 is one of the most studied Mg-based complex hydrides, formed via the reaction $Mg_2Ni + 2H_2 \rightarrow Mg_2NiH_4$. It stores ~3.6 wt.% H_2, with a desorption temperature of around 250–300 °C and a desorption enthalpy of ~64 kJ/mol H_2, significantly lower than pure MgH_2 (~74.5 kJ/mol H_2) [123]. The reduced stability arises because the Ni–H interaction in Mg_2NiH_4 is much weaker than the Mg–H interaction in pure MgH_2, leading to a lower formation enthalphy [124]. The complex undergoes a monoclinic-to-cubic phase transition at ~240 °C, and both phases have been characterized by neutron diffraction [124]. Recent work has demonstrated that nanoconfinement of Mg_2Ni within mesoporous carbon hosts produces particles (~4 nm) with markedly faster sorption kinetics, achieving near-full absorption and desorption within approximately 5 min at 210 °C. The thermodynamic properties remain unchanged relative to bulk Mg_2NiH_4, confirming that kinetic rather than thermodynamic modification is the primary benefit of nanoconfinement in this system [125]. Catalytic doping with rare-earth elements and transition metals further reduces T_des to below 220 °C in several reported systems [123,126].

Mg_2FeH_6 offers one of the highest known volumetric hydrogen densities (150 kg H_2/m^3) with a gravimetric capacity of ~5.5 wt.% [124]. It is synthesized via reactive ball milling of MgH_2 and Fe powder under hydrogen pressure or via high-pressure sintering. The decomposition enthalpy (~98 kJ/mol H_2) is higher than MgH_2, resulting in T_des >400 °C. Destabilisation strategies have been explored to bring the operating temperature into a practical range. Combining Mg_2FeH_6 with $LiBH_4$ in a composite is energetically favoured because FeB and MgB_2 form as stable intermediate compounds during dehydrogenation, thermodynamically destabilizing both hydrides simultaneously [127]. The $5LiBH_4$–Mg_2FeH_6 composite showed a hydrogen desorption capacity of 5.6 wt.% at 370 °C and could be partially rehydrogenated, with both composites exhibiting enhanced desorption kinetics and capacity at lower temperatures compared to neat Mg_2FeH_6 [128]. Partial substitution of Fe with Ni represents an additional credible destabilisation pathway. The $[FeH_6]^{4-}$ octahedral complex is central to the structure, confirmed by X-ray and neutron diffraction.

The concept of reactive hydride composites (RHC) involves mixing MgH_2 with light borohydrides ($LiBH_4$, $Mg(BH_4)_2$, $Ca(BH_4)_2$) such that the dehydrogenation products of one component serve as the hydrogenation reactants for the other [129]. The landmark demonstration was provided by Vajo et al. [130] who showed that mechanically milled mixtures of $LiBH_4 + ½MgH_2$ (with 2–3 mol% $TiCl_3$ catalyst) reversibly store 8–10 wt.% H_2 at 315–400 °C via the reaction: $MgH_2 + 2LiBH_4 \leftrightarrow MgB_2 + 2LiH + 4H_2$. This destabilisation reduces ΔH by ~25 kJ/mol H_2 relative to pure $LiBH_4$, attributable to the thermodynamic stabilization of the dehydrogenated state by MgB_2 formation. Bimetallic NiCo nanoporous carbon catalysts induced in-situ formation of $MgNi_3B_2$ and CoB as heterogeneous nucleation sites for MgB_2, yielding a reversible capacity of 8.4 wt.% after 10 cycles with 95.5% retention of the second-cycle capacity [131]. A comprehensive review of $LiBH_4$-based materials confirms that advanced carbon architectures and metal oxide catalysts now achieve activation energies as low as 82.5 kJ/mol with 93% capacity retention over 20 cycles through interface engineering and nanoconfinement. Extension to MgH_2–$Mg(BH_4)_2$ and MgH_2–$Ca(BH_4)_2$ composites has been reported, with MgB_2 formation identified as the key thermodynamic driver across all Mg–borohydride RHC systems [76]. Ding, Li, and Shaw [132] demonstrated that nanostructuring the $LiBH_4$–MgH_2 composite via ball milling with aerosol spraying opens three parallel hydrogen release pathways including the in-situ formation of $Mg(BH_4)_2$, releasing up to 4.11 wt.% H_2 at temperatures below 265 °C without any catalyst, establishing that nano-engineering can unlock thermodynamically favourable but kinetically constrained RHC systems. Collectively, this class of materials represents one of the most promising approaches to overcoming the thermodynamic stability of Mg-based hydrides. Recent catalytic advances have largely resolved the kinetic barrier, while reversibility and operating temperature remain the primary targets for further optimization.

There has been a growing interest in HEAs for hydrogen storage, with their hydrogen storage capacity ranging from 0.2 to 3.5 wt.% of H_2 [133]. However, most articles published report compositions based on transition metal elements. These transition metal elements limit the gravimetric capacities due to their high densities. Nonetheless, few researchers are substituting some transition elements with Mg, which reduces the overall weight of the alloy while improving the gravimetric capacity when compared to other HEAs [134]. The $Mg_{0.10}Ti_{0.30}V_{0.25}Zr_{0.10}Nb_{0.25}$ alloy can absorb hydrogen within 1 min at room temperature, forming a hydride phase with a capacity of 1.7 H/M (2.7 wt.%) [135]. $MgZrTiFe_{0.5}Co_{0.5}Ni_{0.5}$ HEA can absorb about 1.2%wt. of hydrogen [136]. Reactive milled MgAlTiFeNi HEA showed a hydrogen storage capacity of 0.94 wt.%. A_2B type. $MgTiNbCr_{0.5}Mn_{0.5}Ni_{0.5}$ alloy and its derivative $Mg_{0.68}TiNbNi_{0.55}$ alloy present a total gravimetric capacity of around 1.6 wt.% H_2 [134]. Strozi et al. [137] synthesized a lightweight Mg-V-Al-Cr-Ni HEA; the hydrogen storage capacity was found to be very low (approximately 0.3 wt.% of H). The available hydrogen storage capacity compared to the hydrogen storage capacity of existing Mg-containing HEAs is shown in Fig. 7.

4.2. Pressure-composition-temperature property and thermal stability

The pressure-composition-temperature (PCT) property describes the relationship between the pressure, composition, and temperature of hydrogen in a storage material. It is essential to understand how much hydrogen can be absorbed or released by a material under varying conditions of pressure and temperature. The property is important for evaluating the efficiency and effectiveness of hydrogen storage materials. It aids in determining how well a material can store hydrogen at different temperatures, while monitoring the amount of hydrogen absorbed or desorbed by the material, which is vital for practical applications in fuel cells and other similar uses. The hydrogen storage capability is typically measured using a PCT apparatus, which allows for controlled variations in pressure and temperature while monitoring the amount of hydrogen absorbed or desorbed by the material [138].

Thermal stability refers to the ability of a material to maintain its properties and structure when exposed to high temperatures. The thermal stability of MgH_2 is a crucial factor influencing its application as a hydrogen storage material. For MgH_2, this involves its resistance to decomposition and ability to release or absorb hydrogen without significant structural changes. MgH_2 has a large negative heat of formation (approximately −74.75 kJ/mol H_2), indicating that it is thermodynamically stable at room temperature but requires significant energy input to decompose [44]. The kinetics of hydrogen release from MgH_2 is relatively slow at temperatures below 400 °C [139]. Pristine MgH_2 starts

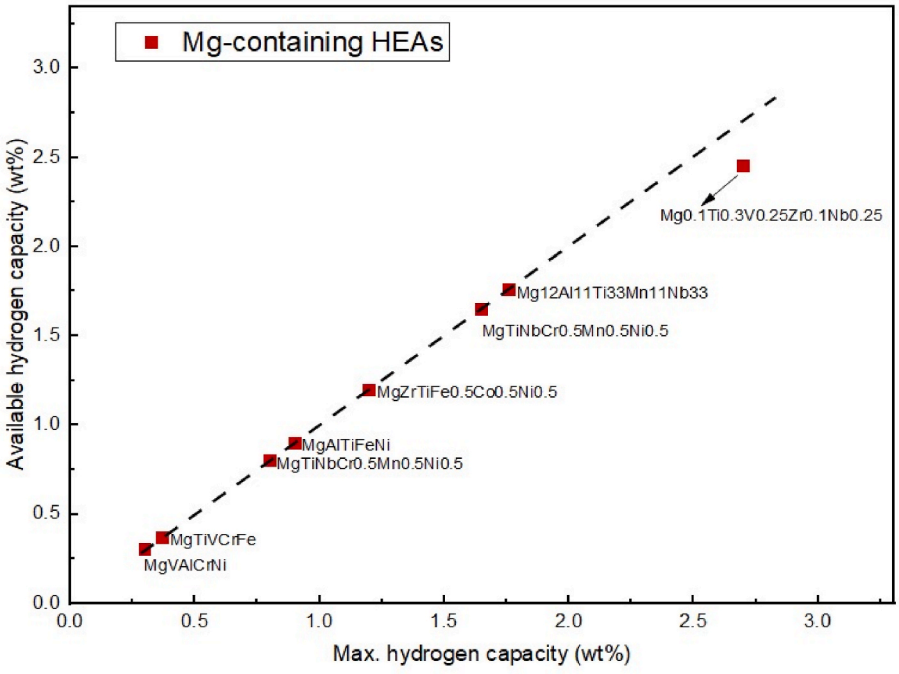


Fig. 7. Maximum and available hydrogen capacity of Mg-containing HEAs.

desorbing hydrogen near 320 °C and can achieve nearly full capacity around 400 °C, but the kinetics are slow below 350 °C, and it may take tens of minutes to hours to release significant hydrogen at 400 °C. However, the use of various catalytic agents can enhance the thermal stability and kinetics of MgH_2. Research has shown that different catalysts can significantly alter the thermal behaviour of MgH_2. Moreover, strategies like alloying, nanostructuring, and metastable phase formation can effectively tune its thermodynamics, reducing dehydrogenation enthalpies and temperatures, thus enhancing its potential as a hydrogen storage material [44].

Khan et al. studied the hydrogen storage performance of pure MgH_2 against MgH_2-In composite synthesized through high-energy ball milling. The PC isotherms of pure MgH_2 and the MgH_2-In composite at 350 °C. Fig. 8 shows the pressure-composition isotherm of pure MgH_2 in comparison with the MgH_2-In composite, where the de/hydrogenation of pure MgH_2 shows flat plateaus over the entire composition range corresponding to the single-phase hydride formation/decomposition. There is a significant reduction in the pressure hysteresis observed in MgH_2-In composite when compared to pure MgH_2. The lowered hysteresis is associated with the improved de/hydriding kinetics of the composite [79].

The addition of Ni effectively improves the thermodynamic properties of Mg-based hydrogen storage materials by catalyzing hydrogen dissociation. For instance, Mg_{95-x}-Nix-Y_5 (x = 5, 10, 15) alloys were prepared by induction melting. XRD analysis confirmed the presence of evenly dispersed MgH_2, YH_3, and Mg_2NiH_4 nanocrystalline phases in both the hydrogenated and dehydrogenated alloys. They recorded low desorption enthalpies for the Ni_5, Ni_{10}, and Ni_{15} alloys to be 84, 69.1, and 63.5 kJ/mol H_2, respectively. They also reported that 90% of the storage capacity (5.4 wt.% H_2) can be absorbed within 1 min at an optimal temperature of 200 °C. The dehydrogenation activation energy of the $Mg_{85}Ni_{15}Y_5$ alloy was also reduced to 67.0 kJ/mol, allowing for the complete release of H_2 within 5 min at 320 °C. The PCT curves of Mg_{95-x}-Nix-Y_5 at different Ni contents are measured at 300, 320, 340, and 360 °C [140] (see Fig. 9 for the SEM, TEM and XRD diagrams and Fig. 10 for the PCT diagram).

Nevertheless, HEAs present a qualitatively different PCT landscape that reflects their fundamentally more complex thermodynamic character. While conventional Mg-based alloys typically produce PCT isotherms with clear, flat plateaus from which ΔH and ΔS can be extracted reliably, PCT curves of HEAs characteristically display a narrow solid-solution region, a long and steeply sloped plateau, and significant hysteresis [133]. These features are not defects; they are direct consequences of the compositional complexity that defines HEAs. On the atomic scale, the coexistence of multiple elements with different atomic radii, electronegativities, and hydrogen affinities creates a distribution of local hydrogen-binding energies rather than a single, uniform binding environment. Hydrogen atoms occupying different interstitial sites, surrounded by varying combinations of Ti, Zr, V, Nb, or Mg nearest neighbours, experience a continuous spread of local thermodynamic conditions. The result is that hydrogen absorption and desorption occur progressively across a range of pressures rather than at a single plateau pressure, producing the sloped isotherm that is the PCT hallmark of HEAs. Local chemical ordering, atomic volume mismatch, and charge transfer between dissimilar elements further modulate these local environments, enhancing microstructural homogeneity and contributing to the exceptional structural stability that many HEAs exhibit under prolonged high-temperature cycling. This is a direct practical advantage over nanostructured MgH_2 composites that coarsen and sinter under equivalent conditions [133].

The pressure-composition isotherms of HfNbTiVZr were measured at 289, 317, and 341 °C, yielding ΔH and ΔS values of −59 kJ/mol H_2 and 82 J/mol H_2·K, respectively. The moderate reaction enthalpy suggests that the stability of the hydrides lies between that of AB_5-type and Mg hydrides [141]. Zhang et al. [142] conducted PCT experiments for TiZrNbTa at 20, 120, and 220 °C, calculating ΔH = −6.4 kJ/mol H_2 and ΔS = 4.3 J/mol H_2·K, values notably lower than those of typical hydrides. Additionally, the hydride formation enthalpy of ZrTiVNiCrFe, as determined by calorimetry, was found to be 38.8 kJ/mol H_2 [143]. The MgTiVZrNb alloy exhibits a low hydrogen absorption enthalpy (ΔH = −35.4 kJ/mol H_2), which is attributed to lattice strain effects that facilitate hydrogen desorption at lower temperatures [65].

The pattern that emerges from this dataset is instructive: Mg-containing HEAs consistently exhibit ΔH values in the range −35 to −59 kJ/mol H_2—intermediate between transition-metal-only HEAs (which can reach as low as −6.4 kJ/mol H_2) and pure MgH_2 (−74.5 kJ/

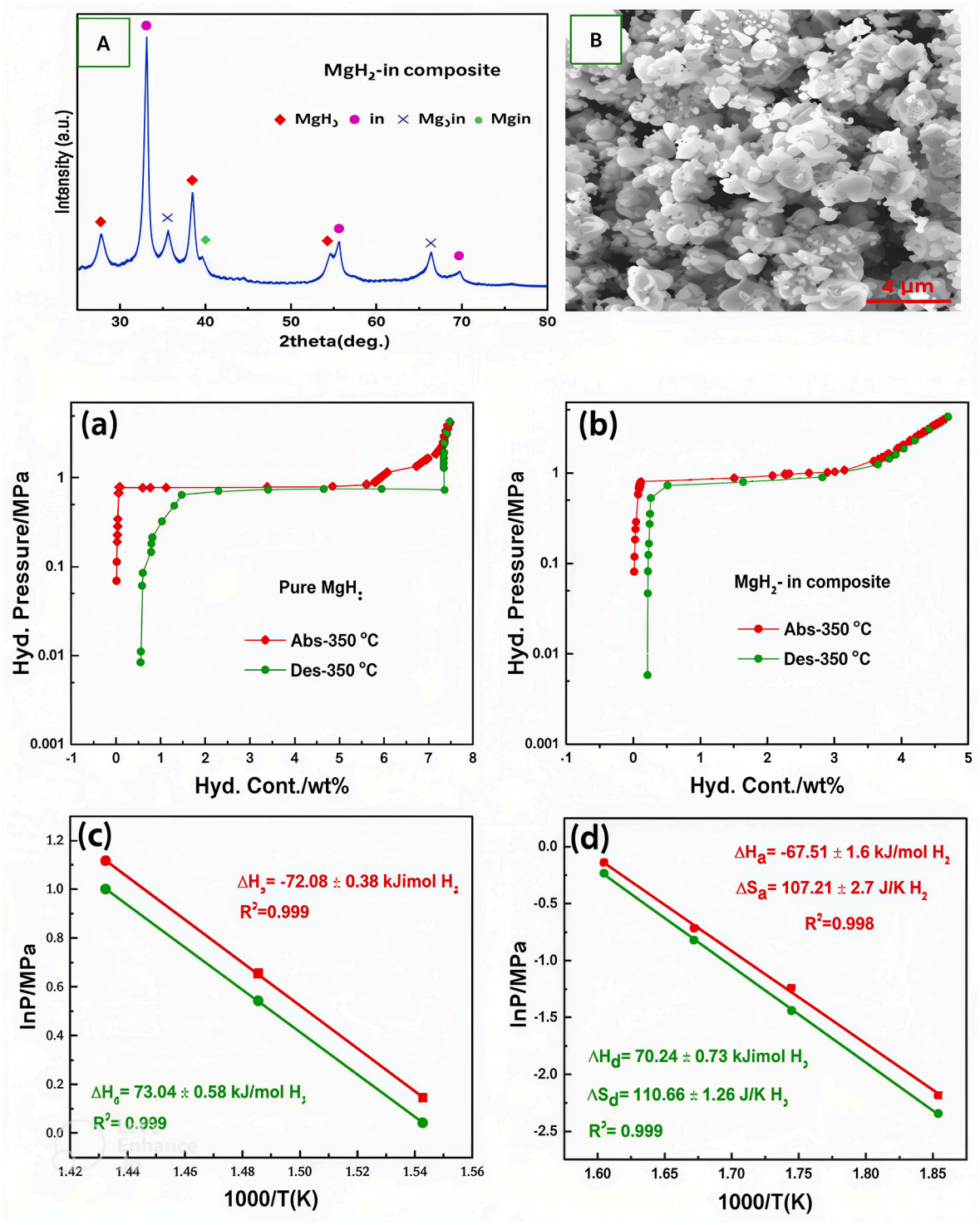


Fig. 8. (A) X-ray diffraction pattern and (B) SEM image of ball-milled MgH_2−In composite; Pressure−composition isotherms recorded at 350 °C and associated van't Hoff plots for (a, c) pure MgH_2 and (b, d) MgH_2−In composite [79] (Reproduced with permission from ACS).

mol H_2). This bracketing arises because Mg introduces a strong hydride-forming character that raises ΔH, while the surrounding TM-rich lattice introduces strain and electronic effects that partially destabilize Mg–H bonds relative to the pure binary. The practical consequence is that Mg-containing HEAs occupy a thermodynamic sweet spot: their desorption temperatures are meaningfully lower than MgH_2, while their gravimetric capacity is higher than TM-only HEAs.

The computational design of HEA compositions exemplifies how this tunability can be exploited deliberately. A Ti–Zr–Mn–Fe–Co HEA designed using a combined CALPHAD, machine learning, and semi-empirical descriptor approach [144] achieved remarkable cycling stability: the equiatomic $Ti_{20}Zr_{20}Mn_{20}Fe_{20}Co_{20}$ composition maintained a hydrogen capacity of 1.6 wt.% at room temperature through the first cycle, declining by only 0.08 wt.% by the tenth cycle (Fig. 11). The non-equiatomic $Ti_{15}Zr_{22}Mn_{27}Fe_{26}Co_{10}$ variant showed comparable initial capacity (1.53 wt.%) with an even smaller capacity fade of just ~0.03 wt.% per cycle demonstrating that fine-tuning the elemental ratios beyond equiatomic composition can improve cycling durability

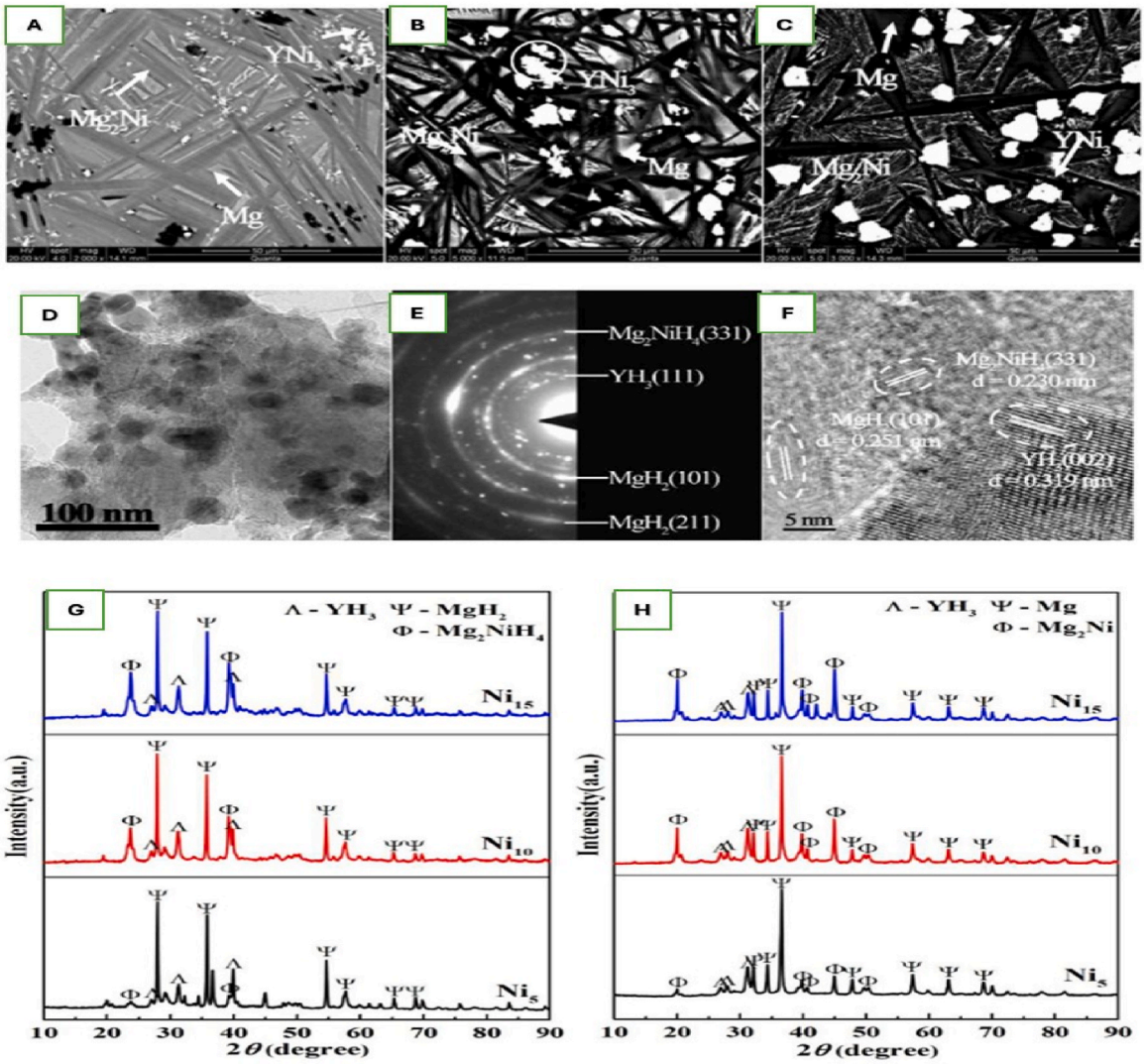


Fig. 9. SEM morphology of as-cast Mg95-X-Nix-Y5 (x ¼ 5, 10, 15) samples: (A) Ni5, (B) Ni10, (C) Ni15; TEM morphology (D), SAED diffraction ring (E) and HRTEM image (F) of the Ni15 samples after hydrogenation; XRD patterns of the Mg95-X-Nix-Y5 (x ¼ 5, 10, 15) samples after hydrogenation (G) and dehydrogenation (H) [140]. (Reproduced with permission from Elsevier).

without sacrificing capacity. This cycling resilience reflects the thermodynamic stability of the multi-element lattice, which resists phase segregation and microstructural degradation under repeated hydrogen-induced volume changes, which that limit long-term performance in nanostructured MgH_2 systems.

The thermodynamic landscape described in this section underscores a recurring challenge in the field: PCT measurements from different laboratories are often not directly comparable. Differences in measurement temperature range, activation protocol, hydrogen purity, equilibration time, and particle size all affect the derived ΔH and ΔS values through contributions from kinetic hysteresis, surface effects, and non-equilibrium absorption.

4.3. Reaction kinetics

The reaction kinetics/mechanisms of magnesium hydrides are governed by complex mechanisms involving hydrogen dissociation, diffusion, and phase transformations. Under vacuum conditions, the activation energy for dehydrogenation averages 111 ± 7 kJ mol^{-1}, closely aligning with Mg–H bond breaking as the rate-limiting step [145]. However, the material-processing route affects the hydrogen storage properties [146,147]. Catalytic additives like Nb_2O_5 and Fe_3O_4 enhance surface reactions [148,149], while aluminum compounds drastically improve kinetics. Mixing MgH_2 with Al reduces dehydrogenation times from 8.6 h to 5.3 h at 300 °C. The AlH_3 further shortens the dehydrogenation time to 44 min by lowering the activation energy to 138.1 kJ mol^{-1} [146,147]. Rehydrogenation at 300 °C and 5 MPa H_2 pressure requires 10 h for full recovery in AlH_3-containing systems.

The thermodynamic-kinetic relationship reveals pressure-dependent mechanisms. Under vacuum, dehydrogenation follows first-order kinetics (F1 model: $f(\alpha) = (1 - \alpha)^{0.94}$) [150], while hydrogen pressure shifts the mechanism to three-dimensional nuclei growth (A3 model) [150]. The equilibrium pressure ratio (p/p^*) critically influences reaction pathways, with lower ratios accelerating dehydrogenation [150]. Destabilisation strategies, such as the use of $LiAlH_4$ additives, leverage intermetallic phases (e.g., $Li_{0.92}Mg_{4.08}$ and $Mg_{17}Al_{12}$) to reduce thermodynamic stability, enabling 10.5 wt.% hydrogen release at 150 °C. [50,151]. Ball-milled MgH_2-AlH_3 composites achieve a 55 °C reduction in onset dehydrogenation temperature due to oxide-free Al* surfaces and optimized particle mixing [151].

Despite substantial progress, challenges persist in achieving low operational temperatures (<200 °C) and maintaining cyclic stability. Recent advances include Mg-Li-Al composites that synergize destabilisation and catalytic effects, achieving faster kinetics through in-situ

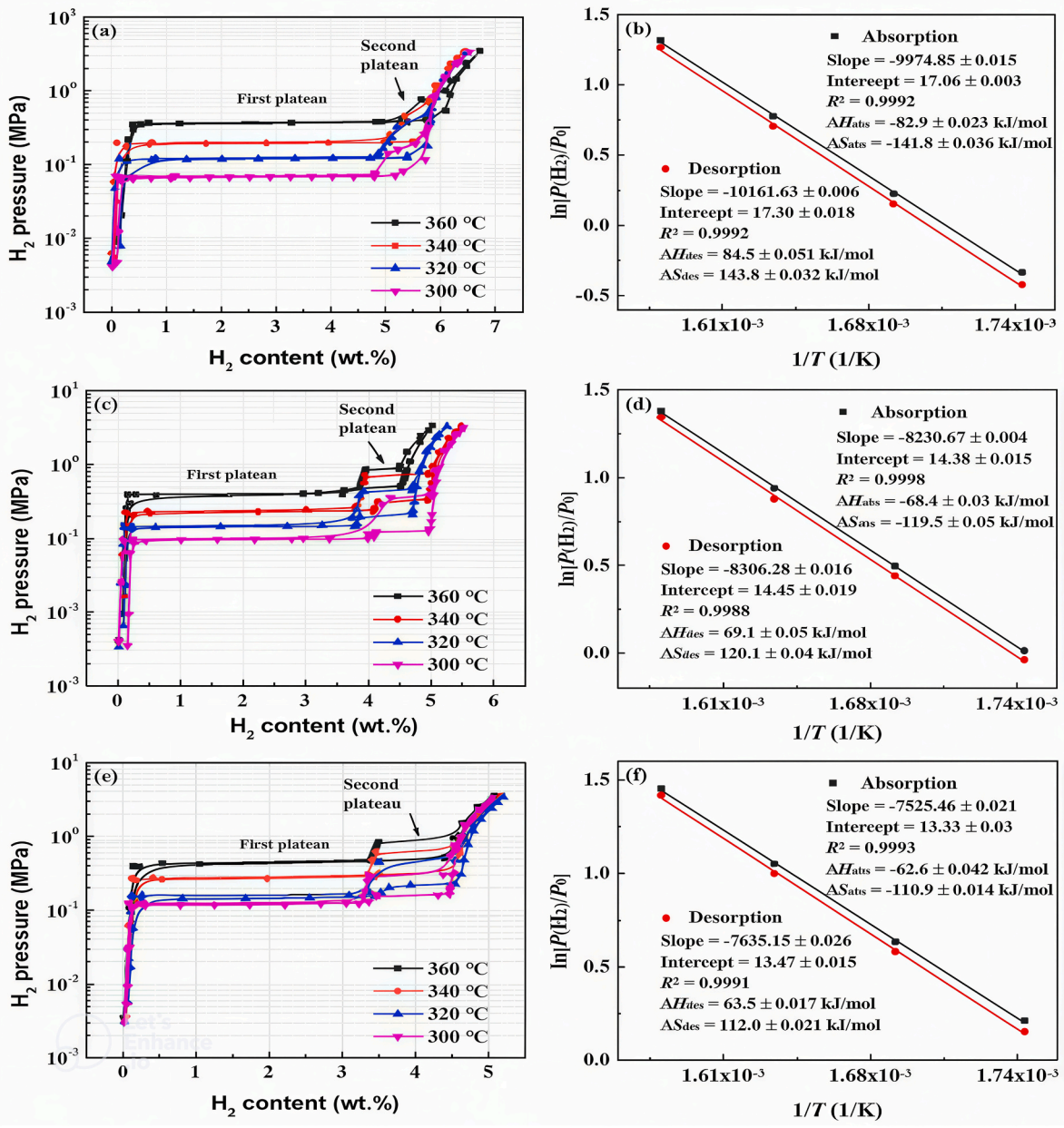


Fig. 10. PCT curves (a, c, e) of the activated Mg_{95-x}-Ni_x-Y_5 (x = 5, 10, 15) samples at different temperatures and the corresponding Van't Hoff graphs; Ni_5 (a, b), Ni_{10} (c, d), and Ni_{15} (e, f) [140] (Reproduced with permission from Elsevier).

reactive phases (eg., LiMgAl intermetallics) that enhance H_2 diffusion and surface reactivity [50,149]. Similarly, HEAs containing transition metals (Ti, Zr, V) display superior hydrogen sorption kinetics, driven by lattice distortion, configurational entropy, and synergistic catalytic effects [152]. Mg-based HEAs, while benefiting from Mg's high gravimetric hydrogen capacity, generally exhibit intermediate kinetics between pure MgH_2 and transition metal-rich HEAs; their reaction rates are improved by proper alloying and microstructural control, but typically do not match the rapid kinetics of TM-HEAs. MgH_2 derivatives and Mg-based HEAs offer promising pathways for balancing storage capacity and kinetics. However, optimizing hydrogen reaction kinetics in Mg-rich HEAs remains a challenge requiring further compositional and processing innovations.

Future research directions should focus on integrating multi-scale kinetic analysis with advanced operando characterization to provide a more detailed understanding of rate-controlling processes. For instance, In-situ TEM and synchrotron XRD can track nucleation and phase boundary migration in real time, revealing kinetic transitions between F_1 and A_3 models. Microreversibility-based models should be coupled with DFT and MD simulations to correlate reaction barriers with thermodynamic parameters such as equilibrium pressure and defect energy states. In addition, ML-driven kinetic modelling can optimize additive composition and process parameters for rapid sorption under low temperature conditions [149].

Moreover, HEAs composed primarily of transition metals (e.g., Ti, Zr, V) demonstrate faster hydrogen sorption kinetics attributed to their lattice disorder and synergistic catalytic effects, which facilitate hydrogen diffusion and decrease hydride stability. Mg-based HEAs, while benefiting from Mg's high gravimetric hydrogen capacity, generally exhibit intermediate kinetics between pure MgH_2 and transition metal-rich HEAs; their reaction rates are improved by proper alloying and microstructural control, but typically do not match the rapid kinetics of TM-HEAs. MgH_2 derivatives and Mg-based HEAs offer promising pathways for balancing storage capacity and kinetics. However,

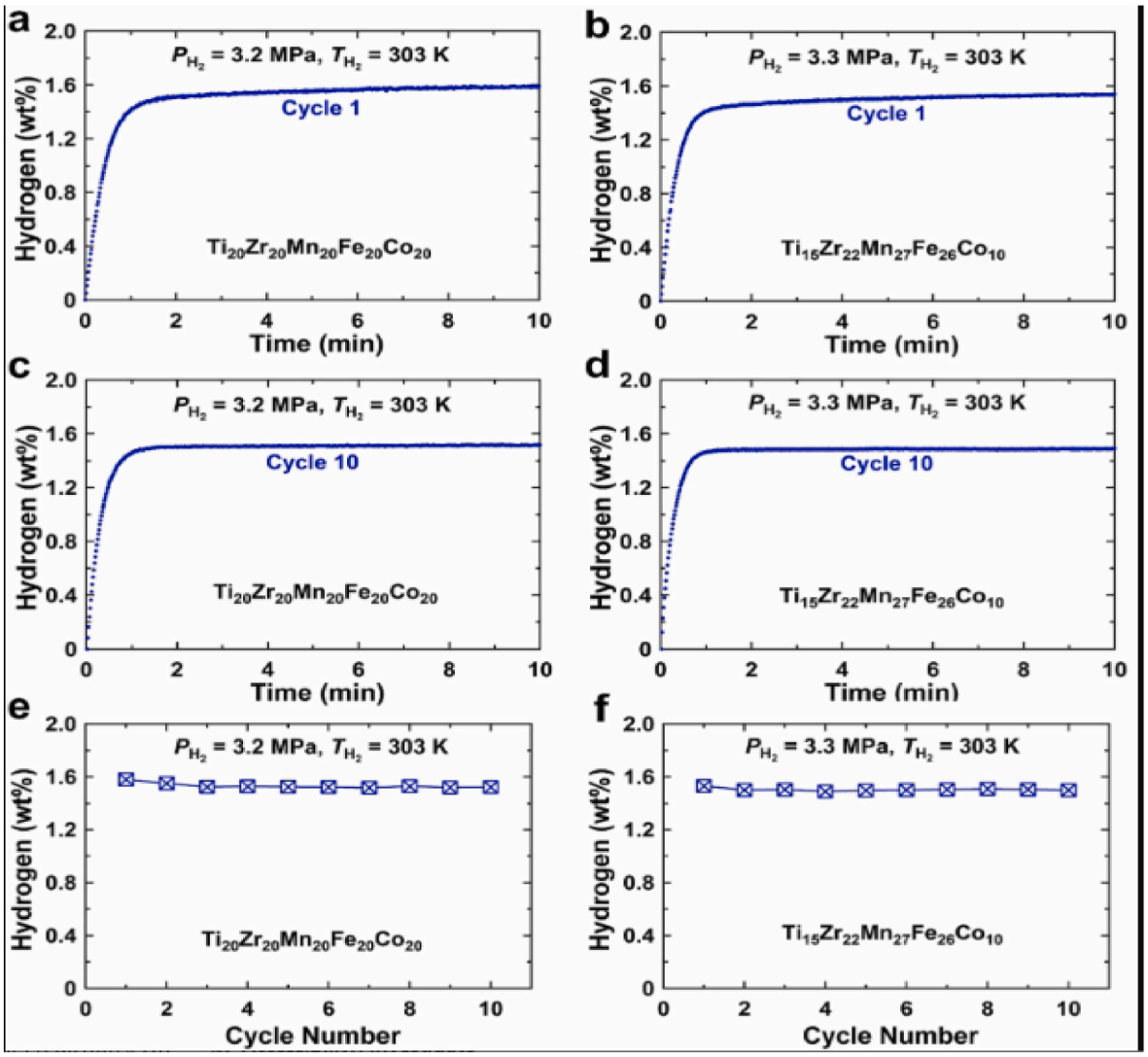


Fig. 11. Room temperature kinetic curves for HEAs $Ti_{20}Zr_{20}Mn_{20}Fe_{20}Co_{20}$ (left) and $Ti_{15}Zr_{22}Mn_{27}Fe_{26}Co_{10}$ (right) in a, c) cycle 1 and b, d) cycle 10 at hydrogen pressures of 3.2–3.3 MPa. Hydrogen storage capacity for e) $Ti_{20}Zr_{20}Mn_{20}Fe_{20}Co_{20}$ and f) $Ti_{15}Zr_{22}Mn_{27}Fe_{26}Co_{10}$ [144] (Reproduced with permission from Elsevier).

optimizing hydrogen reaction kinetics in Mg-rich HEAs remains a challenge requiring further compositional and processing innovations.

4.4. Activation energy

The activation energy (Ea) for hydrogen desorption from Mg-based hydrides varies widely depending on material processing, additives, and composite formulations. Bulk MgH_2 typically exhibits an activation energy of ~140–160 kJ/mol [50], which can be significantly reduced by mechanical milling. Reducing particle size introduces more grain boundaries, defects, and surface sites, which serve as active sites for hydrogen dissociation, absorption, and diffusion [153]. This structural refinement facilitates easier hydrogen absorption and desorption at the atomic level, altering the absorption and desorption pathways. Smaller particle sizes drastically increase hydrogen sorption rates by shortening hydrogen diffusion paths and increasing the number of hydrogen-active sites.

Surfactants-assisted ball-milling has been used for Nb-doped MgH_2. At 186.7 °C, the MgH_2-5 wt.% Nb composite material started to release hydrogen, reaching a maximum hydrogen release of 7.0 wt.%. The desorption and hydrogenation activation energies decreased from 140.51 ± 4.74 and 70.67 ± 2.07 kJ mol^{-1} to 90.04 ± 2.83 and 53.46 ± 3.33 kJ mol^{-1} for the desorption and hydrogenation activation, respectively [154]. Further reduction has been achieved by chemical destabilisation. MgH_2-$LiAlH_4$ composites show Ea values of 121 kJ mol^{-1} [146], while the addition of catalytic additives such as 5 wt.% $SrFe_{12}O_{19}$ can decrease Ea further to about 104 kJ mol^{-1}, enhancing hydrogen release kinetics [155].

In addition, nanostructuring and extended milling further improve kinetics by reducing particle size and increasing surface area (Fig. 12). The larger surface area leads to improved hydrogen absorption and desorption kinetics because more reactive sites facilitate faster hydrogen molecule dissociation and atomic hydrogen diffusion into the bulk material. This improved reactivity reduces the time required to charge and discharge hydrogen and lowers the temperature at which hydrogen release occurs. Milling MgH_2 for 20 h reduces particle size from 900 nm to 13 nm, increases surface area from 1.6 to 33.2 m^2/g. This lowers the onset of dehydrogenation temperature from 410 °C to 335 °C and decreases Ea from 162 kJ mol^{-1} to 94 kJ mol^{-1} [156]. Increasing surface area induces more grain boundaries, which improves the diffusion rate since diffusion of atoms in grain boundaries is much faster than in the entire lattice. Nanostructured MgH_2 exhibits a lower activation energy for hydrogen desorption, facilitating faster kinetics compared to bulk materials [157,158]. With nanostructuring, the desorption temperature can be lowered to below 300 °C, with some studies reporting effective desorption at temperatures as low as 190 °C [159]. Combining

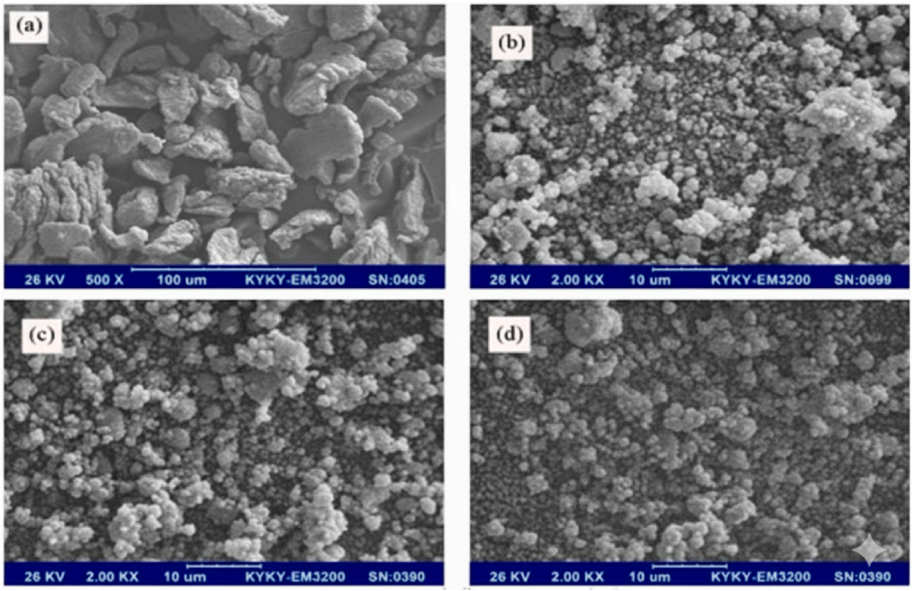


Fig. 12. Scanning electron microscopy micrographs of (a) as-received MgH_2, (b) ball milled for 5 h, (c) 15 h, and (d) 30 h [156] (Under Open Access: CC BY-NC-ND 4.0).

nanostructuring with the right catalysts can have a powerful effect. However, while these improvements are promising, there are also some challenges, such as a reduced ability to be reused over multiple cycles and lower thermal conductivity, which could limit the effectiveness of these materials for long-term hydrogen storage.

Catalytic doping with transition metal oxides and halides has proven effective in lowering kinetic barriers in Mg-based hydrides. For instance, $MnFe_2O_4$-doped and MgH_2-$LiAlH_4$ composites demonstrate rapid hydrogen absorption (3.64 wt.% in 300 s at 300 °C) and desorption (~4 wt.% in 200 s), outperforming undoped samples [160]. Additionally, the addition of TiC and graphene decreased the activation energy from 128.4 kJ/mol to 111.2 kJ/mol, resulting in a 26.3 °C reduction in peak desorption temperature [161]. Additionally, the introduction of a Co@Ni catalyst lowered the activation energy to 93.8 kJ/mol and significantly reduced the onset of dehydrogenation temperature by 160 °C [162].

Five 3D-elements Ti, V, Mn, Fe, and Ni show different catalytic effects on the reaction kinetics of the Mg–H system. Liang et al. reported a rapid desorption rate for MgH_2–V, followed by MgH_2–Ti, MgH_2–Fe, MgH_2–Ni and MgH_2–Mn at low temperatures. The composites containing Ti exhibited the fastest absorption kinetics, followed in order by Mg–V, Mg–Fe, Mg–Mn, and Mg–Ni. Ti has a high affinity for hydrogen and effectively dissociates H_2 molecules into atomic hydrogen at lower temperatures. This lowers the energy barrier for the initial hydrogen uptake step, which is often the rate-limiting step. While the activation energy of desorption for magnesium hydride was reduced drastically, the formation enthalpy and entropy of the hydrides were not altered by ball milling [163].

The presence of these dopants reduces the activation energy for hydrogen absorption and desorption in MgH_2 by accelerating key reaction steps, such as hydrogen molecule dissociation, atomic hydrogen diffusion, and Mg–H bond breaking. Transition metal dopants, such as Ti, Co, Ni, and their compounds (e.g., TiC, Co@Ni), provide active catalytic sites with partially filled d-orbitals that efficiently dissociate H_2 at lower temperatures and form reactive interfaces, promoting hydrogen diffusion in MgH_2. These catalysts also introduce lattice strain and defects, which lower the energy barriers and alter the electronic structures, thereby weakening the Mg–H bonds. Graphene-based dopants enhance kinetics by increasing surface area, improving electronic conductivity, introducing defects that aid hydrogen diffusion, and preventing particle agglomeration. However, their direct catalytic effect on dissociation is moderate. While metal dopants generally achieve greater reductions in Ea and dehydrogenation temperatures due to their strong catalytic activity, combining metals with graphene yields synergistic benefits. Metal nanoparticles catalyse hydrogen reactions while graphene stabilizes these catalysts, enhances electron transport, and improves cycling stability. Thus, the most effective dopants reduce activation energy and improve hydrogen storage performance by combining catalytic hydrogen dissociation with structural and electronic enhancements that facilitate faster, more reversible hydrogen absorption and desorption at lower temperatures.

Furthermore, substituting pure MgH_2 with catalytic alloys significantly lowers Ea for hydrogen desorption, enhancing hydrogen storage kinetics. For example, the ball-milled $Mg_{85}Zn_5Ni_{10}$ alloy exhibits an Ea of 109.83 kJ/mol, which reduces to 75.51 kJ/mol and 82.37 kJ/mol when catalyzed by TiF_3 and NbF_5, respectively, with TiF_3 showing a superior catalytic effect on hydrogen release [164]. Similarly, doping MgH_2 with 10 wt.% Ce-doped $Ti_6Cr_{14}V_{80}$ hydride catalyst decreases Ea further to 62.62 kJ/mol, accompanied by a lowered dehydrogenation temperature and rapid hydrogen release kinetics [165]. Transition metal-based catalysts generally enhance kinetics by forming stable hydrides (e.g., TiH_2, Mg_2NiH_4) or oxides that weaken Mg–H bonds and promote hydrogen diffusion channels [166]. Doping Mg-based alloys with catalytic transition metals can capitalize on their lower activation energies to balance Mg's high hydrogen capacity with enhanced kinetic performance; however, values vary depending on composition and catalyst type.

4.5. *Cycling stability*

The cycling stability of Mg-based hydrides is a critical factor for their practical application in hydrogen storage. This is important in determining the viability of hydrogen storage applications. High cycling stability ensures that the hydrogen storage capacity and kinetics of the storage materials remain consistent over repeated cycles of absorption and desorption. Cycling can induce physical and chemical changes in Mg-based materials, including phase transformations and structural modifications. Degradation of Mg-based hydrides during hydrogen cycling is mainly caused by the formation of surface oxides like MgO. Oxygen atoms tend to occupy the same lattice spaces as the hydrogen

atoms, which block hydrogen diffusion and reduce active sites. Additionally, repeated hydrogen absorption and desorption cause particle agglomeration and grain growth, resulting in the loss of atomic-scale features essential for fast kinetics. Lattice expansion and contraction during cycling lead to the accumulation of lattice strain and structural defects, which can impact the energy barriers for hydrogen reactions.

Furthermore, catalyst loss or segregation, as well as phase transformations into less active forms, reduce hydrogen capacity and slow down kinetics. These combined effects result in decreased storage performance and cycling stability over time, leading to slower kinetics of hydrogen absorption and desorption. Research shows that Mg-based hydrides exhibit a declining stability after multiple cycles. For instance, Huen et al. [167] synthesized MgH_2 via a direct solvent-based method from $MgBu_2$ in four different carbon aerogels. They reported a significant loss of hydrogen capacity after five cycles, attributed to the possible formation of MgO. They also observed hydrogen release of 1.3 to 3.1 wt.% in the first cycle and 1.0 to 1.9 wt.% in the fifth cycle with much slower desorption kinetics.

Nanoscale oxide or fluoride shells formed on Mg-based particles via arc plasma synthesis enhance hydrogen storage by acting as thin, uniform protective coatings that improve oxidation resistance without significantly hindering hydrogen diffusion [29]. These core-shell nanostructures prevent particle agglomeration and preserve active surface area, while providing abundant interfaces that facilitate faster hydrogen dissociation and absorption. The arc plasma method enables rapid vaporization and controlled nucleation, producing uniformly nanostructured particles with tailored shell thickness and composition in a single, scalable, and cost-effective step. This precise control optimizes the balance between protection and hydrogen permeability, resulting in materials with improved hydrogen absorption kinetics and stability compared to other synthesis routes [126].

Modification strategies involving catalysts and composite formation have been effective in enhancing cycling stability. For instance, MgH_2 composites with MXenes like V_2C/Ti_3C_2 exhibit excellent stability due to improved structural integrity and resistance to agglomeration [168]. These MXenes have a unique two-dimensional layered structure that provides a robust and flexible scaffold, helping to distribute MgH_2 particles uniformly and preventing agglomeration during repeated cycles. Carbon scaffolds induce porosity, facilitating hydrogen diffusion and mitigating degradation [167]. Additionally, carbon-based additives, including single-walled carbon nanotubes (SWCNTs), enhance cycling stability by mitigating particle growth and maintaining catalytic activity, although some catalytic effects diminish with increasing cycle numbers. Nanoconfinement within frameworks like $TiNb_2O_7$ nanoflakes or Ni-MOFs prevents particle growth, maintaining active surface areas over cycles [169].

4.6. Direct comparison of Mg-based hydrides and Mg-containing HEAs/CCAs across eight consistent performance metrics

Despite this progress, challenges persist in achieving stability at lower temperatures and in practical conditions. Factors such as catalyst dispersion (e.g., V_2C/Ti_3C_2 MXenes, reducing activation energy by 37%) [168], particle size control and composite homogeneity influence performance. While some systems, such as La-Ni-Fe-V-Mn alloys, retain 1.41 wt.% capacity over cycles [170], degradation mechanisms, such as sintering and oxidation, remain barriers. Ongoing research prioritizes optimizing nanostructuring and hybrid designs (e.g., MgH_2–V_2C–Ti_3C_2 [168]) to balance cycling life, kinetics, and capacity.

Table 5 compares Mg-based hydrides and Mg-containing HEAs/CCAs using eight consistent metrics to make the central capacity-thermodynamic-flexibility trade-off explicit. Pure MgH_2 and RHC composites hold a decisive gravimetric and volumetric advantage: MgH_2 at 7.6 wt.% and RHC systems at 8–10 wt.% reversible capacity are unmatched by any HEA composition. Mg_2FeH_6 records the highest volumetric density of any known complex hydride at 150 kg H_2/m^3. However, all conventional Mg-based hydrides and RHC systems require desorption temperatures of 250–400 °C, face slow kinetics without

Table 5
Direct comparison of Mg-based hydrides and Mg-containing HEAs/CCAs.

Metric	MgH_2	Mg_2NiH_4	Mg_2FeH_6	RHC (MgH_2–$LiBH_4$)	TM-only HEA	Mg-containing HEA/CCA	Key trade-off/note
Gravimetric capacity (wt.% H_2)	7.6 (theoretical); ~6.5–7.0 (practical)	3.6	5.5	8–10 (reversible)	0.2–1.7	1.2–2.7	MgH_2 and RHC far exceed HEAs in gravimetric capacity
Volumetric density (kg H_2/m^3)	110	~80	150 (highest known)	~100 (estimated)	~70–90	~80–100 (estimated)	Mg_2FeH_6 holds the volumetric record across all classes
Desorption enthalpy ΔH (kJ/mol H_2)	−74.5	−64	−98	−40.5 (RHC coupled)	−6.4 to −38.8	−35 to −59	RHC and HEAs occupy the optimal thermodynamic window (−20 to −60)
Desorption temperature T_des (°C)	>300 (1 bar)	250–280	>400	315–400	RT to ~250	~150–350	TM-HEAs enable room-temperature operation; Mg–HEAs are intermediate
PCT plateau character	Flat; single plateau	Flat; two plateaus (phase transition at ~240 °C)	Flat; single plateau	Stepped/two-plateau	Sloped; broad pressure range	Sloped; broader than MgH_2, narrower than TM-HEAs	Sloped HEA plateaus reflect distributed H-binding energies
Cycling stability	Moderate; coarsening and sintering limit long-term stability	Good; intermetallic phase resists coarsening	Good at T below 500 °C; limited reversibility data	Moderate; MgB_2 nucleation barrier slows rehydrogenation	Excellent; entropy-stabilized lattice resists phase segregation	Good; superior to nanostructured MgH_2 composites; less data than TM-HEAs	HEA configurational entropy is an intrinsic cycling stability advantage
Activation energy Ea (kJ/mol)	~140–160 (undoped); ~60–94 (catalyzed)	~100	Not well characterized	~82.5–120 (with catalyst)	Generally low; fast kinetics	Intermediate; faster than MgH_2, slower than TM-HEAs	Mg–HEAs benefit kinetically from multi-element lattice but not as fast as TM-HEAs
Main limitation	High T_des; sluggish kinetics without catalysis	Low capacity (3.6 wt.%)	Very high T_des (>400 °C)	Slow rehydrogenation; high operating temperature	Low gravimetric capacity (below 2 wt.%)	Capacity lower than MgH_2; sloped PCT complicates engineering design	No single material class resolves all four challenges simultaneously

catalytic modification, and suffer from coarsening-related cycling degradation under extended operation.

Mg-containing HEAs occupy a genuinely different region of the design space: their ΔH values (−35 to −59 kJ/mol H_2) sit squarely within the thermodynamically ideal window for near-ambient operation, their PCT curves are characteristically sloped (reflecting distributed H-binding environments rather than a single-phase transformation), and their configurational entropy provides an intrinsic structural resilience against phase segregation under cycling. The price of these thermodynamic and stability advantages is gravimetric capacity: current Mg-containing HEAs report 1.2–2.7 wt.% H_2, roughly one-third of the MgH_2 theoretical value. The most promising compositional strategies for bridging this gap are those that increase the Mg molar fraction in HEA compositions beyond the ~10–30 at.% typical of current reports, incorporate light elements (Al, V, Ti) to reduce alloy density without sacrificing the hydride-forming character conferred by Mg, and exploit reactive hydride composite principles within HEA architectures, combining the thermodynamic flexibility of multi-principal-element design with the coupled dehydrogenation pathways that have proven effective in MgH_2–$LiBH_4$ systems. None of the material classes reviewed in this section resolves all four key challenges (capacity, thermodynamics, kinetics, and cycling stability), which reinforces the need for the integrated computational-experimental design approaches.

5. Processing routes for Mg-based hydrides and alloys

A comprehensive review of the some manufacturing routes for magnesium-based hydrides, highlighting the various processes, as well as their advantages and disadvantages are presented. Among the several processing routes explored for the manufacturing of magnesium hydrides, high-energy ball milling, reactive milling, mechanical alloying, arc plasma technology, nanoscaffold confinement, severe plastic deformation, and electrochemical reduction have been widely used.

5.1. *High-energy ball milling and mechanical alloying*

High-energy ball milling has been widely used for the processing of Mg-based materials and HEAs for hydrogen storage. High-energy ball milling induces repeated welding, fracturing, and rewelding of particles, reducing particle size, creating defects, and dispersing catalysts within powder particles. The process involves high-energy grinding of magnesium (Mg) or pre-formed MgH_2 powder in a planetary or vibratory mill, often under a hydrogen atmosphere (5–20 bar). High-energy ball milling also introduces a fine dispersion of additives with catalytic effects (such as transition metal oxides or fluorides). The uniform distribution of fine additives promotes fast absorption/desorption kinetics in MgH_2 [171]. Also, a combinatorial planetary ball milling system with a 16-chamber vial enables high-throughput synthesis of solid-state hydrogen storage materials, facilitating rapid screening of variables such as milling time and catalyst additives under consistent conditions [172]. These approaches accelerate optimization of hydrogen storage properties while maintaining effective material processing. Fig. 13 shows a schematic diagram of a ball milling process.

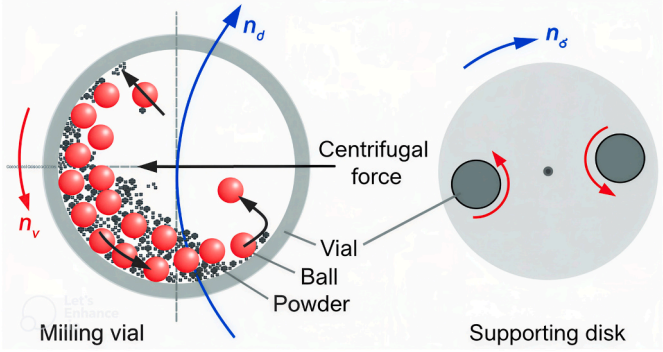


Fig. 13. Ball milling process [174].

The mechanical alloying technique for Mg-based alloys typically involves high-energy ball milling of magnesium powder with other alloying elements, creating a unique microstructure that enhances hydrogen absorption and release kinetics. The mechanical alloying procedure is simple, low-cost, and utilizes basic equipment, including planetary ball mills, attritor ball mills, and vibratory ball mills. Also, under the heat of positive mixing, mechanical alloying can alloy two metals and can synthesize metastable alloys, amorphous alloys, or quasicrystals [153] Conventional melting and casting methods are generally unsuitable for Mg-based alloys such as MgFe, MgCo, MgNb, and MgTi because these systems often exhibit significant differences in melting points, vapor pressures, and a lack of solid solubility between magnesium and the transition metals (Fe, Co, Nb, Ti). These systems can be fabricated by mechanical alloying, in addition to any other pairs or more complex mixtures of metals and non-metals. This method is particularly effective in overcoming the challenges associated with Mg's surface oxide layer and in achieving the desired nanostructures for efficient hydrogen storage [173].

Mechanical alloying parameters, such as milling time, ball-to-powder ratio, milling speed, and milling atmosphere, critically influence the microstructure and hydrogen storage properties of magnesium-based alloys by controlling particle and grain size reduction, microstrain, and lattice distortion. These microstructural changes shorten hydrogen diffusion distances, create defects like vacancies and grain boundaries that enhance diffusion pathways, and locally destabilize hydrides, thereby lowering the hydrogen desorption temperature and activation energy [174]. Longer milling times and higher energy input intensify these effects, improving hydrogen absorption and desorption kinetics, while the milling atmosphere affects surface oxidation and adsorption behaviour [175]. Together, these factors synergistically enhance the kinetics, thermodynamics, and capacity of Mg-based hydrogen storage materials.

A study by Huang and Mose shows that ball milling significantly modifies the microstructure of AZ61 magnesium alloy by drastically reducing particle size (from ~68 μm to ~16 μm) and introducing strain-induced defects. These microstructural refinements enhance hydrogen storage capacity (up to 5.5 wt.%) and improve hydrogen absorption/desorption kinetics by shortening diffusion paths and increasing active sites for hydrogen interaction. However, ball milling does not substantially alter the intrinsic thermodynamic properties of the hydride phases, as the desorption activation energy remains comparable to that of commercial MgH_2 [176].

Milling speed plays a crucial role in balancing the benefits of microstructure and defect formation. Fig. 14 shows the morphological changes in MgH_2 at different ball milling speeds. Fig. 14 (a) shows rounded samples of as-received MgH_2 samples. Fig. 14b and (c) indicate almost rounded particles due to low milling speed. In Fig. 14 (d), MgH_2 samples appear to have flat surfaces. These changes in the morphology of the powders influence the sorption process due to alterations in the number of active sites for hydride formation and dissociation.

Milling time affects the hydrogen storage performance of Mg-based materials. Increasing milling time generally leads to enhanced hydrogen absorption/desorption kinetics by refining particle and grain sizes, increasing the content of nanocrystalline and amorphous phases, and introducing lattice strain and defects that facilitate hydrogen diffusion and reduce the activation energy for desorption. Milling times in the range of 4 to 10 h often yield optimal performance, significantly lowering the hydrogen desorption activation energy (typically between 60 and 80 kJ/mol) and reducing desorption temperatures. Mechanically milling MgH_2 for 5 h decreased its decomposition temperature from 402 °C to 389 °C due to the formation of a nanocrystal, accumulation of the lattice strain, formation of metastable γ-MgH_2 phase, and the reduction of MgH_2 particle size from 32 μm to 1.7 μm. The addition of Ti-

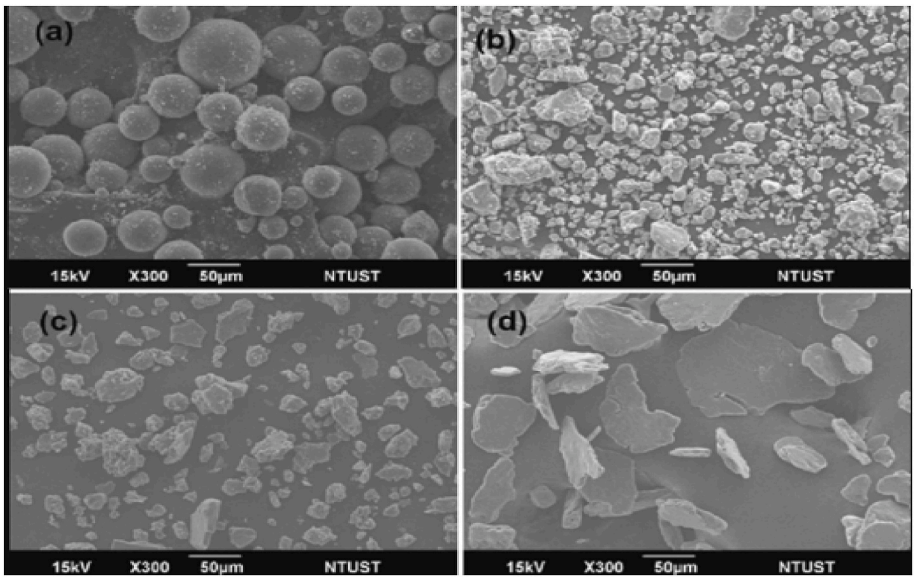


Fig. 14. SEM images of; (a) as-received MgH_2 sample, (b) and (c) low speed milled samples; (d) high speed milled samples [176] (Reproduced with permission from Elsevier).

based alloy to magnesium hydride and mechanical alloying for 15h reduced the dehydrogenation temperature of magnesium hydride from 399 °C to 345 °C and an average particle size of 0.8 μm, which was lower than that of milled MgH_2 powder (1.7 μm) at the same conditions [177]. (See Fig. 15).

XRD analysis of the $NaAlH_4$-MgH_2 composite confirmed that milling progressively altered the phase composition, with $NaAlH_4$ peaks diminishing and new phases including Na_3AlH_6/$NaMgH_3$ and Al/$Al_{0.95}Mg_{0.05}$ emerging as milling extended from 1 min to 6 h (Fig. 16A and B). After dehydrogenation at 350 °C, both the 1 min and 2 h milled samples transformed into $Al_{12}Mg_{17}$, AlMg, and Al_3Mg_2 intermetallic phases alongside NaH, indicating similar final phase assemblages regardless of milling duration (Fig. 16C and D). The dehydrogenation curves (Fig. 16E) revealed that increasing milling time from 1 to 360 min significantly lowered the onset desorption temperature, with the 120 and 360 min samples beginning hydrogen release near 100 °C compared to approximately 150 °C for the 1 min sample. The isothermal desorption profiles (Fig. 16F) further demonstrated that more extensively milled samples, particularly those processed for 120 and 360 min, completed desorption considerably faster and at lower temperatures, releasing approximately 6 wt.% hydrogen well before the 1 min sample reached comparable values. Beyond 120 min of milling, the kinetic gains became marginal, suggesting 120 min as the practical optimum for this system [178].

The formation of catalytic phases, such as MgSe, Mg_2NiH_4, $Al_{11}La_3$, and MgF_2, as well as related intermetallics, during mechanical alloying or ball milling significantly enhances Mg-based hydrogen storage materials. These phases act as catalysts for hydrogen reactions, lowering desorption temperatures and activation energies, thereby enhancing hydrogen diffusion and facilitating rapid and efficient hydrogen absorption and release. When combined with structural additives like graphene, these effects are synergistically amplified, making these composites promising for real-world hydrogen storage technologies. MgH_2–$NiSe_2$ composites were prepared via mechanical ball milling using hydrothermally synthesized $NiSe_2$ and MgH_2. They observed that increasing the $NiSe_2$ content reduced the desorption peak temperature from 375 °C to 307 °C, and enhanced kinetics due to the formation of in-situ MgSe/Mg_2NiH_4 catalytic phases [179].

In another study, Mg2.3Y0.1Ni + x wt.% graphene composites (x = 1–7) fabricated via mechanical ball milling, show Mg_2Ni, Mg, $MgNi_2$, and Ni_3Y phases. Graphene at alloy edges enhanced H_2 diffusion channels, with 7 wt.% graphene eliminates the gestation period, and 3 wt.% graphene optimizes performance. They achieved 3.251 wt.% H_2 absorption in 2 min (90.21% capacity) and 3.389 wt.% H_2 release in 10 min (99.04% capacity) at 300 °C. The 3 wt.% graphene composites exhibited a low dehydrogenation activation energy and reduced desorption enthalpy (67.5 kJ/mol) [180].

High alloy complexity (ternary/quaternary systems) tends to extend

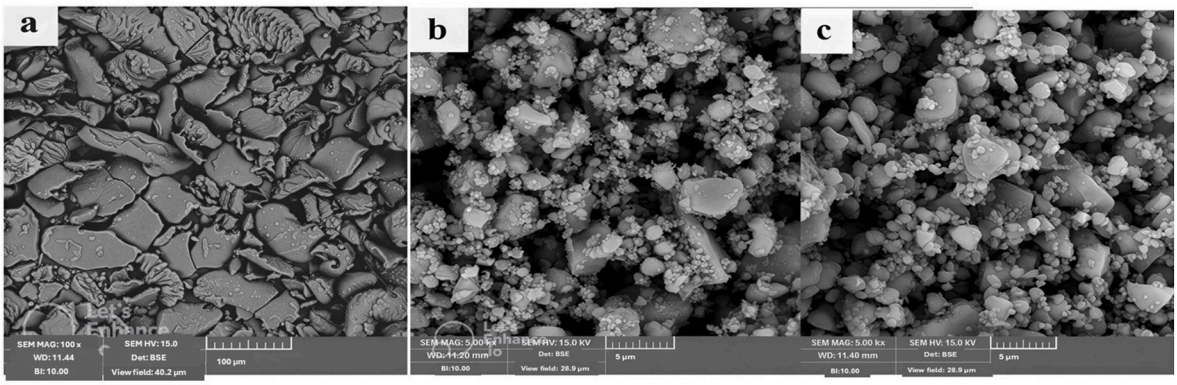


Fig. 15. SEM micrograph of MgH_2 powder for (a) un-milled; (b) milled for 5h; and (c) milled for 15 h [177] Open Access license (CC BY-NC 4.0).

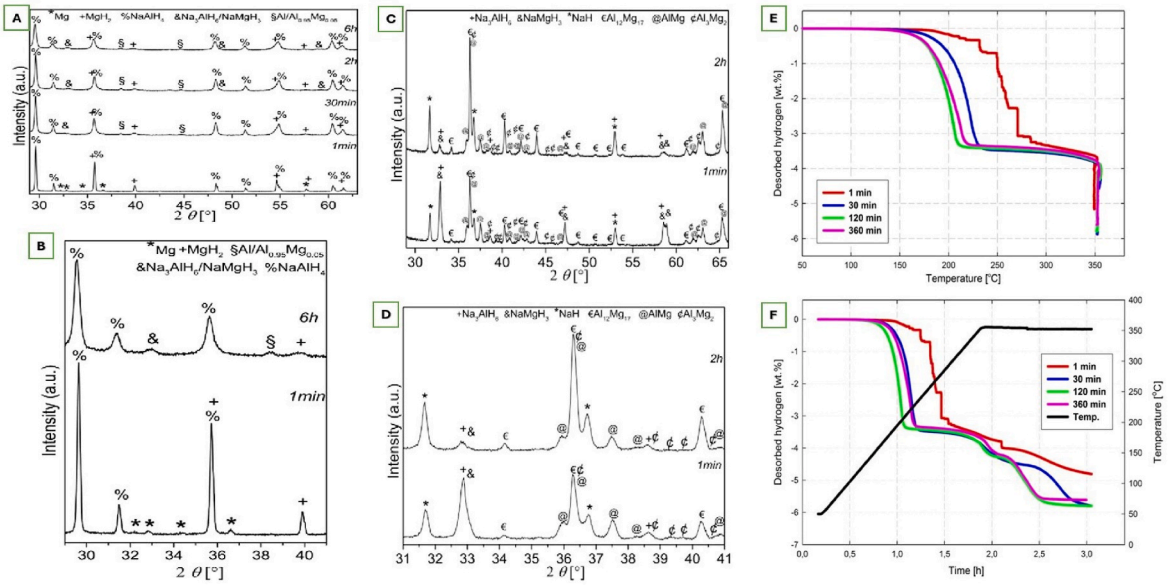


Fig. 16. XRD patterns of $NaAlH_4$-MgH_2 mixtures after ball-milling (1 min–6 h) and dehydrogenation at 350 °C (A–D), and dehydrogenation properties of $NaAlH_4$–MgH_2 (1:1) ball-milled for 1–360 min: hydrogen desorption vs. temperature (E) and vs. time (F) [178] (Reproduced with permission from Elsevier).

cycle life; however, it may somewhat reduce discharge capacity, highlighting the need for a balanced capacity with durability. The $Mg_{90}Ni_5Y_5$ alloy was synthesized via vacuum electromagnetic induction melting followed by ball milling. The alloy achieved full activation after two cycles, with a maximum hydrogen desorption capacity of ~5.1 wt.%. They concluded that ball milling reduced the dehydrogenation activation energy to 75.7 kJ/mol, significantly improving kinetics [181]. $Mg_{2.4-x}Y_xNi$ alloys (x = 0.05–0.2) alloy was prepared via vacuum high-frequency induction melting followed by mechanical crushing/ball milling The $Mg_{2.3}Y_{0.1}Ni$ alloy exhibited optimal kinetics, achieving 90% hydrogen absorption in 6 min and desorption in 3.4 min at 300 °C, alongside high saturation rates (80.17% absorption, 96.02% desorption) and reduced hydrogen release activation energy (113.1–123.9 kJ/mol) [182].

Mg-containing HEAs synthesized via high-energy ball milling exhibit promising hydrogen storage behaviour characterized by moderate hydrogen capacities, enhanced absorption kinetics, and stable phase transformations between BCC solid solutions and FCC hydrides. Wu et al. prepared $Mg_{10}Ti_{30}V_{25}Zr_{10}Nb_{25}$ through the mechanical alloying method and could absorb hydrogen at room temperature without activation. This alloy can absorb hydrogen at room temperature without activation, with a hydrogen absorption capacity of approximately 1.196 wt.%. The dehydrogenation activation energy of the composites reduces from 121.94 ± 4.08 to 91.66 ± 1.31 kJ $mol^{-1.}$ [65]. A_2B-type $MgTiNbCr_{0.5}Mn_{0.5}Ni_{0.5}$ alloy and its derivative $Mg_{0.68}TiNbNi_{0.55}$ alloys were prepared by mechanical alloying and reactive milling, respectively. Both alloys present a total gravimetric capacity of around 1.6 wt.% H_2 [134]. $MgZrTiFe_{0.5}Co_{0.5}Ni_{0.5}$ HEA was synthesized by high-energy ball milling (HEBM), which presents a BCC structure and can absorb up to 1.2 wt.% H_2 [136]. MgAlTiFeNi processed by HEBM showed a hydrogen storage capacity of 0.94 wt.% [183]. Furthermore, ball-milled MgVCr and MgTiVCrFe can reversibly absorb 0.95 and 0.37 wt.% of hydrogen, respectively. [184]. $Mg_{0.10}Ti_{0.30}V_{0.25}Zr_{0.10}Nb_{0.25}$ alloy was synthesized by HEBM. The alloy adopted a single-phase BCC lattice and can absorb 2.7 wt.% hydrogen within 1 min at room temperature conditions [64].

Mechanical ball milling plays a crucial role in optimizing Mg-based hydrogen storage materials by inducing grain refinement, forming an amorphous phase, and reducing particle size, which collectively enhances nucleation and hydrogen diffusion. Nanostructuring and the development of catalytic phases through alloying and catalyst addition improve hydrogen storage kinetics, wheras thermodynamic properties showed limited change. Refined microstructures with high densities of grain boundaries, defects, and interfaces serve as active sites for hydrogen absorption, reducing diffusion distances and facilitating hydride formation. These features, along with strain-induced effects and catalytic multiphase interactions, lower energy barriers for hydrogen uptake and release. Despite some contradictory findings regarding milling duration and thermodynamic impacts, precise process control and further research into thermodynamic destabilisation remain important for advancing Mg-based hydrogen storage technologies. Table 6 summarizes various Mg-based alloys processed by high-energy ball milling and mechanical alloying methods, along with their respective hydrogen storage properties.

5.2. *Reactive ball milling*

Reactive ball milling (RBM) is a technique in which starting materials are milled together under a controlled reactive gas atmosphere, such as hydrogen or nitrogen, allowing both mechanical alloying and in-situ chemical reactions to occur simultaneously [185]. This method is widely used to synthesize compounds such as metallic hydrides and nitrides, at room temperature. The mechanical energy and repeated collisions during milling activate solid-gas reactions between the powders and the surrounding gas. In hydrogen storage research, RBM enables direct formation of hydrides (e.g., MgH_2) by milling metal powders under hydrogen, making it a powerful tool for fabricating advanced functional materials with tailored properties [186].

High-temperature, high-pressure reactive ball milling (HTHPRBM) of Mg-Ni mixtures under hydrogen rapidly synthesizes MgH_2 in ~40 min (even at 250 rpm), leveraging elevated temperatures (up to 325 °C) to accelerate kinetics. However, Ni agglomeration limits Mg_2NiH_4 formation, yielding trace amounts only above 250 °C, as Ni primarily acts as a catalyst for Mg hydrogenation. This highlights the potential of HTHPRBM for fast hydride synthesis but underscores challenges in targeting complex ternary hydrides [187]. In addition, MgH_2-10 wt.% $TiMn_2$ nanocomposite, synthesized via reactive/high-energy ball milling and cold-pressing by [188] achieves ultra-fast 5.1 wt.% H_2 absorption/desorption (100s/400s at 225 °C) with low activation energies (19.3/82.9 kJ/mol), 414 stable cycles, and 150 ml/min H_2 flow for fuel

Table 6
Summary table of materials, processing route, and results observed.

Material	Processing Route	Key Additives/ Phases	Hydrogen Capacity (wt. %)	Absorption Kinetics	Desorption Kinetics	Activation Energy (kJ/mol)	Enthalpy (kJ/ mol)	Ref
MgH_2	Combinatorial planetary ball milling (16-chamber vial)	Various catalysts	Up to 6.8	Not specified	Not specified	~94 (dehydrogenation)		[172]
$Mg_{2-4-x}Y_xNi$ (x = 0.05–0.2)	Induction melting + crushing + ball milling	Mg_2Ni, Ni_3Y		90% in 6 min (300 °C)	90% in 3.4 min (300 °C)	113.1–123.9 (desorption)		[182]
$Mg_{0-93}Al_{0-07}$-5 wt.%LaF_3	Ball milling	$Al_{11}La_3$, MgF_2		Not specified	Not specified	65 (hydriding), 78 (dehydriding)	69.7 (dehydriding)	[187]
$Mg_{2-3}Y_{0-1}Ni$ + x wt.% graphene	Ball milling	Mg_2Ni, $MgNi_2$, Ni_3Y, graphene	3.251–3.389	3.251 wt.% in 2 min (300 °C)	3.389 wt.% in 10 min (300 °C)	67.5 (3 wt.% graphene)		[180]
Mg_2Ni-based alloys	High-energy ball milling (2–4h)	Cr, Mn		Enhanced with Mn	Enhanced with Mn	Reduced with Cr/ Mn	Reduced with Cr	[188]
$La_7Sm_3Mg_{80}Ni_{10}$	Casting + ball milling	Not specified	4	4 wt.% in 50–108 s (200 –280 °C)	Onset at 274.4 °C	80.79 (milled)	76.52–77.13	[189]
AZ61 alloy	Ball milling	MgH_2, minor AlH_3	5.5	Not specified	Not specified	188.9 (desorption)	Not specified	[176]
$Mg_{90}Ce_3Ni_7$	Induction melting + ball milling	Mg, Mg_2Ni, $CeMg_{12}$	3.5–5	3.5 wt.% in 30 min (100 °C)	5 wt.% in 10 min (280 °C)	72.2 (dehydrogenation)		[190]
$La_7Ce_3Mg_{80}Ni_{10}$	Ball milling (10h)		4	4 wt.% in 80 s (200 °C)	3 wt.% in 191 s (300 °C)	62.9 (desorption)		[191]
$PrMg_{12}$ + 30 wt.% Ni	Ball milling	$PrMg_{12}$, Ni, Mg_2Ni				79.86 (10h milling)	Stable	[192]
$Mg_{90}Ni_5Y_5$	Induction melting + ball milling	MgH_2, Mg_2NiH_4, YH_2/YH_3	~5.1		~5.1 wt.%	75.7 (dehydrogenation)		[181]
$Mg_{95}Ni_2Pr_3$	Ball milling (0–20h)	Nanocrystalline/ amorphous	4.499	4.499 wt.% in 10 min (280 °C)		59.66 (10h milling)	−75.60	[193]
$NdMg_{12}$ + Ni	Ball milling	Mg_2Ni				114.5 (10 wt.% Ni)	80.3 (5 wt.% Ni)	[194]
$NdMg_{12}$-Ni	Ball milling (0–8h)	Mg_2Ni		95% in 180 s (330–350 °C)		115.30 (8h milling)	74.61 (absorption, 6h)	[194]
$Mg_{0.65}TiNbNi_{0.55}$	High-energy ball milling	FCC hydride (MH_2 with CaF_2-type structure)	0.8		0.8 wt.% @ 380 °C			[134]
$MgZrTiFe_{0.5}Co_{0.5}Ni_{0.5}$	High-energy ball milling	BCC structures& FCC high entropy hydride	1.2	1.0 wt.% H_2 in 30 min @ 350 °C				[136]
MgAlTiFeNi	High-energy ball milling	BCC	0.94		0.81 wt.% in less than 50 s.			[183]
MgVCr	High-energy ball milling	BCC	0.95	0.5 wt % @ 30 °C				[184]
MgTiVCrFe	High-energy ball milling	BCC	0.37	0.2 wt % @ 350 °C				[184]
$Mg_{0.10}Ti_{0.30}V_{0-25}Zr_{0.10}Nb_{0.25}H_{1.72}$	Ball milling	FCC	1.72 H/M 2.70 wt.%					[64]
$Mg_{0.10}Ti_{0.30}V_{0.25}Zr_{0.10}Nb_{0.25}H_{1.53}$.	Ball milling	FCC	1.53 H/M 2.41 wt.%					[64]
$Mg_{0.10}Ti_{0.30}V_{0.25}Zr_{0.10}Nb_{0.25}H_{1.65}$	Reactive ball milling	FCC	1.65 H/M 2.60 wt.%					[64]

cells (3A/5.5V output), demonstrating efficient solid-state hydrogen storage.

Nanocrystalline MgH_2 synthesized via 200 h reactive ball milling (RBM) under 50 bar H_2 (β/γ phases, ~10 nm grains) achieved 500/2500 s absorption/desorption at 250 °C. Adding 5 wt.% Ni + 5 wt.% Nb_2O_5 via 50 h RBM produced a nanocomposite with enhanced kinetics: 41 s absorption and 121 s desorption (5 wt.% H_2) at 250 °C, supported by low activation energies (β-phase: 68 kJ/mol; γ-phase: 74 kJ/mol). The Ni/Nb_2O_5 synergy enhanced catalytic activity, defect density, and H_2 diffusion, allowing for rapid cycling without degradation [189]. Similarly, Farina et al. [190] synthesized MgH_2-Mg_2FeH_6 nanocomposites via reactive ball milling. The nanocomposite exhibits enhanced kinetics with >4 wt.% H_2 release in <100s above 340 °C and electrochemical capacity >1400 mAh/g, while Fe-based catalysts (e.g., FeNi/rGO, Fe_7S_8) improve cycling stability (e.g., 93.4–100% retention) by forming active phases (Mg_2NiH_4, Mg_2FeH_6) that lower activation energies (e.g., 19–82 kJ/mol) and accelerate H_2 dissociation. Nanocrystalline structures (~10 nm) and synergistic catalysts optimize hydrogen storage capacity (up to 5.2–6.9 wt.%) and reversibility across thermal/-electrochemical systems.

Nanocrystalline MgH_2 (β/γ phases, ~10 nm grains) was prepared through reactive ball milling for 200 h under 50 bar H_2. It takes 8.3/

44.6 min for the absorption/desorption of H_2 to occur at 250 °C. Adding 5 wt.% Ni + 5 wt.% Nb_2O_5 via 50h RBM yielded a nanocomposite with enhanced kinetics: 41s absorption and 121s desorption (5 wt.% H_2) at 250 °C, driven by low activation energies (β: 68 kJ/mol; γ: 74 kJ/mol). The Ni/Nb_2O_5 synergy provided catalytic sites and defects, enabling 180 stable cycles with ~5.46 wt.% H_2 capacity retention, demonstrating robust cyclability without degradation [190].

Reactive Ball Milling achieves these breakthroughs in hydrogen storage properties, particularly cyclability, because it creates nanocrystalline hydrides (e.g., grains of ~10 nm), which shorten hydrogen diffusion pathways. RBM increases active surface area, leading to accelerated kinetics. It also facilitates the in-situ formation of catalytically active phases (e.g., Mg_2NiH_4, Mg_2FeH_6) from additives like Ni, $TiMn_2$, or Fe, which significantly lower activation energies by acting as efficient hydrogen dissociation/recombination sites. Moreover, these additives often work synergistically (e.g., Ni/Nb_2O_5) to further enhance catalytic activity, defect density, and H_2 diffusion. Furthermore, RBM introduces a high density of defects and lattice distortions, providing fast diffusion channels for hydrogen. The resulting nanoconfinement and improved structural integrity actively suppress particle agglomeration and sintering, which are primary causes of degradation, thereby maintaining high active surface areas and crystallographic stability over hundreds of absorption/desorption cycles. These combined effects manifest in the fast kinetics, reduced activation energies, and long-term cyclability observed in Mg-based alloys.

5.3. Arc plasma method

Arc plasma is an effective physical vapor deposition technology to prepare metal nanoparticles. The process utilizes arc plasma to heat the metal block, followed by metal vaporization, nucleation, and deposition. In the arc equipment, a large temperature gradient exists between the arc source and the cooling zone (See Fig. 17 for a schematic diagram of an Arc Plasma equipment). Metals vaporize into a supersaturated state, travel through a short distance, and enter the high-temperature growth regime with a sudden drop in temperature [29]. The vaporized sample instantaneously forms ultrafine particles, which grow continuously in the high-temperature growth zone. In the arc plasma method for preparing Mg-based alloys, magnesium, which has a low melting point, nucleates first, followed by other alloying elements (mostly transition metal elements) attaching to the magnesium particles to form a shell with a layer thickness between a few nanometres due to their small concentrations in the alloy [191].

The arc plasma method enables the formation of Mg-based materials with nano-sized oxide or fluoride shells. These materials show improved hydrogen absorption kinetics and oxidation resistance compared to pure magnesium. The arc plasma method offers significant advantages for magnesium-based hydrogen storage materials, including the ability to produce nanostructured and core-shell composites with high surface area. This improves hydrogen absorption kinetics and enhances resistance to oxidation due to the presence of nano-sized oxides. The equipment is relatively low-cost and has scalable production [29].

Core-shell structured Mg-MF_x (M = Ni, La, V, and Ce) nanocomposites were synthesized using the arc plasma method. The Mg_2Ni and MgF_2 shells that formed on the Mg particles contributed to the improved hydrogen absorption kinetics of the Mg-NiF_2 composite, even at low temperatures. At 200 °C, it could absorb 3.85 wt.% H_2 in 60 s, while at 100 °C, it could absorb 3.26 wt.% H_2 in 2 h. Additionally, the hydrogen absorption kinetics of RE oxides produced on Mg particles were superior to those of the Mg-VF_3 composite. Additionally, as compared to pure magnesium made using the same technique, all of the Mg-MFx composites displayed better hydrogen absorption kinetics [192].

Catalytic phases in Mg/MgH_2 particles improve the sorption properties of Mg-based materials. For example, Mg@Ni nanocomposite powder prepared through the arc plasma evaporation of pure Mg followed by electroless plating of Ni on Mg ultrafine particles in a $NiCl_2$ bath shows a low hydrogenation enthalpy of −73.6 kJ/mol H_2 and a maximum hydrogen capacity reaching 6.1 wt.% at 350 °C under a hydrogen pressure of 4.3 MPa. This capacity is slightly higher than that of pure ultrafine powder (5.7 wt.%). The improved hydrogen sorption properties stemmed from Mg_2Ni/Mg_2NiH_4 phases on Mg/MgH_2 ultrafine particles after cycles of de/hydrogenation [193]. Similarly, Mg–Ce_2O_3 nanocomposite powders were prepared through arc plasma evaporation using a Mg–5 wt.% CeO_2 mixture, followed by passivation in air [194]. The Ce_2O_3 particles adhered to the surface of Mg particles, creating a core-shell structured metal-oxide nanocomposite. The composite's hydrogenation and dehydrogenation enthalpies were −71 kJ/mol H_2 and 75.41 kJ/mol H_2, respectively, and its activation energy for hydrogen absorption was 47.75 kJ/mol H_2. The composite also absorbed 4.07 wt.% of hydrogen at 50 °C in 10 h. These findings demonstrated that a small amount of Ce oxide added to Mg using the arc

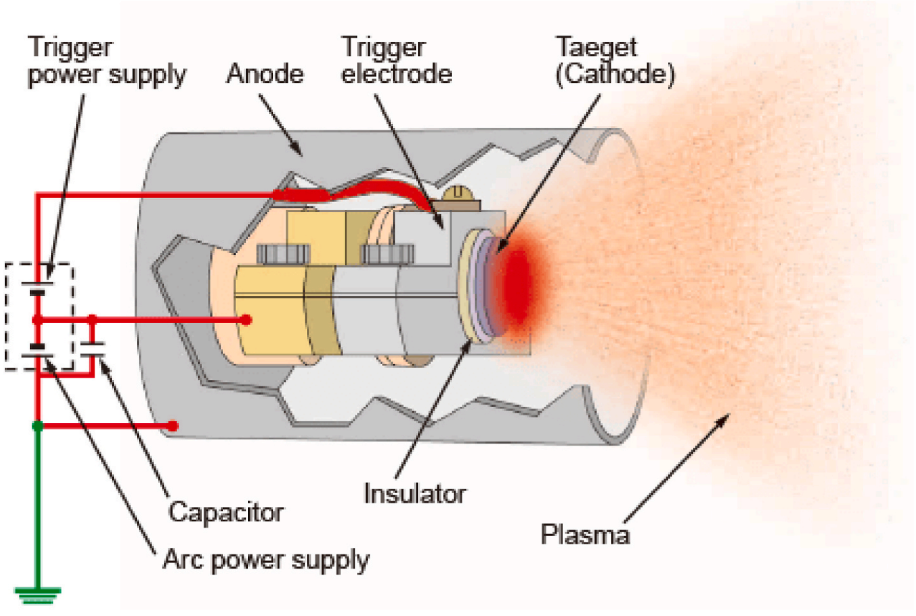


Fig. 17. The Arc Plasma Equipment [202].

plasma method can greatly enhance the kinetics of hydrogen absorption of Mg.

The core-shell structured Mg-TiO_2 nanocomposites via an arc plasma were synthesized [195]. The Mg-TiO_2 nanocomposite could absorb up to 5.5 wt.% H_2 in <5 min at 350 °C. The activation energy for hydrolysis dropped from 53.42 kJ mol^{-1} (for pure Mg) to 45.14 kJ mol^{-1} for Mg-TiO_2. Similarly, Pan and co-workers prepared Mg–TiO_2 composite powder by arc plasma evaporation of the Mg+5%TiO_2 mixture followed by passivation in air. Its entropy and hydrogenation enthalpy changes were −130.1 J/(K·mol) and −71.5 kJ/mol, respectively. Additionally, the activation energy for hydrogenation was 77.2 kJ/mol. These results demonstrate that the addition of TiO_2 to Mg, achieved through the arc plasma method, can act as a catalyst to enhance the kinetic properties of hydrogen sorption in Mg [195]. In another work, Mg-TM-La (TM = Ti, Fe, Ni) ternary composite powders were prepared via arc plasma evaporation using Mg-TM-La precursor mixture, followed by air passivation. They observed that the hydrogenation enthalpies of Mg were −68.7 kJ/mol H_2 for Mg–Ti–La powder, −72.9 kJ/mol H_2 for Mg–Fe–La powder, and −82.1 kJ/mol H_2 for Mg–Ni–La powder. Moreover, the Mg-Ni-La composite powder showed a 1.5 wt.% hydrogen absorption at 30 °C after 3.5 h, indicating a moderate absorption rate even at such a low temperature [195]. The study confirmed that the addition of 3*d* transition metals and 4*f* rare-earth metals to Mg through an arc plasma method can effectively enhance both the thermodynamic and kinetic properties of Mg nano powders for hydrogen storage.

The Mg–Y_2O_3 and Mg–Y nanocomposite powders were prepared through the arc plasma method, followed by in situ passivation. According to the PCT analyses, the Mg–Y_2O_3 powder has a greater capacity to store hydrogen than the Mg–Y powder. The hydrogenation enthalpies of the Mg–Y_2O_3 and Mg–Y powders are found to be −75.4 and 71.8 kJ/mol H_2, respectively, based on the van der Hoff equation. The hydrogenated Mg–Y_2O_3 powder exhibits a lower dehydriding temperature than the hydrogenated Mg–Y powder, as indicated by DTA tests. Y_2O_3 has a strong catalytic effect on magnesium hydrogen sorption, and this effect is more pronounced in the arc-evaporated Mg–Y_2O_3 composite powder [196].

The arc plasma method for preparing magnesium-based hydrogen storage materials consistently shows that this approach dramatically enhances both the thermodynamic and kinetic properties of Mg alloys. By forming core-shell nanostructures and incorporating transition metals, rare earth elements, or metal oxides/fluorides, the arc plasma method enables rapid hydrogen uptake at lower temperatures, reduces activation energies, and improves oxidation resistance compared to pure Mg. For example, Mg–Ni–La and Mg@Ni composites exhibit faster absorption rates and favourable enthalpies due to catalytic phase formation, while Mg–NiF_2, Mg–TiO_2, and Mg–CeO_2 nanocomposites show significantly improved hydrogen absorption capacities and lowered activation energies. The method's ability to create ultrafine, defect-rich, and catalytically active surfaces at scale makes it a promising strategy for advancing high-performance magnesium-based hydrogen storage materials.

5.4. Nanoscaffold confinement

Nanoscaffold confinement techniques involve restricting or encapsulating materials within a nanosized space. This technique significantly increases the surface area-to-volume ratio, creating specialized materials with enhanced properties, such as improved hydrogen storage, catalysis, or separation [48]. Encapsulating hydrogen-storing materials within a nanostructured scaffold can enhance their hydrogen diffusion and sorption kinetics, as well as improve their stability against environmental degradation [48,197]. Precise control over particle size and morphology in nanoconfined systems enables tailored hydrogen storage properties that are difficult to achieve with traditional alloying or doping [48]. It also prevents nanoparticle aggregation within the host material's pore structure [198].

Scaffold materials with diverse pore sizes, micropores, mesopores, and macropores, enable versatile applications and further enhance hydrogen storage by maintaining dispersion and preventing the growth or agglomeration of MgH_2 [167]. The surface chemistry of the scaffold also critically influences hydrogen storage performance. Hydrophilic surfaces enhance adsorption capacity through stronger hydrogen bonding interactions, while hydrophobic surfaces improve stability in humid environments but may reduce uptake efficiency. The balance between surface functionality and pore structure enables improved hydrogen storage capacity, faster kinetics, and greater cycling stability [199].

Various porous host materials have been explored to optimize MgH_2 nanoconfinement, including zeolites [200], covalent organic frameworks (COFs), metal organic frameworks (MOFs) [201], MXenes and carbon-based materials such as aerogels, nanotubes, and ordered mesoporous carbons [199]. MOFs show promise with high hydrogen storage capacities at low temperatures (up to 17.6 wt.% at −196 °C), although their room-temperature performance still requires improvement to meet DOE targets [199]. Zeolites face limitations due to heavier elemental composition and counterion effects, while COFs suffer from high costs and mechanical fragility [198]. Carbon-based materials stand out for their high surface area, tunable pore sizes, low weight, cost-effectiveness, and excellent chemical and thermal stability, making them the most widely used scaffolds for hydrogen storage applications.

The nanoconfinement of Mg/MgH_2 in scaffolds significantly improves hydrogen sorption kinetics. MgH_2 confined in carbon aerogel scaffolds exhibits dehydrogenation kinetics over five times faster than ball-milled MgH_2 due to the nanoconfinement effect, which maintains MgH_2 particles at the atomic scale, shortens hydrogen diffusion paths, and prevents particle agglomeration and sintering. The porous carbon framework also facilitates rapid hydrogen transport, improves heat dissipation, and may provide catalytic interfaces that weaken Mg–H bonds, further enhancing reaction rates. Compared to ball-milled MgH_2, which typically shows reduced hydrogen storage capacity (~5–6 wt.%) due to particle growth and incomplete hydrogenation, nanoconfined MgH_2 retains near-theoretical capacities (~6.5–7 wt.%) with improved cycling stability. Thus, carbon aerogel scaffolding both accelerates hydrogen sorption kinetics and preserves high storage capacity [48]. Additionally, the thermodynamic stability of MgH_2 is enhanced through nanoconfinement and the addition of catalysts. For instance, MgH_2@Ni-MOF composites exhibit improved thermodynamic properties, with desorption enthalpies of 69.7 ± 2.7 kJ mol^{-1} H_2 [201].

The Mg-based nanoscaffold materials achieve high hydrogen storage capacities. For instance, Chen et al. [203] fabricated V-decorated Mg nanoparticles confined in 1 nm carbon shells using a reactive gas evaporation method. They observed that over 94% loading of the $Mg_{92}V_8$@C nanocomposite exhibited a hydrogen storage capacity of 6.6 wt.% with improved kinetics. Moreover, the combination of nanoconfinement and catalytic effects leads to synergistic improvements in hydrogen storage properties. The addition of CNTs to the Mg-3Ni-2MnO_2 nanocomposite exhibits excellent thermal conductivity and good hydrogen storage capacity (more than 6% vol). The CNTs improve the mass and heat transfer properties of Mg-3Ni-2MnO_2, enhancing both the hydrogen storage capacity and kinetics [204]. Furthermore, core-shell architectures, such as graphene-supported MgH_2 with TiC_2 MXene coatings, achieve a synergistic effect, where the MXene shell provides catalytic Ti sites for H_2 dissociation. The structure provides geometric confinement, preventing nanoparticles from coalescing during cycling. Such designs yield stable capacity retention of 95% after 50 cycles, thanks to the mitigation of pulverization and oxidation [205].

Therefore, we can establish that the nanoconfinement of MgH_2 within porous scaffolds, such as MOFs, carbon aerogels, and graphene-based heterostructures, significantly enhances hydrogen storage properties by improving kinetics. For instance, five times faster dehydrogenation is observed in carbon aerogels. Moreover, nanoconfinement of

MgH_2 allows for tuneable thermodynamic properties (e.g., 69.7 kJ/mol H_2 desorption enthalpy in MgH_2@Ni-MOF) [48,201]. Carbon-based scaffolds, achieve 15-17 wt.% MgH_2 loading with 75% reversibility, while MOFs show promise with 17.6 wt.% H_2 capacity at −196 °C [199]. Innovations such as V-decorated Mg nanoparticles in carbon shells, showing 6.6 wt.% H_2 and layered heterostructures with ~2.5 nm MgH_2 show synergistic improvement in capacity and cyclability. However, challenges persist, including oxidation (MgO formation), thermal stability of nanoparticles, and scalability hurdles for complex synthesis. Table 7 shows a compares of nanoconfinement strategies for Mg-based hydrogen storage materials.

5.5. Severe plastic deformation

Severe plastic deformation (SPD) plays a pivotal role in enhancing the hydrogen storage capabilities of Mg-based alloys. The method refines the microstructures of the alloys, improving their hydrogenation and dehydrogenation kinetics, which are crucial for practical hydrogen storage applications [171,206]. SPD techniques such as high-pressure torsion (HPT), equal-channel angular pressing (ECAP), and cold rolling (CR) are employed to achieve ultrafine nanocrystalline structures, which facilitate faster hydrogenation and desorption due to increased surface area and defect density [147].

HPT is effective for processing Mg powder materials by inducing large shear strains. This which drastically refine grain sizes and introduce lattice distortions that destabilize Mg–H bonds, facilitating hydrogen release and uptake. Additionally, HPT enables the synthesis of novel Mg-based alloys and composites, including those with normally immiscible elements, by overcoming thermodynamic barriers through enhanced atomic mixing and defect generation [206,207].

The ECAP involves repeatedly pressing the material through an angled die, thereby imposing shear strain without altering the sample's cross-sectional dimensions. This results in grain refinement down to the nanoscale, as demonstrated in Mg alloys like ZK60. Such microstructural modification leads to significantly faster hydrogenation/dehydrogenation kinetics through enhanced diffusion and greater surface activity [208]. Notably, the processing temperature during ECAP influences the alloy's crystallographic texture, which modifies hydrogen sorption thermodynamics and kinetics by affecting lattice strain and hydrogen site occupancy.

Cold rolling (CR), a more conventional SPD technique, similarly refines grain structure and introduces favourable textures that improve hydride formation and decomposition kinetics in Mg alloys [171]. The degree of thickness reduction during CR correlates with the extent of defect generation and microstructural refinement, thereby controlling the enhancement in hydrogen sorption properties. Mg-Fe was synthesized via the extensive cold rolling (ECR) technique followed by the accumulative roll-bonding (ARB). They observed a synergistic effect of microstructural features and Fe as a catalyst, with its distribution improving activation, kinetics, and hydrogen capacity. They reported that ECR + ARB processing led to faster kinetics and larger capacities for both absorption and desorption due to the high concentration of defects, interstitial sites, and grain size reduction up to ~10 μm compared to pure Mg [209].

A combination of ECAP, CR, and HEBM techniques was used to enhance microstructural refinement and texture in AZ31 alloy. The AZ31 alloy demonstrated significant hydrogen absorption capabilities, achieving 6 wt.% H_2 at 350 °C and 15 bar [210]. The hydrogen storage capacity of cold-rolled Mg_2Ni alloy can attain up to 6.6 wt.% [211]. This was achieved after processing the alloy through multiple rolling and heat treatment cycles, showcasing the effectiveness of cold rolling in enhancing hydrogen storage [211]. The initial discharge capacity of a nanocrystalline Mg_2Ni alloy obtained was 205 mAh g^{-1}, which is comparable to the results obtained with ball-milled Mg_2Ni alloys.

The main characteristics of cold-rolled AZ91D alloy in comparison to pure magnesium is investigated. Both AZ91D and pure magnesium plates were subjected to 50 rolling passes in air, with each pass achieving a 50% thickness reduction by folding the plates in half between successive rolls [212]. To promote nucleation sites for the hydride phase, the rolled materials were then combined with 5 wt.% MgH_2 and ball milled for 30 min. Hydrogenation tests were conducted at 350 °C under a hydrogen pressure of 2 MPa for absorption and 0.01 MPa for desorption. Fig. 18 shows the optical micrographs of as-cast and cold rolled samples at different working temperatures and the hydrogenation and dehydrogenation kinetics of magnesium and cold-rolled AZ91D respectively. Compared to pure magnesium the AZ91D activate faster and exhibits faster dehydrogenation kinetics and a shorter incubation period.

Furthermore, the effect of the ECAP technique on Mg alloy (ZK60) was studied [207]. There was an increasing trend in the hydrogen desorption pressure with increasing processing temperature from 250 °C to 300 °C, demonstrating the impact of thermomechanical conditions on hydrogen release. From the reviewed literature, it can be established that lattice distortion and ultrafine grain structures generated by severe plastic deformation create numerous diffusion pathways and energetically favourable sites for hydrogen absorption and desorption. The combination of this enhanced defect density with tailored texture changes results in significant improvements in both the hydrogen storage kinetics and capacity of Mg-based alloys.

Table 7
Summary of the effect of nanoconfinement method on hydrogen storage properties of Mg-based hydrides and alloys.

System/scaffold	Kinetic Enhancement	Hydrogen Capacity	Key Observations
MgH_2@Carbon Aerogel	>5x faster kinetics	6.5-7 wt.%	Near-theoretical capacity, stable cycling
$Mg_{92}V_8$@C Nanocomposite	Improved sorption	6.6 wt.%	High loading (94%) with superior kinetics
MgH_2@Ni-MOF	Lowered desorption enthalpy	-	Enhanced cycling stability
Mg-3Ni-2MnO_2+CNTs	Improved mass/ heat transfer	>6 vol%	Enhanced thermal properties boost capacity & Kinetics
MgH_2 in Graphene-organosilica	Higher rehydrogenation	-	Particle size <2.5 nm, stable cycling
MgH_2 in carbon aerogel	5x faster Kinetics	15-17 wt.% loading	75% reversible, smaller pore sizes improve kinetics
MgH_2 @ TiC_2 MXene	-	-	Stable capacity retention of 95% after 50 cycles

5.6. Electrochemical reduction method

The electrochemical reduction method is a promising technique for synthesizing magnesium hydride, which is used in hydrogen storage applications. This process involves the electrochemical reduction of magnesium ions (Mg^{2+}) dissolved in an electrolyte solution, typically containing magnesium salts such as magnesium chloride ($MgCl_2$) or complex magnesium salts. In a typical setup, two electrodes, the working electrode (cathode) and the counter electrode (anode), are immersed in the electrolyte solution [213]. Hydrogen gas is supplied either by bubbling it directly into the electrolyte or passing it through the reaction chamber. When an electrical current is applied, magnesium ions at the working electrode gain electrons (i.e., are reduced) to form magnesium metal atoms on the electrode surface. Simultaneously, hydrogen molecules dissolved in the electrolyte or delivered to the electrode surface react with the freshly deposited magnesium metal, resulting in the direct formation of magnesium hydride (MgH_2) on the electrode.

Factors such as the applied current density, temperature, hydrogen pressure, and electrolyte composition govern the efficiency, purity, and

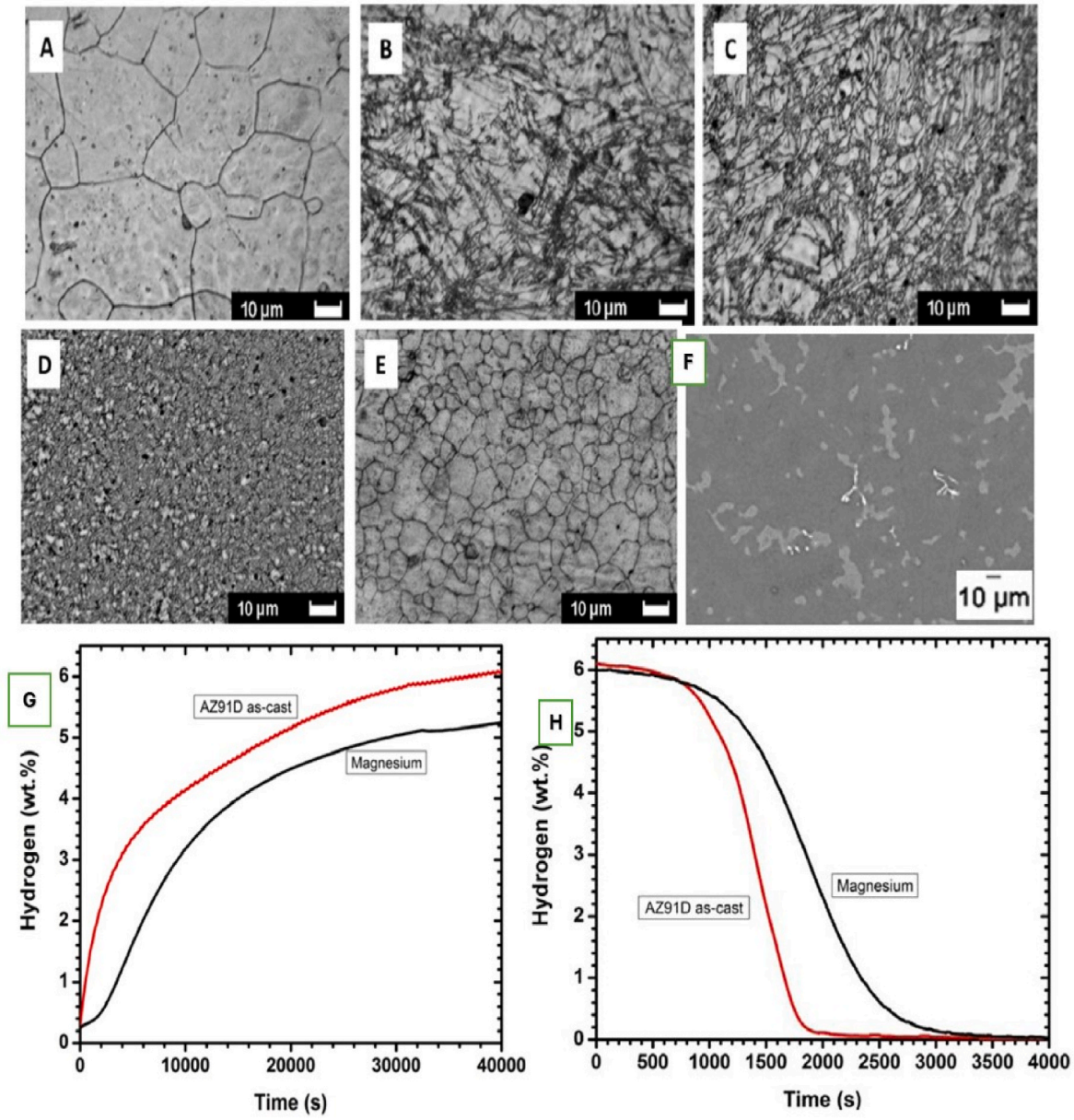


Fig. 18. Optical micrographs of AZ31 magnesium alloy. (A) as-cast; (B) two passes at 150 °C; (C) two passes at 200 °C; (D) two passes at 250 °C; (E) two passes at 300 °C; (F) microstructure of as-cast AZ91D. Primary α-Mg with discontinuous and divorced $Mg_{17}Al_{12}$ eutectic. The white particles are Al_8Mn_5 compound (γ-brass); (G) Hydrogenation and (H) Dehydrogenation kinetics of cold-rolled AZ91D and pure magnesium [212] (Reproduced with permission from Elsevier).

properties of the synthesized MgH_2, including particle size and crystallinity. This method enables the formation of MgH_2 under milder conditions compared to conventional high-temperature hydrogenation, offering potential for the controlled synthesis of nanostructured products that are beneficial for hydrogen storage performance. Recent studies have highlighted the critical role of molecular mediators with reduction potentials near −2.3 V vs. SHE in stabilizing intermediate hydride species during electrochemical synthesis. These mediators enable efficient interconversion between H_2 and hydride ions (H^-), which is essential for forming MgH_2 without introducing proton-related side reactions that complicate synthesis [214].

The electrochemical reduction method offers several advantages over traditional gas-phase hydrogenation. It can be performed at room temperature, eliminating the need for high temperature and high-pressure conditions [214]. This method also provides precise control over the hydriding process, enabling the synthesis of high-quality Mg-based hydrides with tailored properties. Additionally, the use of nonaqueous electrolytes avoids the challenges associated with aqueous electrolytes, such as hydrogen evolution and corrosion. Moreover, electrochemical reduction enables the precise tuning of particle size, morphology, and phase distribution, resulting in enhanced hydrogen absorption/desorption kinetics, as well as improved thermodynamics. For example, nanosized Mg produced electrochemically has demonstrated a significant fraction of γ-MgH_2 (~30%), reducing the apparent activation energy for hydrogen release from ~106 to ~69 kJ/mol and lowering the reaction enthalpy from ~75 to ~58 kJ/mol H_2, thereby facilitating hydrogen release at temperatures as low as 200 °C [102].

Despite its advantages, the electrochemical reduction method faces severe challenges. The high thermodynamic stability of MgH_2 requires high desorption temperatures, which limit its practical applications [84, 145]. The slow kinetics of hydrogen absorption are another significant challenge, which can be attributed to the large ionic radius of Mg and strong Mg–H bonding [215]. Furthermore, the limited cycle life of Mg-based hydrides due to oxidation and degradation during repeated

hydriding-dehydriding cycles remains a concern. However, alloying Mg with other metals such as Ni, Al, and Ti has been shown to improve the hydrogen storage properties of Mg-based hydrides. Moreover, nanostructuring and surface modification have emerged as an effective strategy to enhance the thermodynamic and kinetic properties of Mg-based hydrides [216].

The electrochemical conversion reaction of MgH_2 with Li ion enables the production of in-situ nanometric Mg and MgH_2 nanoparticles. The material exhibited remarkable hydrogen desorption at 200 °C under primary vacuum and hydrogen absorption at 100 °C under 10 bar H_2. The desorption temperature decreased from 416 °C to 295 °C, and the heat of formation decreased from −74 kJ mol^{-1} $(H_2)^{-1}$ to −56 kJ mol^{-1} $(H_2)^{-1}$, according to DSC measurements of MgH_2 [217]. Similarly, electrochemical hydriding of Mg-Ni and Mg-Ni-Mm alloys (11–24 wt.% Ni, 0–6 wt.% Mm) was achieved in 6 M KOH at temperatures ranging from 20 to 80 °C for 480 min. A maximum hydrogen concentration of 1.1% was achieved in the eutectic $MgNi_{24}Mm_5$ alloy at 80 °C, forming primarily MgH_2. Ni and Mm destabilized MgH_2, lowering its decomposition temperature by ~100 °C and enhancing de/hydriding kinetics. The hydrogen diffusion coefficient in $MgNi_{24}Mm_5$ at 20 °C was 4×10^{-10} cm^2/s, reflecting improved kinetics resulting from additive electronic/structural effects [218].

A novel strategy for mobile hydrogen storage uses rapidly solidified Mg-14Ni alloy ribbons synthesized via melt spinning, resulting in a refined microstructure that is ideal for enhanced hydrogen diffusion. Electrochemical hydriding at 90 °C for 120 min in alkaline electrolytes (e.g., KOH/NaOH) achieved 1.4 wt.% hydrogen uptake, with potential for higher capacity through optimized conditions (e.g., electrolyte composition, current density) [218].

6. Emerging computational frameworks for Mg-based hydride design

The experimental discovery and optimization of Mg-based hydrogen storage materials have traditionally proceeded were by trial-and-error. This approach is inadequate as the compositional space expands from binary MgH_2 derivatives to ternary alloys, nanocomposites, and now high-entropy alloys containing five or more principal elements. The combinatorial explosion of possible compositions, catalytic additives, and processing routes means that purely empirical screening is both time-prohibitive and cost-prohibitive at the scales required. Over the past two decades, three complementary computational methodologies namely including the CALPHAD (Calculation of Phase Diagrams) method, Density Functional Theory (DFT), and Machine Learning (ML), have emerged as indispensable tools for guiding material design with physical rigour and predictive power.

These three approaches are not interchangeable: they operate at fundamentally different length and time scales, and their power lies precisely in how they complement one another. DFT operates at the quantum-mechanical level, resolving electron density distributions and atomic-scale bond energetics with high accuracy but at high computational cost and for systems limited to hundreds of atoms. CALPHAD bridges the atomic scale and the engineering scale by parameterizing thermodynamic functions for individual phases, informed partly by DFT and partly by experimental data, and extrapolating them to multicomponent systems of arbitrary complexity, enabling full phase diagram prediction at the alloy design level. ML operates at the data level, learning the mapping between material descriptors and target properties from existing datasets and executing predictions at a speed that neither DFT nor CALPHAD can approach, enabling high-throughput screening of thousands of compositions. Used in isolation, each method has blind spots; integrated as a hierarchy such as DFT feeding CALPHAD databases, CALPHAD constraining ML feature spaces, ML guiding experimental iteration, constituting a powerful closed-loop design engine. The following subsections examine each method's capabilities, specific applications to Mg-based hydrides and Mg-containing HEAs, and the critical gaps that remain.

6.1. CALPHAD method

The CALPHAD method, first formalized by Kaufman and Bernstein in the 1970s and subsequently extended to metal-hydrogen systems, provides a systematic framework for predicting phase equilibria in multicomponent alloys by minimizing the total Gibbs free energy of the system as a function of composition, temperature, and pressure [219,220]. Each phase is described by a thermodynamic model, commonly a Redlich–Kister polynomial for solution phases or a sublattice model for ordered intermetallics with parameters fitted to experimental thermochemical data and to DFT-computed formation enthalpies and vibrational free energies. The central strength of CALPHAD is its extrapolation power*:* thermodynamic parameters determined from well-characterized binary and ternary subsystems can be combined to predict phase equilibria in quaternary, quinary, and higher-order systems where direct experimental measurement is impractical [100,220].

For Mg-specific systems, role of CALPHAD extends to predicting how processing routes alter the accessible phase space. Severe plastic deformation, for example, can kinetically trap metastable phases that lie outside the equilibrium phase diagram; CALPHAD can define the thermodynamic driving forces that govern whether these phases will form, persist, or revert during subsequent thermal treatment [171]. Similarly, nanostructuring shifts the effective free energy landscape through surface energy contributions that become significant below ~10 nm particle size—a size-dependent thermodynamic correction that can be incorporated into CALPHAD models to predict the stability of nanoconfined MgH_2 phases more accurately than bulk phase diagrams allow [221].

For Mg-based hydrogen storage materials, this extrapolation capability addresses a specific and critical design need. Phase stability directly controls hydrogen storage performance: the formation of catalytically active intermetallic phases such as Mg_2Ni or Mg_2Fe, the stability boundaries of metastable γ-MgH_2 relative to the equilibrium β-phase, and the solubility limits of alloying elements in the Mg lattice all determine whether a given composition will absorb and release hydrogen reversibly and at practical temperatures. CALPHAD can predict the temperature and composition windows within which these desirable phases are stable, guide the selection of alloying elements and their concentrations to stabilize target phases, and anticipate deleterious phase transformations such as the precipitation of inert MgO or irreversible intermetallic decomposition, which degrade cycling performance [100,221].

A compelling demonstration of CALPHAD-guided HEA design was provided by Floriano et al. [222], who used thermodynamic calculations to predict that both the equiatomic TiZrNbFeNi alloy and its non-equiatomic variant $Ti_{20}Zr_{20}Nb_5Fe_{40}Ni_{15}$ would adopt a single C14 Laves phase structure. This phase is known to favour reversible hydrogen absorption in AB_2-type intermetallics. Experimental XRD and Rietveld refinement confirmed the predicted phase with high fidelity, validating the CALPHAD model for this five-component system and demonstrating that phase-targeted HEA design is feasible without exhaustive experimental screening. The practical significance is substantial: the C14 Laves phase in TiZrNbFeNi can absorb approximately 1.8 H/f. u. at room temperature, and its thermodynamic stability predicted and then confirmed. This makes it a viable candidate for near-ambient hydrogen storage [222]. In a parallel study on refractory Mo-Nb-V-Ti HEAs, Bencze et al. [223] used CALPHAD calculations to predict single-phase BCC solid solution formation across a range of Ti concentrations, providing thermodynamic activities of Ti and V that were subsequently validated against Knudsen effusion mass spectrometry measurements. The agreement between computed and measured activities within experimental uncertainty establishes confidence that CALPHAD thermodynamic databases can be extended to refractory HEA systems relevant to high-temperature hydrogen storage [223].

Despite these advances, CALPHAD faces inherent limitations in the hydrogen storage context. Thermodynamic databases for hydrogen-containing multicomponent systems remain incomplete, particularly for the metal-hydrogen gas phase interactions at elevated pressures that govern PCT behaviour. The accuracy of predictions degrades when extrapolations are done beyond the composition range covered by the underlying binary data. Metastable phases, which are outside the equilibrium phase diagram, require separate kinetic modelling to predict their formation and persistence under real processing conditions. Bridging this gap between CALPHAD's equilibrium framework and the kinetically trapped, metastable microstructures that often deliver the best hydrogen storage performance remains an active area of research, with phase-field modelling and kinetic Monte Carlo simulations increasingly being coupled to CALPHAD databases to capture time-dependent phase evolution [221].

6.2. *Density functional theory: atomic-scale mechanistic insight*

Although CALPHAD operates at the phase level, DFT resolves the electronic structure that ultimately governs every thermodynamic and kinetic property of interest: Mg–H bond strength, hydrogen diffusion barriers, surface adsorption energetics, and the electronic perturbations induced by alloying elements [224]. By solving the Kohn–Sham equations self-consistently for a periodic supercell of atoms, DFT yields the ground-state electron density distribution and total energy, from which formation enthalpies, adsorption energies, transition state energies, and vibrational frequencies can be derived with chemical accuracy for systems of up to several hundred atoms. This atomic-scale resolution makes DFT uniquely suited to answering the mechanistic questions that CALPHAD cannot address: *why* does Nb_2O_5 catalyse MgH_2 dehydrogenation more effectively than Fe_3O_4? *Which* interstitial site does hydrogen preferentially occupy in a TiZrVMoNb HEA lattice? *How* does grain boundary segregation of a minority element alter local hydrogen diffusion kinetics?

In the context of MgH_2, DFT has established the foundational understanding of the Mg–H bond that motivates all modification strategies. Calculations of the electronic density of states confirm that the Mg–H interaction in β-MgH_2 is predominantly ionic in character, with the H 1s states hybridizing with Mg 3s/3p states to form a filled bonding band separated from an empty conduction band by a ~4 eV gap. This large electronic stability directly manifests as the ~74.5 kJ/mol H_2 formation enthalpy [224,225]. DFT-computed hydrogen diffusion barriers in bulk β-MgH_2 (~1.6 eV along the [001] direction, considerably lower than the ~2.0 eV barrier in the basal plane) rationalize why hydrogen release is highly anisotropic and why grain boundary engineering markedly improves kinetics [225] Shelyapina's comprehensive DFT review of hydrogen diffusion pathways in Mg identifies subsurface trapping as a critical kinetic bottleneck: hydrogen atoms that penetrate beyond the first subsurface layer experience a local energy minimum that delays bulk absorption, providing an atomistic explanation for the observation that surface-clean, freshly activated Mg absorbs hydrogen far faster than passivated or oxidized particles [45].

The role of alloying elements is mechanistically illuminated by DFT in ways that guide rational catalyst selection. Transition metal (TM) substitutions such as Ni, Ti, Pd and Fe modify the electronic environment around Mg atoms in two complementary ways: they weaken Mg–H bonding by introducing d-states that hybridize preferentially with H 1s orbitals and compete with Mg for hydrogen coordination, while simultaneously strengthening the overall surface binding of atomic H through TM–H bond formation that facilitates dissociative chemisorption of H_2 at the metal surface [122,226]. This dual effect (destabilizing bulk MgH_2 while activating the surface) provides the combination required for practical improvement: lower formation enthalpy reduces the thermodynamic desorption temperature, while stronger H_2 dissociation at the surface eliminates the kinetic barrier to absorption. DFT calculations for Mg decorated with transition metal clusters (Ni, Pd, Pt) consistently show formation enthalpy reductions of 10–20 kJ/mol H_2 relative to pure MgH_2, in quantitative agreement with experimental calorimetry where comparison is available [122].

DFT has moved from explaining known behaviour to predicting *a priori* which compositions will deliver desired properties. Halpren et al. [227] performed first-principles calculations on the TiZrVMoNb HEA, mapping the energetically preferred interstitial sites for hydrogen in both BCC (tetrahedral sites, energetically preferred) and FCC (octahedral sites) phases and predicting the likely BCC-to-FCC phase transformation pathway upon progressive hydrogenation, a structural transition that governs the two-stage PCT isotherm observed experimentally in many BCC HEAs. The predicted hydrogen storage capacity of ~2.5 H/M in the fully hydrogenated FCC dihydride phase was consistent with subsequent experimental measurements, lending confidence to DFT as a forward-predictive tool for HEA design. Hydrogen binding energies for monohydride and dihydride formation have also been computed across a library of BCC HEA compositions and validated against experimentally measured onset desorption temperatures [227]. Generally, the compositions with low DFT-calculated hydrogen binding energy exhibited low experimental desorption temperatures. Thus, DFT can serve as a quantitative pre-screening filter to prioritize candidate alloys before synthesis.

DFT calculations have limitations when used to investigate hydrogen storage behaviour. Standard DFT within the generalized gradient approximation (GGA) systematically underestimates band gaps and overestimates cohesive energies, leading to calculated Mg–H formation enthalpies that are typically 5–10 kJ/mol H_2 too large in magnitude relative to experiment. Temperature and pressure effects are absent from ground-state DFT unless phonon calculations are performed to add zero-point energy and vibrational free energy corrections. These corrections are computationally expensive addition that is often omitted, introducing errors in predicted equilibrium desorption temperatures of 20–40 °C. Perhaps most limiting is the system size constraint: DFT cannot routinely model the disordered, multi-element solid solutions that characterize real HEAs, where the relevant thermodynamic properties emerge from averaging over many atomic configurations. Special Quasi-random Structures (SQS) and the Coherent Potential Approximation (CPA) partially address this, but they remain approximations that may miss important local ordering effects. It is precisely these limitations that motivate the integration of DFT with CALPHAD (for macroscopic phase predictions) and with ML (for rapid sampling of chemical space at DFT accuracy).

Generally, DFT provides valuable insights into the microscopic processes of hydrogen absorption and desorption. This aids in the development of more efficient Mg-based materials for hydrogen storage. DFT studies have elucidated hydrogen interactions with Mg surfaces, including diffusion on Mg surface and into the bulk Mg. These insights are crucial for understanding and improving hydrogen absorption and desorption processes [45]. Alloying Mg with elements such as Ni, Ti, and Pd, and creating nanostructures, can enhance hydrogen storage properties by destabilizing metal-hydrogen bonds and improving kinetics. These modifications are supported by multiscale modelling and experimental synthesis [122].

Through DFT calculations, researchers can identify the effects of various alloying elements on the properties of Mg-based hydrides [226]. For instance, DFT has been used to explain how TM substitutions can weaken Mg–H bonding while simultaneously strengthening TM-H interactions. This dual effect can lead to improved hydrogen storage properties. Additionally, DFT facilitates the prediction of new metastable MgHx phases with enhanced hydrogen storage capabilities, which can be experimentally validated later. By simulating different alloy compositions and their interactions with hydrogen, DFT plays a critical role in the rational design of new materials that can overcome the limitations of pure magnesium in hydrogen storage applications [45].

Common Density Functional Theory (DFT) calculations in Mg-based hydrogen storage research encompass total energy and formation

energy computations, which are used to assess phase stability and thermodynamics of hydride formation. Also, adsorption energy calculations are used to determine favourable hydrogen binding sites on Mg surfaces. Diffusion barrier analyses are used to evaluate hydrogen mobility, crucial for sorption kinetics. Electronic structure and density of states analyses reveal bonding characteristics and explain how alloying elements such as Ni, Ti, and Pd modify Mg–H interactions, weakening Mg–H bonds while strengthening metal–hydrogen bonds to enhance hydrogen storage properties [225]. Transition state calculations identify activation energies for hydrogen diffusion and desorption, shedding light on rate-limiting steps, while surface and interface modelling elucidate catalytic effects and reaction pathways that improve hydrogen absorption and release [212]. Additionally, DFT predicts metastable MgH_x phases with potentially better storage capabilities, helps understand strain and defect influences on hydrogen behaviour, and models nanostructured systems to explore the impact of confinement and core-shell architectures [225]. These calculations inform the rational design of Mg-based hydrides by linking atomic-scale insights to enhanced thermodynamics and kinetics, thereby facilitating efficient hydrogen storage.

First-principle ab initio calculations based on DFT were carried out to investigate the hydrogen absorption behaviour in TiZrVMoNb HEA. The calculations predicted the preferred sites of the hydrogen atoms in the BCC and FCC phases of the HEA. They also predicted the possibility of a BCC-to-FCC phase transformation during hydrogenation as well as the hydrogen storage capacity of the HEA [228]. In another work, DFT simulations were used to compute the hydrogen binding energies for the formation of monohydrides and dihydrides in the BCC HEA structures. They validated the trends between the DFT-calculated hydrogen binding energies and the experimentally measured onset temperatures for hydrogen desorption [227].

6.3. Machine learning

Machine learning has entered hydrogen storage research as a response to a specific bottleneck: the experimental and DFT databases of Mg-based hydride properties are now large enough to train predictive models, yet the compositional space to be searched, spanning alloying elements, concentrations, processing conditions, and catalyst identities, is far too vast for exhaustive first-principles calculation. ML bridges this gap by learning structure-property relationships from existing data and applying them to predict the properties of untested compositions at comparately low computational cost, enabling high-throughput screening of thousands of candidates that would require years of DFT calculations or decades of experimental testing [229].

The architectures of ML models deployed in hydrogen storage research reflects the nature of the target properties. For thermodynamic quantities (hydride formation enthalpy, desorption temperature, equilibrium plateau pressure), graph neural networks (GNNs) have emerged as the leading architecture because they naturally encode the crystal structure as a graph of atomic nodes connected by bonds, allowing the model to learn how local coordination environments determine macroscopic energetics [230]. The MetalHydEnth model, a GNN trained on the AFLOW database of hydride formation enthalpies, achieves a mean absolute error of 5.5 kJ/mol H_2 for Mg-containing intermetallics [230], which is entirely adequate for ranking hundreds of candidate compositions by predicted thermodynamic suitability and filtering the most promising subset for higher-fidelity calculation. Batalović et al. [230] demonstrated this workflow explicitly, using a GNN to screen Mg-containing alloy compositions for hydrogen storage suitability and identifying $MgBe_{13}$ as a candidate for near-ambient storage conditions.

For kinetic properties, where the relevant information lies in atomic trajectories rather than ground-state configurations, ML interatomic potentials (MLIPs) offer a transformative capability. MLIPs are trained on DFT-computed energies and forces for a diverse set of atomic configurations and then applied in molecular dynamics (MD) simulations that would be computationally prohibitive at the DFT level. Morrison et al. [231] developed a MLIP for the MgH_2 system and applied it to microsecond-scale MD simulations, which is four orders of magnitude longer than achievable with DFT-MD. Revealing the formation and trapping of subsurface molecular H_2 as a previously unrecognized kinetic bottleneck in dehydrogenation. This subsurface H_2 trapping mechanism, invisible to short-timescale DFT-MD and inaccessible to macroscopic kinetic models, provides a concrete atomic-scale target for catalytic intervention: surface modifications that destabilize subsurface H_2 trapping sites should yield disproportionate kinetic improvements. This is the type of mechanistic insight that only the combination of DFT accuracy and ML computational speed can deliver.

For HEA design specifically, where the composition space is effectively infinite, Bayesian optimization combined with ML property prediction has been applied to efficiently navigate the search for optimal hydrogen binding energies. Halpren et al. [227] used Bayesian optimization to explore the BCC HEA composition space, identifying promising candidates with target hydrogen binding energies within a fraction of the computational effort required for exhaustive search. Critically, the interpretable ML models in this study revealed physically meaningful structure-property relationships: the thermodynamics of monohydride formation (first absorption stage) are primarily governed by the bulk modulus of the alloy while dihydride formation (second stage) is controlled by the electronic density of states at the d-band, reflecting the availability of transition metal states to hybridize with H 1s orbitals [227]. These insights directly inform compositional design rules: alloys with intermediate bulk modulus and high d-band density of states near the Fermi level should be targeted for compositions that balance monohydride thermodynamic accessibility with dihydride stability.

Physics-informed machine learning (PIML) represents the next generation of ML deployment in this field, addressing the core weakness of data-driven models; their tendency to extrapolate unphysically beyond the training distribution. By embedding thermodynamic constraints (e.g., Hess's law relationships between formation enthalpies, van't Hoff equation relating ΔH and ΔS to equilibrium pressure, conservation of mass during phase transformation) directly into the loss function or model architecture, PIML models are constrained to produce physically consistent predictions even in regions of compositional space where training data are sparse [232]. The integration of CALPHAD-derived thermodynamic relationships as hard constraints within ML models using CALPHAD as a physics engine that regularizes ML predictions. This represents a particularly promising direction, combining the extrapolation accuracy of CALPHAD with the compositional flexibility and speed of ML [233].

The field faces important unresolved challenges. Training data for Mg-based hydrides remain limited in several critical dimensions: experimental datasets rarely report consistent, standardized conditions (pressure, temperature, particle size, activation protocol), making cross-study compilation noisy; DFT datasets are biased towards stable crystalline phases and underrepresent the disordered, defect-rich, and nanostructured forms that often deliver the best experimental performance; and cycling stability data are almost entirely absent from existing ML training sets. Addressing these gaps requires coordinated community efforts: standardized reporting protocols for experimental hydrogen storage measurements, curated open-access databases that integrate DFT, CALPHAD, and experimental data under consistent metadata standards, and active learning workflows that direct new experiments toward the most informative regions of composition space [227].

6.4. Integrated computational frameworks: emerging works, convergent trends, and future directions

The preceding subsections have treated CALPHAD, DFT, and ML as distinct tools. In practice, the most consequential recent advances in Mg-based and HEA hydrogen storage design have come not from any single

method in isolation, but from their deliberate integration into multi-fidelity workflows, where the strengths of each approach compensate for the limitations of the others. This section surveys the most significant recent works embodying this integrated paradigm, identifies the trends they collectively establish, and outlines the research directions they point toward.

6.4.1. From screening to synthesis: the ML–DFT–experiment loop

The first major class of integrated frameworks couples ML-driven high-throughput screening with DFT validation and targeted experimental synthesis in a closed loop. The foundational demonstration for HEA hydrides was provided by Witman et al. [234], who trained a Gaussian Process Regression (GPR) model on the U.S. DOE HydPARK metal hydride database to predict hydride formation enthalpies across a library of 672 equimolar HEA compositions, without requiring knowledge of crystal structures. The trained model screened the composition space orders of magnitude faster than DFT, identifying candidates predicted to exhibit large destabilisation of the hydride phase. Targeted synthesis and PCT measurement of three predicted compositions; TiVZrNbHf, AlTiVNbTa, and AlTiVCr confirmed the predicted trends. AlTiVCr showed a 70-fold increase in equilibrium plateau pressure and a 20 kJ/mol H_2 reduction in desorption enthalpy relative to the benchmark TiVZrNbHfH_x [234]. This work established several features that have since become benchmarks for the field: (i) composition-only descriptors (no structural input) are sufficient for predicting thermodynamic trends in HEAs, (ii) ML-derived design rules can directly guide synthesis priorities without exhaustive first-principles calculation at the screening stage, and (iii) experimental validation is an indispensable final step that feeds improved data back into the model, enabling iterative refinement. The mean absolute error of the improved GPR model for ΔH prediction was 1.4 kJ/mol H_2 across the training set. This is accuracy is sufficient for thermodynamic ranking within a large candidate pool.

The same group subsequently extended this framework in a multi-objective direction. Witman et al. [235] applied Pareto-front optimization to simultaneously target desorption enthalpy below 60 kJ/mol H_2 and hydrogen capacity approaching 2 H/M across a much larger HEA composition space, demonstrating that multiple competing objectives can be navigated efficiently using ML-guided iterative synthesis without exhaustive experimental sampling [235].

Multi-objective Bayesian optimization (BO) with DFT calculations on BCC HEAs was used to simultaneously target monohydride and dihydride thermodynamics in a V-Nb-Cr-Mo-Mn composition space [227]. Bayesian optimization was chosen over passive ML screening due to the inherent adaptive nature. Each DFT calculation updates the uncertainty of the surrogate model, resulting in subsequent calculations being more informative and targeted, rather than randomly selected compositions. This allows for efficient navigation of a high-dimensional search space with a minimal number of expensive DFT evaluations. The BO-DFT workflow identified eight new HEA candidates, including VNbCrMoMn, which was predicted and experimentally confirmed to store 2.83 wt.% H_2 at room temperature and atmospheric pressure, exceeding the capacity of commercial $LaNi_5H_6$ (1.38 wt.%) and $TiFeH_2$ (1.91 wt.%) under the same conditions [227]. The interpretable ML component of the study, using SHAP (SHapley Additive exPlanations) values to decompose model predictions revealed that monohydride formation thermodynamics are controlled primarily by the alloy bulk modulus while dihydride formation is governed by the d-band density of states. These physically interpretable descriptors provide transferable design rules. Future alloy screening can prioritize compositions with intermediate bulk modulus (for accessible monohydride) and high d-band occupancy (for stable but not over-stabilized dihydride).

6.4.2. DFT-parameterized CALPHAD for quantitative PCT prediction

A second major integration trend moves beyond qualitative phase diagram prediction toward quantitative, first-principles-grounded PCT simulation. The historical limitation of CALPHAD in this context has been its dependence on experimental PCT data to fit thermodynamic model parameters. Hannappel et al. [236] addressed this directly by developing a Python-based PCT Simulation Toolkit that automates the full workflow from crystal structure input to quantitative PCT curve prediction. The toolkit automatically identifies interstitial void sites in the metallic lattice, generates VASP input files for DFT formation enthalpy calculations at each hydrogen occupancy, and constructs a para-equilibrium thermodynamic model from the DFT outputs. Validated across five hydride classes including BCC and FCC metals, AB_5 ($LaNi_5$), AB_2 ($TiMn_2$), and AB (FeTi). The framework achieved hydrogen capacity predictions within 95% mean accuracy and sorption pressures within one order of magnitude of experimental values using only the PBE functional without vibrational corrections. The significance is methodological: for the first time, PCT curves for previously unsynthesized compositions can be predicted purely from structural input, prior to any laboratory work. The toolkit is open-source, lowering the barrier to adoption, and the authors explicitly identify high-pressure PCT regimes (>1 GPa) and hydrogen-induced structural transformations (BCC-to-FCC transitions) as the next modelling targets, providing a clear roadmap for capability extension [236].

AlMatrouk et al. [237] directly combined DFT and CALPHAD calculations to predict the pressure-temperature phase diagram for MgH_2 formation and decomposition, finding good agreement with experimental van't Hoff data and establishing DFT-derived formation enthalpies as reliable inputs for Mg–H CALPHAD database construction when experimental data are absent [237]. The comprehensive CALPHAD methodology review by Palumbo et al. [238] systematically mapped where DFT inputs have been used to fill database gaps in metal-hydrogen systems, particularly for end-member energies of complex intermetallic phases and for metastable hydride intermediates. They also identified the representation of hydrogen-induced lattice expansion and para-equilibrium kinetics in multicomponent systems as the outstanding unsolved modelling challenges [238].

6.4.3. Machine learning interatomic potentials: bridging DFT accuracy and MD Timescales

A third critical integration is the use of ML interatomic potentials (MLIPs) to achieve DFT-level accuracy in molecular dynamics simulations at timescales four to six orders of magnitude longer than typical ab initio MD will allow. A trained Behler–Parrinello neural network potential (BPNNP) on a DFT database of Mg–H configurations and on a nanosecond-scale MD simulations of MgH_2 surface dehydrogenation [239], shows a unique mechanism. Thus, the formation and subsurface trapping of molecular H_2 in the near-surface layer of MgH_2, where individual H_2 molecules formed in the subsurface can remain trapped for more than 60 ps before escaping, with some molecules temporarily dissociating and reforming before eventual desorption. Across eight H_2 desorption events observed within a 1 ns simulation at 800 K, all originated in the subsurface layer, suggesting that this subsurface trapping is not an occasional anomaly but a systematic kinetic bottleneck during dehydrogenation. The mechanistic implication is direct: catalysts or surface modifications that disrupt subsurface trapping sites should yield greater kinetic improvements than those that only accelerate surface H_2 dissociation/recombination. These findings redirect catalyst design priorities in a way that purely macroscopic kinetic measurements could not have identified [239].

This class of MLIP-enabled mechanistic discovery is rapidly expanding. The HYPHAD project has adopted universal MLIPs in conjunction with CALPHAD and large-scale experimental synthesis specifically to screen $TiMn_2$- and FeTi-based metal hydrides for replacement of costly Zr and V. This allows MLIP-based multi-scale discovery as an industrial-facing design methodology rather than a purely academic exercise [240]. The transition of MLIP frameworks from proof-of-concept studies to program-level deployment signals a maturation of this integration approach.

6.4.4. Graph neural networks and phase diagram prediction for disordered systems

A fourth emerging integration addresses one of the most fundamental limitations of both DFT and CALPHAD for HEA hydrides: neither method handles the configurational disorder of multi-principal element alloys with sufficient rigor for predicting phase diagrams. To overcome the short-range ordering effects that are averaged out in conventional CALPHAD treatment of solution phases, Witman et al. extended their earlier ML work by developing on-lattice graph neural networks (GNNs) that predict phase diagrams of disordered alloys and their hydrides from limited training data, capturing the dependence of thermodynamic properties on local compositional environments [241]. The GNN approach inherits two key advantages over composition-only ML models: it explicitly encodes the local atomic connectivity that governs hydrogen binding site energetics in HEAs, and it can be trained on relatively small DFT datasets (tens to hundreds of configurations) while still generalizing to predict properties across large compositional spaces. This positions on-lattice GNNs as a bridge between the quantum-mechanical accuracy of DFT (which is too slow for exhaustive coverage) and the compositional breadth of CALPHAD (which lacks atomic-scale resolution), filling a capability gap that neither method alone can address.

The Forward-Inverse Navigation and Discovery (FIND) platform [242,243] could be integrated in coupling forward prediction (composition → hydrogen storage properties) with inverse design (target properties → optimal composition) within a single ML framework incorporating variational autoencoders [242]. Using Magpie-generated compositional features and multi-objective regression, FIND simultaneously predicts absorption/desorption plateau pressures, enthalpy change, entropy change, and maximum capacity, and then uses the inverse design module to propose compositions that achieve user-specified combinations of these properties. This forward–inverse design approach represents the most direct expression of autonomous materials discovery yet demonstrated for solid-state hydrogen storage and provides a template applicable to Mg-based HEA composition optimization [242].

7. Trends and future research directions

Synthesizing across these representative works, some convergent trends defining the current trajectory of integrated computational design for Mg-based hydrogen storage are as follows:

The hierarchy is shifting from sequential to simultaneous multi-fidelity. Early integrated workflows were sequential; ML screens, then DFT validates, then CALPHAD maps phase stability. Emerging approaches perform these concurrently, with active learning updating ML models in real time as DFT and experimental data arrive, and CALPHAD constraints embedded in ML loss functions rather than applied as post hoc filters [234,235,237]. The practical consequence is faster convergence: fewer experimental syntheses are needed to identify optimal compositions.

The PCT diagrams are becoming first-principles predictable. The Hannappel et al. framework [236] demonstrates that quantitative PCT curves; the primary experimental characterization of hydrogen storage materials, can now be predicted from DFT structural inputs alone with sufficient accuracy for preliminary screening. As DFT database size grows and MLIP accuracy improves, the prediction accuracy of plateau pressure and capacity will approach the level of useful engineering input rather than qualitative guidance.

Universal MLIPs are reducing the specialization barrier. The development of universal MLIPs (e.g., MACE-MP, CHGNet, SevenNet) trained on the Materials Project database is making it possible to run reasonably accurate MLIP-MD simulations of new HEAs compositions without training a system-specific potential from scratch. This dramatically lowers the computational cost and expertise required to explore kinetics in new alloy systems, enabling the kind of rapid, broad-spectrum screening that was previously limited to thermodynamic properties [239,240,242].

Interpretable and explainable ML are generating transferable design rules. The shift from black-box neural networks toward interpretable models (decision trees, SHAP-augmented gradient boosting, physics-informed neural networks) is extracting physically meaningful descriptors such as bulk modulus, d-band center, Voronoi interstitial volume, average electronegativity difference. This links composition to hydrogen storage properties through understood physical mechanisms [240,244]. These descriptors are transferable across alloy families, meaning design rules learned from BCC HEAs can inform Mg–HEA composition optimization without retraining from scratch.

The need for shared infrastructure is paramount. A recurring limitation identified across all major review works [238,242,244] is the fragmented and inconsistent nature of training data: experimental datasets use different measurement conditions, DFT datasets have different functional and convergence settings, and there is no standardized metadata schema for hydrogen storage measurements. The development of community databases, analogous to the Cambridge Structural Database for crystal structures or the HydPARK dataset that multiple ML studies have already built upon with consistent data provenance and standardized PCT measurement protocols is identified as the single highest-leverage community investment for the next five years.

For Mg-based HEAs and Mg-containing complex alloys, the integrated computational design agenda should focus on critical research priorities such as (i) building targeted DFT datasets for Mg-TM-RE (transition metal–rare earth) multicomponent systems that are large enough to train system-specific or fine-tuned universal MLIPs, enabling nanosecond-scale kinetic simulations of realistic Mg–HEA compositions, (ii) developing CALPHAD databases that explicitly parameterize Mg–H interactions in the presence of TM and RE solutes, currently the most significant gap in phase diagram prediction for this material class, and (iii) demonstrating closed-loop autonomous synthesis where ML-predicted compositions are synthesized, characterized, and fed back into the model without human intervention in the composition selection step for at least one Mg–HEA system, establishing the viability of this paradigm for the broader Mg-based hydrogen storage community.

On the experimental and compositional side, three specific research directions follow directly from the evidence gaps identified in this review. First, compositional design of Mg-containing HEAs should move beyond equiatomic compositions toward non-equiatomic variants in which Mg content is systematically varied between 10 and 40 at.% while maintaining a BCC single-phase structure. This is thermodynamically favourable for simultaneously achieving ΔH values of -40 to -55 kJ/mol H_2 and gravimetric capacities above 2 wt.%. The theoretical basis for predicting the BCC phase boundary as a function of Mg content in TM-rich HEAs is now available through DFT-parameterized CALPHAD, making targeted experimental exploration of this compositional window feasible without exhaustive trial-and-error synthesis. Second, advanced operando characterization such as in-situ synchrotron XRD coupled with simultaneous PCT measurement should be systematically applied to the highest-performing composite and HEA systems to resolve the rate-limiting step under realistic cycling conditions rather than idealized single-cycle laboratory protocols. The distinction between surface-limited, diffusion-limited, and nucleation-limited regimes has direct implications for catalyst design priorities and is currently inferred indirectly from macroscopic kinetic models rather than observed directly. Third, the cycling stability gap identified across all modification strategies should be addressed through standardized accelerated cycling protocols. A community-agreed minimum reporting standard of a minimum of 500 cycles with capacity measurement every 50 cycles and post-cycling microstructural characterization should be implemented. Without this baseline, cross-study comparison of cycling durability remains impossible and the field cannot identify which degradation mechanisms are intrinsic to each material class versus artefacts of specific synthesis or testing conditions.

8. Conclusion

This review has examined the current state of Mg-based hydrides and CCAs, with special interest in Mg-containing HEAs for solid-state hydrogen storage, surveying fundamental thermodynamics and kinetics, complex hydride systems, alloying and nanostructuring strategies, processing methods, and the computational frameworks that are reshaping materials design. Many of the physical and chemical barriers that have historically constrained MgH_2 from practical deployment are now understood at the atomic level, and the tools required to engineer around them; from ML-guided composition screening to MLIP-enabled nanosecond-scale kinetics modelling.

The thermodynamic landscape of pure MgH_2, characterized by a desorption enthalpy of 74.5 ± 1 kJ/mol H_2 and equilibrium desorption temperature near 287 °C, sets the baseline against which all modification strategies must be measured. The most consequential reductions in thermodynamic stability have been achieved through three routes, each of which has been substantially clarified by this review's revised treatment of Section 4. First, ternary complex hydrides such as Mg_2NiH_4 ($\Delta H \approx 64$ kJ/mol H_2) exploit the formation of complex anions ($[NiH_4]^{4-}$) that electronically destabilize the Mg–H bond, though at the cost of reduced gravimetric capacity (~3.6 wt.%). Second, reactive hydride composites (RHC), most notably the MgH_2–$LiBH_4$ system introduced by Vajo et al. [30] achieve a ~25 kJ/mol H_2 reduction in ΔH through thermodynamic coupling. One of the most practically significant results in the field is the MgB_2 formation, enabling a reversible storage up to 8–10 wt.% H_2 at 315–400 °C. Third, Mg-containing HEAs occupy an intermediate thermodynamic regime ($\Delta H = -35$ to -59 kJ/mol H_2), where multi-principal-element solid-solution disorder distributes hydrogen binding energies across a heterogeneous landscape of interstitial sites, producing sloped PCT plateaus that are thermodynamically accessible at lower temperatures than pure MgH_2.

Kinetically, the Section 4.3 established that the three primary barriers to MgH_2 dehydrogenation: surface oxide passivation, Mg–H bond scission, and bulk hydrogen diffusion, respond differently to catalytic and microstructural interventions. Nb_2O_5 and Fe_3O_4 remain among the most effective oxide catalysts for surface activation, while nanostructuring to grain sizes below 20 nm reduces the apparent activation energy from ~162 to ~94 kJ/mol H_2 by shortening diffusion pathways and increasing the density of reactive grain boundary sites. Importantly, however, the MLIP-enabled molecular dynamics study by Morrison et al. [231] identified subsurface H_2 trapping as a previously unrecognized kinetic bottleneck that macroscopic measurements cannot resolve. This redirects catalyst design priorities toward disruption of near-surface trapping sites rather than further optimization of surface dissociation catalysts.

The complex hydrides reviewed in Section 4: Mg_2NiH_4, Mg_2FeH_6, and RHC borohydride composites collectively demonstrate that the 74.5 kJ/mol H_2 thermodynamic floor of MgH_2 is not inviolable. Mg_2FeH_6, with its volumetric density of 150 kg H_2/m^3 and gravimetric capacity of ~5.5 wt.%, remains unmatched for volumetric applications despite its high T_des (>400 °C); partial substitution of Fe by Ni and combination with $LiBH_4$ represent the most credible near-term destabilisation pathways. The RHC framework demonstrates that thermodynamic coupling through co-product formation is a general design principle extendable beyond MgH_2–$LiBH_4$ to MgH_2–$Mg(BH_4)_2$ and MgH_2–$Ca(BH_4)_2$ systems, with MgB_2 formation confirmed as the universal thermodynamic anchor across all Mg–borohydride RHC systems [245].

The computational sections of this review reflect a field transitioning from single-method calculation toward integrated multi-fidelity workflows. CALPHAD has matured to the point where DFT-derived formation enthalpies can substitute for experimental input in Mg–H database construction, and the open-source PCT Simulation Toolkit of Hannappel et al. [236] now enables quantitative PCT curve prediction without any experimental fitting for previously unsynthesized compositions. DFT has clarified the anisotropic nature of hydrogen diffusion in MgH_2 (activation energy ~1.6 eV along [001] vs. ~2.0 eV in the basal plane) and the dual role of transition metal substitution in simultaneously weakening Mg–H bonds and modifying surface binding energetics. ML, and in particular GNNs and Bayesian optimization frameworks, has demonstrated that composition-only descriptors are sufficient for reliable thermodynamic ranking across hundreds of candidate HEA compositions, with the HydPARK-trained model of Witman et al. [234] achieving MAE = 1.4 kJ/mol H_2 and the Bayesian–DFT framework of Halpren et al. [227] identifying VNbCrMoMn as storing 2.83 wt.% H_2 at room temperature. The interpretable ML analysis of the latter study established bulk modulus and d-band density of states as transferable design descriptors applicable across BCC HEA families.

Five convergent trends: the shift from sequential to concurrent multi-fidelity workflows, the first-principles predictability of PCT diagrams, the democratizing effect of universal MLIPs, the generation of transferable design rules by interpretable ML, and the emergence of shared data infrastructure as the rate-limiting resource, collectively define the direction of the field over the coming decade. For Mg–HEAs specifically, three near-term priorities follow directly from this review: building DFT datasets for Mg–TM–RE systems of sufficient size to train system-specific or fine-tuned universal MLIPs; developing CALPHAD databases that parameterize Mg–H interactions in the presence of TM and RE solutes; and demonstrating at least one closed-loop autonomous synthesis cycle for a Mg–HEA composition. Realizing these priorities will require deliberate coordination between the synthesis, characterization, and computation communities, including adoption of standardized PCT measurement protocols and open-access data deposition practices that have so far been inconsistent across the literature.

In conclusion, this review establishes that Mg-based hydrides and their high-entropy alloy derivatives constitute one of the most scientifically rich and practically consequential material classes in the hydrogen storage landscape. The combination of magnesium's unmatched abundance and gravimetric capacity with the compositional flexibility of HEA design and the predictive power of modern computational tools creates a uniquely favourable convergence of opportunity. The remaining challenges such as thermodynamic high-stability of MgH_2, sluggish bulk diffusion kinetics, and incomplete computational databases for multicomponent Mg systems are well-defined and tractable. With continued integration of experimental and computational effort, and with the infrastructure investments identified here, Mg-based hydrogen storage materials are well positioned to contribute meaningfully to the energy transition.

Funding

This work was funded by the International Science Partnerships Fund (ISPF) from the Royal Society. Ref (ICAO\R1\241164- ISPF - International Collaboration Awards 2024.

CRediT authorship contribution statement

Joseph Dela Aziafor: Writing – review & editing, Writing – original draft, Methodology, Investigation, Formal analysis, Data curation, Conceptualization. **Bongani Ramatsoma:** Writing – review & editing, Writing – original draft, Methodology, Formal analysis, Data curation, Conceptualization. **Nihad Omer Hassan:** Writing – review & editing, Supervision, Funding acquisition, Formal analysis, Conceptualization. **Abdalrhaman Koko:** Writing – review & editing, Visualization, Supervision, Project administration, Funding acquisition, Formal analysis, Conceptualization. **Michael Bodunrin:** Writing – review & editing, Supervision, Resources, Project administration, Funding acquisition, Formal analysis, Conceptualization. **Desmond Klenam:** Writing – review & editing, Writing – original draft, Supervision, Resources, Project administration, Funding acquisition, Formal analysis, Conceptualization.

Declaration of competing interest

The authors declare that they have no known competing financial interests or personal relationships that could have appeared to influence the work reported in this paper.

References

[1] Q. Hassan, P. Viktor, J. Al-Musawi T, B. Mahmood Ali, S. Algburi, H.M. Alzoubi, et al., The renewable energy role in the global energy transformations, Renew. Energy Focus 48 (2024) 100545, https://doi.org/10.1016/J.REF.2024.100545.

[2] X.F.M. O'g'li, Renewable energy sources: advancements, challenges, and prospects, Int. J. Adv. Sci. Res. 3 (2023) 14–25, https://doi.org/10.37547/IJASR-03-08-04.

[3] S.A. Hussain, F. Razi, K. Hewage, R. Sadiq, The perspective of energy poverty and 1st energy crisis of green transition, Energy 275 (2023) 127487, https://doi.org/10.1016/J.ENERGY.2023.127487.

[4] H. Qudrat-Ullah, Myth: renewable energy is too intermittent to be reliable?, 17–47, https://doi.org/10.1007/978-3-031-59733-6_2, 2024.

[5] I. Rolo, V.A.F. Costa, F.P. Brito, Hydrogen-based energy systems: current technology development status, opportunities and challenges, Energies 17 (2024) 180, https://doi.org/10.3390/EN17010180, 2023;17:180.

[6] H. Ishaq, I. Dincer, C. Crawford, A review on hydrogen production and utilization: challenges and opportunities, Int. J. Hydrogen Energy 47 (2022) 26238–26264, https://doi.org/10.1016/J.IJHYDENE.2021.11.149.

[7] D. Zhao, X. Wang, L. Yue, Y. He, B. Chen, Porous metal–organic frameworks for hydrogen storage, Chem. Commun. 58 (2022) 11059–11078, https://doi.org/10.1039/D2CC04036K.

[8] Y. Xu, Y. Zhou, Y. Li, Z. Ding, Research progress and application prospects of solid-state hydrogen storage technology, Molecules 29 (2024) 1767, https://doi.org/10.3390/MOLECULES29081767, 2024;29:1767.

[9] M.M. Rampai, C.B. Mtshali, N.S. Seroka, L. Khotseng, Hydrogen production, storage, and transportation: recent advances, RSC Adv. 14 (2024) 6699–6718, https://doi.org/10.1039/D3RA08305E.

[10] A. Salehabadi, M.F. Umar, A. Ahmad, M.I. Ahmad, N. Ismail, M. Rafatullah, Carbon-based nanocomposites in solid-state hydrogen storage technology: an overview, Int. J. Energy Res. 44 (2020) 11044–11058, https://doi.org/10.1002/ER.5674;JOURNAL:JOURNAL:1099114X;WGROUP:STRING:PUBLICATION.

[11] R.B. Biniwale, S. Rayalu, S. Devotta, M. Ichikawa, Chemical hydrides: a solution to high capacity hydrogen storage and supply, Int. J. Hydrogen Energy 33 (2008) 360–365, https://doi.org/10.1016/J.IJHYDENE.2007.07.028.

[12] Q. Liu, W. Ran, W. Bao, Y. Li, A review on catalytic hydrolysis of ammonia borane for hydrogen production, Energies (Basel) 18 (2025) 1105, https://doi.org/10.3390/EN18051105/S1.

[13] D. Openshaw, W.T. Lang, L. Goldstone, J. Wildsmith, B. Freeman, G. Bagnato, Hydrogen storage methods by lithium borohydride, Int. J. Hydrogen Energy 69 (2024) 1188–1198, https://doi.org/10.1016/J.IJHYDENE.2024.05.109.

[14] J. Mao, Z. Guo, X. Yu, H. Liu, Improved hydrogen storage properties of NaBH4 destabilized by CaH2 and Ca(BH4)2, J. Phys. Chem. C 115 (2011) 9283–9290, https://doi.org/10.1021/JP2020319.

[15] N.S. Mustafa, N.A.M. Noor, N.A.M.Y. Omar, Z. Omar, M. Ismail, Influence of CeCl3 incorporation on the dehydrogenation characteristics of NaAlH4 for solid-state hydrogen storage, Int. J. Hydrogen Energy 105 (2025) 278–285, https://doi.org/10.1016/J.IJHYDENE.2025.01.197.

[16] M. Kumar, T. Das, Study on the catalytic thermal decomposition of metal-hydride (NaH) to enhance the hydrogen desorption characteristics, Int. J. Hydrogen Energy 50 (2024) 367–378, https://doi.org/10.1016/J.IJHYDENE.2023.07.110.

[17] G.K. Sujan, Z. Pan, H. Li, D. Liang, N. Alam, An overview on TiFe intermetallic for solid-state hydrogen storage: microstructure, hydrogenation and fabrication processes, Crit. Rev. Solid State Mater. Sci. 45 (2020) 410–427, https://doi.org/10.1080/10408436.2019.1652143. SUBPAGE:STRING:FULL.

[18] A. Altuntepe, S. Erkan, M.A. Olgar, S. Çelik, R. Zan, Investigating surface area and hydrogen pressure effects on LiH and NaH, J. Solid State Chem. 330 (2024) 124483, https://doi.org/10.1016/J.JSSC.2023.124483.

[19] F. Qureshi, M. Yusuf, S. Ahmed, M. Haq, A.M. Alraih, T. Hidouri, et al., Advancements in sorption-based materials for hydrogen storage and utilization: a comprehensive review, Energy 309 (2024) 132855, https://doi.org/10.1016/J.ENERGY.2024.132855.

[20] B. Wagner, M. Kim, M. Chowdhury, E. Vidales Pasos, K. Hizon, P. Ghildiyal, et al., Enhancing the combustion of magnesium nanoparticles via low-temperature plasma-induced hydrogenation, ACS Appl. Mater. Interfaces 15 (2023) 51639–51649, https://doi.org/10.1021/ACSAMI.3C12696/SUPPL_FILE/AM3C12696_SI_001.PDF.

[21] L. Mulky, S. Srivastava, T. Lakshmi, E.R. Sandadi, S. Gour, N.A. Thomas, et al., An overview of hydrogen storage technologies – key challenges and opportunities, Mater. Chem. Phys. 325 (2024) 129710, https://doi.org/10.1016/J.MATCHEMPHYS.2024.129710.

[22] P. Garra, G. Leyssens, O. Allgaier, C. Schönnenbeck, V. Tschamber, J.F. Brilhac, et al., Magnesium/air combustion at pilot scale and subsequent PM and NOx emissions, Appl. Energy 189 (2017) 578–587, https://doi.org/10.1016/J.APENERGY.2016.12.069.

[23] R. Bhandari, N. Adhikari, A comprehensive review on the role of hydrogen in renewable energy systems, Int. J. Hydrogen Energy 82 (2024) 923–951, https://doi.org/10.1016/J.IJHYDENE.2024.08.004.

[24] I.P. Jain, C. Lal, A. Jain, Hydrogen storage in Mg: a most promising material, Int. J. Hydrogen Energy 35 (2010) 5133–5144, https://doi.org/10.1016/J.IJHYDENE.2009.08.088.

[25] L. Yang, W. Zeng, Y. Li, Advancements in the modification of magnesium-based hydrogen storage materials, Prog. Nat. Sci. Mater. Int. 34 (2024) 540–554, https://doi.org/10.1016/J.PNSC.2024.05.001.

[26] M. Paskevicius, D.A. Sheppard, C.E. Buckley, Thermodynamic changes in mechanochemically synthesized magnesium hydride nanoparticles, J. Am. Chem. Soc. 132 (2010) 5077–5083, https://doi.org/10.1021/JA908398U.

[27] I.V. Drozdov, R. Vaßen, D. Stöver, Modelling and evaluation of hydrogen desorption kinetics controlled by surface reaction and bulk diffusion for magnesium hydride, RSC Adv (2014), https://doi.org/10.1039/C4RA08089K.

[28] Y. Xu, Y. Li, Q. Hou, Y. Hao, Z. Ding, Ball milling innovations advance Mg-Based hydrogen storage materials towards practical applications, Materials 17 (2024) 2510, https://doi.org/10.3390/MA17112510, 2510 2024;17.

[29] Yinghui Li, Qiuyu Zhang, Li Ren, Zi Li, Xi Lin, Zhewen Ma, et al., Core–shell nanostructured magnesium-based hydrogen storage materials: a critical review, Indust. Chem. Mater. 1 (2023) 282–298, https://doi.org/10.1039/D3IM00061C.

[30] J.J. Vajo, S.L. Skeith, F. Mertens, Reversible storage of hydrogen in destabilized LiBH 4, J. Phys. Chem. B 109 (2005) 3719–3722, https://doi.org/10.1021/JP040769O.

[31] K. Tanaka, Hydride stability and hydrogen desorption characteristics in melt-spun and nanocrystallized mg–ni–la alloy, J. Alloys Compd. 450 (2008) 432–439, https://doi.org/10.1016/J.JALLCOM.2006.10.160.

[32] Y. Sun, X. Zhang, W. Chen, J. Ye, S. Ju, K.F. Aguey-Zinsou, et al., Light-driven reversible hydrogen storage in light-weight metal hydrides enabled by photothermal effect, Small 18 (2022) 2202978, https://doi.org/10.1002/SMLL.202202978.

[33] X. Zhang, Y. Sun, S. Ju, J. Ye, X. Hu, W. Chen, et al., Solar-driven reversible hydrogen storage, Adv. Mater. 35 (2023) 2206946, https://doi.org/10.1002/ADMA.202206946. PAGE:STRING:ARTICLE/CHAPTER.

[34] X. Hu, X. Chen, X. Zhang, Y. Meng, G. Xia, X. Yu, et al., In situ construction of interface with photothermal and mutual catalytic effect for efficient solar-driven reversible hydrogen storage of MgH2, Adv. Sci. 11 (2024) 2400274, https://doi.org/10.1002/ADVS.202400274.

[35] X. Zhang, S. Ju, C. Li, J. Hao, Y. Sun, X. Hu, et al., Atomic reconstruction for realizing stable solar-driven reversible hydrogen storage of magnesium hydride, Nat. Commun. 15 (1) (2024) 2815, https://doi.org/10.1038/s41467-024-47077-y, 2024;15.

[36] X. Zhang, C. Li, J. Ye, X. Hu, W. Chen, F. Fang, et al., Light-enabled reversible hydrogen storage of borohydrides activated by photogenerated vacancies, J. Am. Chem. Soc. 147 (2025) 2786–2796, https://doi.org/10.1021/JACS.4C15744.

[37] J.W. Yeh, Physical metallurgy of high-entropy alloys, JOM 67 (2015) 2254–2261, https://doi.org/10.1007/S11837-015-1583-5/METRICS.

[38] B. Cantor, Multicomponent and high-entropy alloys, Entropy 16 (16) (2014) 4749–4768, https://doi.org/10.3390/E16094749, 2014;4749–68.

[39] H. Wang, J. Li, X. Wei, Y. Zheng, S. Yang, Y. Lu, et al., Thermodynamic and kinetic regulation for Mg-Based hydrogen storage materials: challenges, strategies, and perspectives, Adv. Funct. Mater. 34 (2024) 2406639, https://doi.org/10.1002/ADFM.202406639. JOURNAL:JOURNAL:10990712;PAGE:STRING:ARTICLE/CHAPTER.

[40] M.P. Mose, S.J. Huang, Enhanced hydrogen storage capacity and kinetics in AZ61 alloy with nickel and cobalt additives: insights into reaction mechanisms and activation energy, J. Alloys Compd. 984 (2024) 173934, https://doi.org/10.1016/J.JALLCOM.2024.173934.

[41] K.S. Nivedhitha, T. Beena, N.R. Banapurmath, M.A. Umarfarooq, V. Ramasamy, M.E.M. Soudagar, et al., Advances in hydrogen storage with metal hydrides: mechanisms, materials, and challenges, Int. J. Hydrogen Energy 61 (2024) 1259–1273, https://doi.org/10.1016/J.IJHYDENE.2024.02.335.

[42] J.M. Sander, L. Ismer, C.G. Van De Walle, Point-defect kinetics in α- and γ-MgH2, Int. J. Hydrogen Energy 41 (2016) 5688–5692, https://doi.org/10.1016/J.IJHYDENE.2016.01.156.

[43] M.A. Kuzovnikov, V.S. Efimchenko, E.V. Filatov, A.A. Maksimov, I.I. Tartakovskii, A.J. Ramirez-Cuesta, Raman scattering study of α-MgH2 and γ-MgH2, Solid State Commun. 154 (2013) 77–80, https://doi.org/10.1016/J.SSC.2012.09.022.

[44] J. Zhang, Z. Li, Y. Wu, X. Guo, J. Ye, B. Yuan, et al., Recent advances on the thermal destabilisation of Mg-based hydrogen storage materials, RSC Adv. 9 (2019) 408–428, https://doi.org/10.1039/C8RA05596C.

[45] M.G. Shelyapina, Hydrogen diffusion on, into and in magnesium probed by DFT: a review, Hydrogen 3 (2022) 285–302, https://doi.org/10.3390/HYDROGEN3030017, 2022;3:285–302.

[46] Y. Xinglin, L. Xiaohui, Z. Jiaqi, H. Quanhui, Z. Junhu, Progress in improving hydrogen storage properties of Mg-based materials, Mater. Today Adv. 19 (2023) 100387, https://doi.org/10.1016/J.MTADV.2023.100387.

[47] J. Lyu, V. Kudiiarov, A. Lider, Experimentally observed nucleation and growth behavior of Mg/MgH2 during De/Hydrogenation of MgH2/Mg: a review, Materials 15 (2022) 8004, https://doi.org/10.3390/MA15228004, 2022;15:8004.

[48] M.F. Saeid, B.A. Abdulkadir, S.Z. Abidin, H.D. Setiabudi, Nanoconfinement of magnesium hydride in porous scaffolds for hydrogen storage: kinetics, thermodynamics, and future prospects, Mater. Sci. Semicond. Process. 188 (2025) 109225, https://doi.org/10.1016/J.MSSP.2024.109225.

[49] Á. Révész, Á. Pintér, Time-dependent multi-particle model describing the hydrogen absorption of nanocrystalline magnesium powders: a case study, Energies 17 (2024) 2322, https://doi.org/10.3390/EN17102322, 2024;17:2322.

[50] Z. Wu, J. Fang, N. Liu, J. Wu, L. Kong, The improvement in hydrogen storage performance of mgh2 enabled by multilayer ti3c2, Micromachines (Basel) 12 (2021) 1190, https://doi.org/10.3390/MI12101190/S1.

[51] M.S. El-Eskandarany, E. Shaban, A. Al-Shemmiri, Integrated Ni/Nb2O5 nanocatalytic agent dose for improving the hydrogenation/dehydrogenation kinetics of reacted ball milled MgH2 powders, Int. J. Hydrogen Energy 39 (2014) 21097–21106, https://doi.org/10.1016/J.IJHYDENE.2014.10.076.

[52] S. Singh, A. Bhatnagar, V. Shukla, A.P. Pandey, M.A. Shaz, Three-dimensional graphene aerogel decorated with nickel nanoparticles as additive for improving the hydrogen storage properties of MgH2, Int. J. Hydrogen Energy 107 (2025) 96–107, https://doi.org/10.1016/J.IJHYDENE.2024.12.331.

[53] L. Zeng, Z. Lan, B. Li, H. Liang, X. Wen, X. Huang, et al., Facile synthesis of a Ni3S2@C composite using cation exchange resin as an efficient catalyst to improve the kinetic properties of MgH2, J. Magnesium Alloys 10 (2022) 3628–3640, https://doi.org/10.1016/J.JMA.2021.03.013.

[54] V. Zadorozhnyy, I. Tomilin, E. Berdonosova, C. Gammer, M. Zadorozhnyy, I. Savvotin, et al., Composition design, synthesis and hydrogen storage ability of multi-principal-component alloy TiVZrNbTa, J. Alloys Compd. 901 (2022) 163638, https://doi.org/10.1016/J.JALLCOM.2022.163638.

[55] J. Montero, C. Zlotea, G. Ek, J.C. Crivello, L. Laversenne, M. Sahlberg, TiVZrNb multi-principal-element alloy: synthesis optimization, structural, and hydrogen sorption properties, Molecules 24 (2019) 2799, https://doi.org/10.3390/MOLECULES24152799, 2019;24:2799.

[56] G. Ek, M.M. Nygård, A.F. Pavan, J. Montero, P.F. Henry, M.H. Sørby, et al., Elucidating the effects of the composition on hydrogen sorption in TiVZrNbHf-Based high-entropy alloys, Inorg. Chem. 60 (2020) 1124–1132, https://doi.org/10.1021/ACS.INORGCHEM.0C03270.

[57] L. Luo, H. Han, D. Feng, W. Lv, L. Chen, L. Li, et al., Nanocrystalline high-entropy alloys with ultrafast kinetics and high storage capacity for large-scale room-temperature-applicable hydrogen storage, Renewables 2 (2024) 138–149, https://doi.org/10.31635/RENEWABLES.024.202300049.

[58] B. Sarac, V. Zadorozhnyy, E. Berdonosova, Y.P. Ivanov, S. Klyamkin, S. Gumrukcu, et al., Hydrogen storage performance of the multi-principal-component CoFeMnTiVZr alloy in electrochemical and gas–solid reactions, RSC Adv. 10 (2020) 24613–24623, https://doi.org/10.1039/D0RA04089D.

[59] I. Kunce, M. Polanski, J. Bystrzycki, Structure and hydrogen storage properties of a high entropy ZrTiVCrFeNi alloy synthesized using Laser Engineered Net Shaping (LENS), Int. J. Hydrogen Energy 38 (2013) 12180–12189, https://doi.org/10.1016/J.IJHYDENE.2013.05.071.

[60] P. Edalati, R. Floriano, A. Mohammadi, Y. Li, G. Zepon, H.W. Li, et al., Reversible room temperature hydrogen storage in high-entropy alloy TiZrCrMnFeNi, Scr. Mater. 178 (2020) 387–390, https://doi.org/10.1016/J.SCRIPTAMAT.2019.12.009.

[61] F. Marques, M. Balcerzak, F. Winkelmann, G. Zepon, M. Felderhoff, Review and outlook on high-entropy alloys for hydrogen storage, Energy Environ. Sci. 14 (2021) 5191–5227, https://doi.org/10.1039/D1EE01543E.

[62] Y.J. Cho, H. Cho, E.S. Cho, Nanointerface engineering of metal hydrides for advanced hydrogen storage, Chem. Mater. 35 (2023) 366–385, https://doi.org/10.1021/ACS.CHEMMATER.2C02628/ASSET/IMAGES/MEDIUM/CM2C02628_0009.GIF.

[63] G. Ek, M.M. Nygård, A.F. Pavan, J. Montero, P.F. Henry, M.H. Sørby, et al., Elucidating the effects of the composition on hydrogen sorption in TiVZrNbHf-Based high-entropy alloys, Inorg. Chem. 60 (2021) 1124–1132, https://doi.org/10.1021/ACS.INORGCHEM.0C03270/ASSET/IMAGES/LARGE/IC0C03270_0008.JPEG.

[64] J. Montero, G. Ek, M. Sahlberg, C. Zlotea, Improving the hydrogen cycling properties by Mg addition in Ti-V-Zr-Nb refractory high entropy alloy, Scr. Mater. 194 (2021) 113699, https://doi.org/10.1016/J.SCRIPTAMAT.2020.113699.

[65] S. Wu, Y. Chen, W. Kang, X. Cai, L. Zhou, Hydrogen storage properties of MgTiVZrNb high-entropy alloy and its catalytic effect upon hydrogen storage in Mg, Int. J. Hydrogen Energy 50 (2024) 1113–1128, https://doi.org/10.1016/J.IJHYDENE.2023.09.022.

[66] F. Yin, et al., Structural and kinetic adjustments of Zr-based high-entropy alloys with Laves phases by substitution of Mg element - energy advances, Energy Adv 2 (2023) 1409, https://doi.org/10.1039/D3YA00243H. https://pubs.rsc.org/en/content/articlehtml/2023/ya/d3ya00243h. (Accessed 19 September 2025).

[67] Y. Liu, D. Chabane, O. Elkedim, Optimization of LaNi5 hydrogen storage properties by the combination of mechanical alloying and element substitution, Int. J. Hydrogen Energy 53 (2024) 394–402, https://doi.org/10.1016/J.IJHYDENE.2023.12.038.

[68] A. Hariyadi, S. Suwarno, R.V. Denys, J.B. von Colbe, T.O. Sætre, V. Yartys, Modelling of the hydrogen sorption kinetics in an AB2 laves type metal hydride alloy, J. Alloys Compd. 893 (2022) 162135, https://doi.org/10.1016/J.JALLCOM.2021.162135.

[69] W. Qiao, D. Yin, S. Zhao, N. Ding, L. Liang, C. Wang, et al., Effects of Cu doping on the hydrogen storage performance of Ti-Mn-based, AB2-type alloys, Chem. Eng. J. 465 (2023) 142837, https://doi.org/10.1016/J.CEJ.2023.142837.

[70] X. Li, Z. Yuan, C. Liu, Y. Sui, T. Zhai, Z. Hou, et al., Research progress in improved hydrogen storage properties of Mg-based alloys with metal-based materials and light metals, Int. J. Hydrogen Energy 50 (2024) 1401–1417, https://doi.org/10.1016/J.IJHYDENE.2023.09.265.

[71] Z. Sun, X. Lu, F.M. Nyahuma, N. Yan, J. Xiao, S. Su, et al., Enhancing hydrogen storage properties of MgH2 by transition metals and carbon materials: a brief review, Front. Chem. 8 (2020) 551701, https://doi.org/10.3389/FCHEM.2020.00552/FULL.

[72] M. Zhu, Y. Lu, L. Ouyang, H. Wang, Thermodynamic tuning of Mg-Based hydrogen storage alloys: a review, Materials 6 (2013) 4654–4674, https://doi.org/10.3390/MA6104654, 2013;6:4654–74.

[73] I.C. Atias-Adrian, F.A. Deorsola, G.A. Ortigoza-Villalba, B. Debenedetti, M. Baricco, Development of nanostructured Mg2Ni alloys for hydrogen storage applications, Int. J. Hydrogen Energy 36 (2011) 7897–7901, https://doi.org/10.1016/J.IJHYDENE.2011.01.047.

[74] Y. Wang, Y. Wang, Q. Zhang, L. Jiao, H. Yuan, Catalytic effects of different Ti-based materials on dehydrogenation performances of MgH2, J. Alloys Compd. 645 (2015) S509–S512, https://doi.org/10.1016/J.JALLCOM.2014.12.071.

[75] H. Yun, J. Bai, Z. He, H. Wang, Y. Wang, S. Cao, et al., Mechanical alloying to fabricate Mg10Co for the enhanced hydrogenation performance, Int. J. Hydrogen Energy 98 (2025) 266–279, https://doi.org/10.1016/J.IJHYDENE.2024.12.084.

[76] Z. Ding, Y. Li, H. Yang, Y. Lu, J. Tan, J. Li, et al., Tailoring MgH2 for hydrogen storage through nanoengineering and catalysis, J. Magnesium Alloys 10 (2022) 2946–2967, https://doi.org/10.1016/j.jma.2022.09.028.

[77] Z.Z. Wan, Z.M. Wang, D.H. Wang, Y. Zhong, J.Q. Deng, H.Y. Zhou, et al., Alloying effect study on thermodynamic stability of MgH2 by first-principles calculation, Chin. J. Chem. Phys. 29 (2016) 545–548, https://doi.org/10.1063/1674-0068/29/CJCP1602036.

[78] N. Kuganathan, M. Dornheim, D.M. Grant, S. Ling, Enhancing destabilisation of MgH2 with reactive elemental additives, J. Energy Storage 133 (2025) 117959, https://doi.org/10.1016/J.EST.2025.117959.

[79] D. Khan, J. Zou, S. Panda, W. Ding, Mechanism of thermodynamic destabilisation and fast desorption kinetics in a mechanically alloyed MgH2–In composite, J. Phys. Chem. C 124 (2020) 9685–9695, https://doi.org/10.1021/ACS.JPCC.0C00305.

[80] J. Cermak, L. Kral, P. Roupcova, A new light-element multi-principal-elements alloy AlMg2TiZn and its potential for hydrogen storage, Renew. Energy 198 (2022) 1186–1192, https://doi.org/10.1016/J.RENENE.2022.08.108.

[81] H. Wan, L. Ran, H. Lu, J. Qiu, H. Zhang, Y. Yang, et al., Optimizing microstructure and enhancing hydrogen storage properties in Mg alloy via tailoring Ni and Si element, J. Magnesium Alloys (2024), https://doi.org/10.1016/J.JMA.2024.01.014.

[82] J. Qiu, H. Wan, Y. Li, Z. Guo, Z. Ding, Y. Chen, et al., Multiscale mechanistic insights into Er-driven phase reconfiguration and hydrogen diffusion in Mg–Ni alloys, Nano Mater. Sci. 16 (2025) 7610–7636, https://doi.org/10.1016/j.nanoms.2025.09.013.

[83] L. Pasquini, The effects of nanostructure on the hydrogen sorption properties of magnesium-based metallic compounds: a review, Crystals 8 (2018) 106, https://doi.org/10.3390/CRYST8020106, 106 2018;8.

[84] L. Ren, Y. Li, N. Zhang, Z. Li, X. Lin, W. Zhu, et al., Nanostructuring of Mg-Based hydrogen storage materials: recent advances for promoting key applications, Nano-Micro Lett. 15 (2023) 1–27, https://doi.org/10.1007/S40820-023-01041-5, 1 2023;15.

[85] A. Schneemann, J.L. White, S. Kang, S. Jeong, L.F. Wan, E.S. Cho, et al., Nanostructured metal hydrides for hydrogen storage, Chem. Rev. 118 (2018) 10775–10839, https://doi.org/10.1021/ACS.CHEMREV.8B00313/ASSET/IMAGES/MEDIUM/CR-2018-00313K_0038. GIF.

[86] J.A. Bolarin, R. Zou, Z. Li, A. Munyentwali, Z. Zhang, H. Cao, Recent path to ultrafine Mg/MgH2 synthesis for sustainable hydrogen storage, Int. J. Hydrogen Energy 52 (2024) 251–274, https://doi.org/10.1016/J.IJHYDENE.2023.04.234.

[87] Y. Xu, Y. Zhou, Y. Li, Y. Hao, P. Wu, Z. Ding, Recent advances in the preparation methods of magnesium-based hydrogen storage materials, Molecules 29 (2024) 2451, https://doi.org/10.3390/MOLECULES29112451, 2024;29:2451.

[88] J. Zou, S. Long, L. Zhang, C. Lu, X. Chen, X. Zeng, et al., Hydrogen sorption behaviors of a core–shell structured mg@fe composite powder, Mater. Trans. 55 (2014) 1156–1160, https://doi.org/10.2320/MATERTRANS.MG201418.

[89] C. Lu, Y. Ma, F. Li, H. Zhu, X. Zeng, W. Ding, et al., Visualization of fast "hydrogen pump" in core–shell nanostructured Mg@Pt through hydrogen-stabilized Mg3Pt, J. Mater. Chem. A Mater. 7 (2019) 14629–14637, https://doi.org/10.1039/C9TA03038G.

[90] K.J. Jeon, H.R. Moon, A.M. Ruminski, B. Jiang, C. Kisielowski, R. Bardhan, et al., Air-stable magnesium nanocomposites provide rapid and high-capacity hydrogen storage without using heavy-metal catalysts, Nat. Mater. 10 (2011) 286–290, https://doi.org/10.1038/NMAT2978. SUBJMETA.

[91] T.K. Nielsen, K. Manickam, M. Hirscher, F. Besenbacher, T.R. Jensen, Confinement of MgH2 nanoclusters within nanoporous aerogel scaffold materials, ACS Nano 3 (2009) 3521–3528, https://doi.org/10.1021/NN901072W.

[92] Z. Zhang, Y. Wang, H. Wang, X. Xue, Q. Lin, Metal-organic frameworks promoted hydrogen storage properties of magnesium hydride for In-Situ resource utilization (ISRU) on Mars, Front. Mater. 8 (2021) 766288, https://doi.org/10.3389/FMATS.2021.766288/BIBTEX.

[93] M. Chen, X. Xiao, X. Wang, Y. Lu, M. Zhang, J. Zheng, et al., Self-templated carbon enhancing catalytic effect of ZrO2 nanoparticles on the excellent dehydrogenation kinetics of MgH2, Carbon N Y 166 (2020) 46–55, https://doi.org/10.1016/J.CARBON.2020.05.025.

[94] M. Hu, X. Xie, M. Chen, C. Zhu, T. Liu, TiCX-decorated Mg nanoparticles confined in carbon shell: preparation and catalytic mechanism for hydrogen storage, J. Alloys Compd. 817 (2020) 152813, https://doi.org/10.1016/J.JALLCOM.2019.152813.

[95] Y. Li, Z. Ding, H. Jiang, G. Lin, S. Li, W. Du, et al., Spatially programmed confinement catalysis enables high-performance magnesium hydrogen storage, Nano Lett. 25 (2025) 16801–16808, https://doi.org/10.1021/acs.nanolett.5c04450.

[96] Y. Wang, Z. Lan, X. Huang, H. Liu, J. Guo, Study on catalytic effect and mechanism of MOF (MOF = ZIF-8, ZIF-67, MOF-74) on hydrogen storage properties of magnesium, Int. J. Hydrogen Energy 44 (2019) 28863–28873, https://doi.org/10.1016/J.IJHYDENE.2019.09.110.
[97] Y. Jia, C. Sun, Y. Peng, W. Fang, X. Yan, D. Yang, et al., Metallic Ni nanocatalyst in situ formed from a metal–organic-framework by mechanochemical reaction for hydrogen storage in magnesium, J. Mater. Chem. A Mater. 3 (2015) 8294–8299, https://doi.org/10.1039/C5TA00278H.
[98] Z. Ma, J. Zou, D. Khan, W. Zhu, C. Hu, X. Zeng, et al., Preparation and hydrogen storage properties of MgH2-trimesic acid-TM MOF (TM=Co, Fe) composites, J. Mater. Sci. Technol. 35 (2019) 2132–2143, https://doi.org/10.1016/J.JMST.2019.05.049.
[99] H. Jiang, Z. Ding, Y. Li, G. Lin, S. Li, W. Du, et al., Hierarchical interface engineering for advanced magnesium-based hydrogen storage: synergistic effects of structural design and compositional modification, Chem. Sci. 16 (2025) 7610–7636, https://doi.org/10.1039/d5sc01169h.
[100] H. Wang, J. Li, X. Wei, Y. Zheng, S. Yang, Y. Lu, et al., Thermodynamic and kinetic regulation for Mg-Based hydrogen storage materials: challenges, strategies, and perspectives, Adv. Funct. Mater. 34 (2024) 2406639, https://doi.org/10.1002/ADFM.202406639.
[101] B. Li, J. Li, H. Zhao, X. Yu, H. Shao, Mg-based metastable nano alloys for hydrogen storage, Int. J. Hydrogen Energy 44 (2019) 6007–6018, https://doi.org/10.1016/J.IJHYDENE.2019.01.127.
[102] C. Shen, K.F. Aguey-Zinsou, Can γ-MgH2 improve the hydrogen storage properties of magnesium? J. Mater. Chem. A Mater. 5 (2017) 8644–8652, https://doi.org/10.1039/C7TA01724C.
[103] X. Yao, C. Wu, A. Du, G.Q. Lu, H. Cheng, S.C. Smith, et al., Mg-based nanocomposites with high capacity and fast kinetics for hydrogen storage, J. Phys. Chem. B 110 (2006) 11697–11703, https://doi.org/10.1021/JP057526W. PAGE:STRING:ARTICLE/CHAPTER.
[104] T. Liu, C. Wang, Y. Wu, Mg-based nanocomposites with improved hydrogen storage performances, Int. J. Hydrogen Energy 39 (2014) 14262–14274, https://doi.org/10.1016/J.IJHYDENE.2014.03.125.
[105] Y. Zavalii, V.V. Berezovets, R.V. Denys, Nanocomposites based on magnesium for hydrogen storage: achievements and prospects (A Survey), Mater. Sci. 54 (2019) 611–626, https://doi.org/10.1007/S11003-019-00226-X/METRICS.
[106] S. Guemou, L. Zhang, S. Li, Y. Jiang, T. Zhong, Z. Lu, et al., Exceptional catalytic effect of novel rGO-supported Ni-Nb nanocomposite on the hydrogen storage properties of MgH2, J. Mater. Sci. Technol. 172 (2024) 83–93, https://doi.org/10.1016/J.JMST.2023.07.016.
[107] G. Liu, Y. Wang, F. Qiu, L. Li, L. Jiao, H. Yuan, Synthesis of porous Ni@rGO nanocomposite and its synergetic effect on hydrogen sorption properties of MgH2, J. Mater. Chem. 22 (2012) 22542–22549, https://doi.org/10.1039/C2JM34730J.
[108] C. Duan, Y. Tian, X. Wang, M. Wu, D. Fu, Y. Zhang, et al., Ni-CNTs as an efficient confining framework and catalyst for improving dehydriding/rehydriding properties of MgH2, Renew. Energy 187 (2022) 417–427, https://doi.org/10.1016/J.RENENE.2022.01.048.
[109] W. Zhu, L. Ren, Y. Li, C. Lu, X. Lin, Q. Zhang, et al., In situ high-energy synchrotron X-ray studies in thermodynamics of mg-in-ti hydrogen storage system, Energy Mater. Adv. 4 (2023) 1–12, https://doi.org/10.34133/ENERGYMATADV.0069/SUPPL_FILE/ENERGYMATADV.0069.F1.DOCX.
[110] O.P. Gbenebor, A.P.I. Popoola, Transition metal-based materials and their catalytic influence on MgH2 hydrogen storage: a review, Int. J. Renew. Energy Dev. 12 (2023) 1141–1159, https://doi.org/10.14710/IJRED.2023.57805.
[111] T. Liu, T. Zhang, C. Qin, M. Zhu, X. Li, Improved hydrogen storage properties of Mg–V nanoparticles prepared by hydrogen plasma–metal reaction, J. Power Sources 196 (2011) 9599–9604, https://doi.org/10.1016/J.JPOWSOUR.2011.07.078.
[112] T. Liu, C. Qin, T. Zhang, Y. Cao, M. Zhu, X. Li, Synthesis of Mg@Mg 17Al 12 ultrafine particles with superior hydrogen storage properties by hydrogen plasma-metal reaction, J. Mater. Chem. 22 (2012) 19831–19838, https://doi.org/10.1039/C2JM33911K.
[113] T. Liu, Y. Cao, C. Qin, W. Chou, X. Li, Synthesis and hydrogen storage properties of Mg–10.6La–3.5Ni nanoparticles, J. Power Sources 246 (2014) 277–282, https://doi.org/10.1016/J.JPOWSOUR.2013.07.087.
[114] T. Liu, C. Qin, M. Zhu, Y. Cao, H. Shen, X. Li, Synthesis and hydrogen storage properties of mg-la-al nanoparticles, J. Power Sources 219 (2012) 100–105, https://doi.org/10.1016/J.JPOWSOUR.2012.07.027.
[115] Y. Wu, M.V. Lototskyy, J.K. Solberg, V.A. Yartys, Effect of microstructure on the phase composition and hydrogen absorption-desorption behaviour of melt-spun Mg-20Ni-8Mm alloys, Int. J. Hydrogen Energy 37 (2012) 1495–1508, https://doi.org/10.1016/J.IJHYDENE.2011.09.126.
[116] W. Zhu, L. Ren, Y. Li, C. Lu, X. Lin, Q. Zhang, et al., In situ high-energy synchrotron X-ray studies in thermodynamics of mg-in-ti hydrogen storage system, Energy Mater. Adv. 4 (2023) 1–12, https://doi.org/10.34133/ENERGYMATADV.0069.
[117] X.L. Zhang, Y.F. Liu, X. Zhang, J.J. Hu, M.X. Gao, H.G. Pan, Empowering hydrogen storage performance of MgH2 by nanoengineering and nanocatalysis, Mater. Today Nano 9 (2020) 100064, https://doi.org/10.1016/j.mtnano.2019.100064.
[118] H. Hong, A.R.P. Harrison, B. Nie, Linking the microstructure of ball-milled Mg–Ni hydrogen storage materials to reactive properties and techno-economic feasibility, Energy Fuels 39 (2025) 13789–13800, https://doi.org/10.1021/acs.energyfuels.5c01986.
[119] M.S. El-Eskandarany, E. Shaban, F. Aldakheel, A. Alkandary, M. Behbehani, M. Al-Saidi, Synthetic nanocomposite MgH2/5 wt.% TiMn2 powders for solid-hydrogen storage tank integrated with PEM fuel cell, Sci. Rep. 7 (1) (2017) 13296, https://doi.org/10.1038/s41598-017-13483-0, 2017;7.
[120] L. Ren, Y. Li, N. Zhang, Z. Li, X. Lin, W. Zhu, et al., Nanostructuring of Mg-Based hydrogen storage materials: recent advances for promoting key applications, Nano-Micro Lett. 15 (1) (2023) 93, https://doi.org/10.1007/s40820-023-01041-5, 2023;15.
[121] H. Wang, H. Yan, J. Ren, B. Li, S. Nyallang Nyamsi, Z. Wu, Microwave plasma enhancing Mg-Based hydrogen storage: thermodynamics evaluation and economic analysis of coupling SOFC for heat and power generation, Front. Thermal Eng. 2 (2022) 886322, https://doi.org/10.3389/fther.2022.886322.
[122] L. Pasquini, K. Sakaki, E. Akiba, M.D. Allendorf, E. Alvares, J.R. Ares, et al., Magnesium- and intermetallic alloys-based hydrides for energy storage: modelling, synthesis and properties, Prog. Energy 4 (2022) 032007, https://doi.org/10.1088/2516-1083/AC7190.
[123] Y. Xu, Y. Zhou, Y. Li, Y. Hao, P. Wu, Z. Ding, Magnesium-based hydrogen storage alloys: advances, strategies, and future outlook for clean energy applications, Molecules 29 (2024) 2525, https://doi.org/10.3390/molecules29112525, 2525 2024;29.
[124] A. Alaoui-Belghiti, A. Assila, I. Belkoufa, M. Rkhis, S. Laasri, M. Tlemçani, et al., Strain engineering for optimized hydrogen storage: enhancing ionic conductivity and achieving near-room-temperature desorption in Mg_2NiH_4, Int. J. Hydrogen Energy 92 (2024) 1069–1077, https://doi.org/10.1016/j.ijhydene.2024.10.292.
[125] H. Itoh, O. Yoshinari, K. Tanaka, Study of hydrogen storage in Mg2Ni by thermal desorption spectrometry, J. Alloys Compd. 231 (1995) 483–487, https://doi.org/10.1016/0925-8388(95)01868-9.
[126] H. Yang, Z. Ding, Y.T. Li, S.Y. Li, P.K. Wu, Q.H. Hou, et al., Recent advances in kinetic and thermodynamic regulation of magnesium hydride for hydrogen storage, Rare Met. 42 (2023) 2906–2927, https://doi.org/10.1007/S12598-023-02306-Z.
[127] M.R. Ghaani, M. Catti, N.J. English, In situ synchrotron X-ray diffraction studies of hydrogen-desorption properties of 2LiBH4–Mg2FeH6 composite, Molecules 26 (2021) 4853, https://doi.org/10.3390/molecules26164853, 2021;26:4853.
[128] G. Li, M. Matsuo, S. Takagi, A.L. Chaudhary, T. Sato, M. Dornheim, et al., Thermodynamic properties and reversible hydrogenation of LiBH4–Mg2FeH6 composite materials, Inorganics 5 (2017) 81, https://doi.org/10.3390/inorganics5040081, 81 2017;5.
[129] E.M. Dematteis, S. Vaunois, C. Pistidda, M. Dornheim, M. Baricco, Reactive hydride composite of Mg2NiH4 with borohydrides eutectic mixtures, Crystals 8 (2018) 90, https://doi.org/10.3390/cryst8020090. Page 90 2018;8.
[130] J.J. Vajo, S.L. Skeith, F. Mertens, Reversible storage of hydrogen in destabilized LiBH4, J. Phys. Chem. B 109 (2005) 3719–3722, https://doi.org/10.1021/jp040769o.
[131] W. Chen, Y.H. Sun, T. Xu, X Bin Yu, G.L. Xia, Enhancing reversible hydrogen storage performance of 2LiBH4–MgH2 via in-situ building heterogeneous nucleation sites, Rare Met. 43 (2024) 4367–4376, https://doi.org/10.1007/s12598-024-02762-1.
[132] Z. Ding, H. Li, L. Shaw, New insights into the solid-state hydrogen storage of nanostructured LiBH4-MgH2 system, Chem. Eng. J. 385 (2020) 123856, https://doi.org/10.1016/j.cej.2019.123856.
[133] F. Yang, J. Wang, Y. Zhang, Z. Wu, Z. Zhang, F. Zhao, et al., Recent progress on the development of high-entropy alloys (HEAs) for solid hydrogen storage: a review, Int. J. Hydrogen Energy 47 (2022) 11236–11249, https://doi.org/10.1016/J.IJHYDENE.2022.01.141.
[134] F. Marques, H.C. Pinto, S.J.A. Figueroa, F. Winkelmann, M. Felderhoff, W. J. Botta, et al., Mg-containing multi-principal element alloys for hydrogen storage: a study of the MgTiNbCr0.5Mn0.5Ni0.5 and Mg0.68TiNbNi0.55 compositions, Int. J. Hydrogen Energy 45 (2020) 19539–19552, https://doi.org/10.1016/J.IJHYDENE.2020.05.069.
[135] Y. Deng, J. Hu, S. Zhao, W. Wang, L. Xie, G. Sun, et al., Hydrogen storage properties of Mg0.10Ti0.30V0.25Zr0.10Nb0.25 lightweight high entropy alloy: a theoretical study, Int. J. Hydrogen Energy 50 (2024) 314–323, https://doi.org/10.1016/J.IJHYDENE.2023.07.075.
[136] G. Zepon, D.R. Leiva, R.B. Strozi, A. Bedoch, S.J.A. Figueroa, T.T. Ishikawa, et al., Hydrogen-induced phase transition of MgZrTiFe0.5Co0.5Ni0.5 high entropy alloy, Int. J. Hydrogen Energy 43 (2018) 1702–1708, https://doi.org/10.1016/J.IJHYDENE.2017.11.106.
[137] R.B. Strozi, D.R. Leiva, J. Huot, W.J. Botta, G. Zepon, Synthesis and hydrogen storage behavior of Mg–V–Al–Cr–Ni high-entropy alloys, Int. J. Hydrogen Energy 46 (2021) 2351–2361, https://doi.org/10.1016/J.IJHYDENE.2020.10.106.
[138] D.S. Pyle, E.M.A. Gray, C.J. Webb, A sieverts apparatus for measuring high-pressure hydrogen isotherms on porous materials, Int. J. Hydrogen Energy 42 (2017) 20111–20119, https://doi.org/10.1016/J.IJHYDENE.2017.06.126.
[139] M.S. El-Eskandarany, Recent developments in the fabrication, characterization and implementation of MgH 2 -based solid-hydrogen materials in the Kuwait institute for scientific research, RSC Adv. 9 (2019) 9907–9930, https://doi.org/10.1039/C9RA00287A.
[140] Y. Yu, Y. Ji, S. Zhang, S. Wang, Y. Chen, H. yong, et al., Microstructure characteristics, hydrogen storage thermodynamic and kinetic properties of Mg–Ni–Y based hydrogen storage alloys, Int. J. Hydrogen Energy 47 (2022) 27059–27070, https://doi.org/10.1016/J.IJHYDENE.2022.06.056.
[141] D. Karlsson, G. Ek, J. Cedervall, C. Zlotea, K.T. Møller, T.C. Hansen, et al., Structure and hydrogenation properties of a HfNbTiVZr high-entropy alloy, Inorg. Chem. 57 (2018) 2103–2110, https://doi.org/10.1021/ACS.INORGCHEM.7B03004.

[142] C. Zhang, A. Song, Y. Yuan, Y. Wu, P. Zhang, Z. Lu, et al., Study on the hydrogen storage properties of a TiZrNbTa high entropy alloy, Int. J. Hydrogen Energy 45 (2020) 5367–5374, https://doi.org/10.1016/J.IJHYDENE.2019.05.214.
[143] V. Zadorozhnyy, B. Sarac, E. Berdonosova, T. Karazehir, A. Lassnig, C. Gammer, et al., Evaluation of hydrogen storage performance of ZrTiVNiCrFe in electrochemical and gas-solid reactions, Int. J. Hydrogen Energy 45 (2020) 5347–5355, https://doi.org/10.1016/J.IJHYDENE.2019.06.157.
[144] P. Edalati, G. Andrade, R.B. Strozi, S. Dangwal, K. Edalati, R. Floriano, Room temperature hydrogen storage properties of Ti-Zr-Mn-Fe-Co high-entropy alloys designed by semi-empirical descriptors, thermodynamic calculations and machine learning, J. Alloys Compd. 1022 (2025) 180051, https://doi.org/10.1016/J.JALLCOM.2025.180051.
[145] Y. Liu, Y. Guo, Y. Jiang, L. Feng, Y. Sun, Y. Wang, Recent progress in thermodynamic and kinetics modification of magnesium hydride hydrogen storage materials, Mater. Rep. Energy 4 (2024) 100252, https://doi.org/10.1016/J.MATRE.2024.100252.
[146] Z. Ding, Y. Li, H. Yang, Y. Lu, J. Tan, J. Li, et al., Tailoring MgH2 for hydrogen storage through nanoengineering and catalysis, J. Magnesium Alloys 10 (2022) 2946–2967, https://doi.org/10.1016/J.JMA.2022.09.028.
[147] J. de Jesús Vega-Soria, E.D. Ruiz-Santacruz, N.L. Torres-García, K. Suárez-Alcántara, Systematic study of first-row transition metals chlorides as reaction accelerators for Mg/MgH2 for hydrogen storage application, Int. J. Hydrogen Energy 141 (2025) 979–995, https://doi.org/10.1016/J.IJHYDENE.2024.09.440.
[148] R.L. Corey, T.M. Ivancic, D.T. Shane, E.A. Carl, R.C. Bowman, JMB Von Colbe, et al., Hydrogen motion in magnesium hydride by NMR, J. Phys. Chem. C 112 (2008) 19784–19790, https://doi.org/10.1021/JP807900R. WGROUP:STRING:ACHS.
[149] M.W. Rahman, M.N. Siddiquee, M.M. Hossain, M.J. Uddin, Effect of Mg–Nb oxides on hydrogen sorption kinetics of ball-milled MgH2, Clean Energy 9 (2025) 169–178, https://doi.org/10.1093/CE/ZKAE108.
[150] A. Perejón, P.E. Sánchez-Jiménez, J.M. Criado, L.A. Pérez-Maqueda, Magnesium hydride for energy storage applications: the kinetics of dehydrogenation under different working conditions, J. Alloys Compd. 681 (2016) 571–579, https://doi.org/10.1016/J.JALLCOM.2016.04.191.
[151] M. Ismail, The hydrogen storage properties of destabilized MgH2–AlH3 (2:1) system, Mater. Today Proc. 3 (2016) S80–S87, https://doi.org/10.1016/J.MATPR.2016.01.011.
[152] B. Cheng, Y. Li, X. Li, H. Ke, L. Wang, T. Cao, et al., Solid-state hydrogen storage properties of Ti–V–Nb–Cr high-entropy alloys and the associated effects of transitional metals (M = Mn, Fe, Ni), Acta Metallurgica Sinica (English Letters) 36 (2023) 1113–1122, https://doi.org/10.1007/S40195-022-01403-9/FIGURES/7.
[153] Y. Liu, D. Chabane, O. Elkedim, Intermetallic compounds synthesized by mechanical alloying for solid-state hydrogen storage: a review, Energies 14 (2021) 5758, https://doi.org/10.3390/EN14185758, 2021;14:5758.
[154] F.M. Nyahuma, L. Zhang, M. Song, X. Lu, B. Xiao, J. Zheng, et al., Significantly improved hydrogen storage behaviors in MgH2 with Nb nanocatalyst, Int. J. Min. Met. Mater. 29 (2022) 1788–1797, https://doi.org/10.1007/S12613-021-2303-5/METRICS.
[155] N.N. Sulaiman, M. Ismail, Study the effect of SrFe12O19 on MgH2/LiAlH4 composite for solid-state hydrogen storage, Int. J. Hydrogen Energy 42 (2017) 29830–29839, https://doi.org/10.1016/J.IJHYDENE.2017.10.071.
[156] A. Motavalli, M. Rajabi, A. Gholipoor, Effect of milling time on hydrogen desorption properties of nanocrystalline MgH 2, J. Adv. Mater. Process. 2 (2014) 67–72.
[157] T. Sadhasivam, H.T. Kim, S. Jung, S.H. Roh, J.H. Park, H.Y. Jung, Dimensional effects of nanostructured Mg/MgH2 for hydrogen storage applications: a review, Renew. Sustain. Energy Rev. 72 (2017) 523–534, https://doi.org/10.1016/J.RSER.2017.01.107.
[158] L. Ren, Y. Li, N. Zhang, Z. Li, X. Lin, W. Zhu, et al., Nanostructuring of Mg-Based hydrogen storage materials: recent advances for promoting key applications, Nano-Micro Lett. 15 (2023) 1–27, https://doi.org/10.1007/S40820-023-01041-5/FIGURES/5.
[159] M. Tian, C. Shang, Nano-structured MgH2 catalyzed by TiC nanoparticles for hydrogen storage, J. Chem. Technol. Biotechnol. 86 (2011) 69–74, https://doi.org/10.1002/JCTB.2479;CTYPE:STRING:JOURNAL.
[160] Q. Wan, P. Li, Z. Li, F. Zhai, X. Qu, A.A. Volinsky, Improved hydrogen storage performance of MgH2–LiAlH4 composite by addition of MnFe2O4, J. Phys. Chem. C 117 (2013) 26940–26947, https://doi.org/10.1021/JP410449Q.
[161] A. Kumar Prajapati, -A. Bhatnagar, L.J. Huang, S.T. Shi, J. Cui, et al., Enhanced dehydrogenation properties of MgH2 by the synergetic effects of transition metal carbides and graphene, Nanotechnology 34 (2023) 325704, https://doi.org/10.1088/1361-6528/ACD259.
[162] Y. Zhang, J. Zheng, Z. Lu, M. Song, J. He, F. Wu, et al., Boosting the hydrogen storage performance of magnesium hydride with metal organic framework-derived Cobalt@Nickel oxide bimetallic catalyst, Chin. J. Chem. Eng. 52 (2022) 161–171, https://doi.org/10.1016/J.CJCHE.2022.06.026.
[163] G. Liang, J. Huot, S. Boily, A. Van Neste, R. Schulz, Catalytic effect of transition metals on hydrogen sorption in nanocrystalline ball milled MgH2–Tm (Tm=Ti, V, Mn, Fe and Ni) systems, J. Alloys Compd. 292 (1999) 247–252, https://doi.org/10.1016/S0925-8388(99)00442-9.
[164] Y. Yin, B. Li, Z. Yuan, Y. Qi, Y. Zhang, A comparison of TiF 3 and NbF 5 catalytic effects on hydrogen absorption and desorption kinetics of a ball-milled Mg 85 Zn 5 Ni 10 alloy, RSC Adv. 8 (2018) 34525–34535, https://doi.org/10.1039/C8RA06500D.
[165] H. Xiao, X. Zhang, C. Li, Y. Li, C. Ma, R. Wang, et al., Enhanced hydrogen-storage properties of MgH2 catalyzed via a cerium doped TiCrV BCC alloy, Metals (Basel) 14 (2024) 572, https://doi.org/10.3390/MET14050572/S1.
[166] B. Sun, Y. Chen, G. Zhang, S. Ni, C. Li, X. Li, Investigation on the in situ generated Tih2 and Mg2ni for the hydrogen absorption and desorption performance of Mg90ni10-Ti. https://doi.org/10.2139/SSRN.4963680, 2024.
[167] P. Huen, M. Paskevicius, B. Richter, D.B. Ravnsbæk, T.R. Jensen, Hydrogen storage stability of nanoconfined MgH2 upon cycling, Inorganics 5 (2017) 57, https://doi.org/10.3390/INORGANICS5030057. Page 57 2017;5.
[168] H. Liu, C. Lu, X. Wang, L. Xu, X. Huang, X. Wang, et al., Combinations of V2C and Ti3C2MXenes for boosting the hydrogen storage performances of MgH2, ACS Appl. Mater. Interfaces 13 (2021) 13235–13247, https://doi.org/10.1021/ACSAMI.0C23150/SUPPL_FILE/AM0C23150_SI_001.PDF.
[169] Z. Li, K. Xian, M. Gao, Q. Shanqing, W. Meihong, J. Gan, et al., Remarkable De/Hydrogenation Kinetics and Long-Term Cycling Stability for 2libh4-Mgh2 System via 2d Tinb2o7 Nanoflake Catalyzing, 2024, https://doi.org/10.2139/SSRN.4762192.
[170] A.I. Osman, A. Ayati, M. Farrokhi, S. Khadempir, A. Reza Rajabzadeh, M. Farghali, et al., Innovations in hydrogen storage materials: synthesis, applications, and prospects. https://doi.org/10.1016/j.est.2024.112376, 2024.
[171] D.R. Leiva, A.M. Jorge, T.T. Ishikawa, W.J. Botta, Hydrogen storage in Mg and Mg-Based alloys and composites processed by severe plastic deformation, Mater. Trans. 60 (2019) 1561–1570, https://doi.org/10.2320/MATERTRANS.MF201927.
[172] J.O. Fadonougbo, K. Szczepańska, A. Baran, I. Wyrębska, P. Płatek, J. Janiszewski, et al., Combinatorial synthesis of solid-state hydrogen storage materials using a modified planetary ball mill, Int. J. Hydrogen Energy 101 (2025) 946–958, https://doi.org/10.1016/J.IJHYDENE.2024.12.464.
[173] N. Küçükdeveci, I. Akay Erdoğan, A. Binal Aybar, M. Anik, Electrochemical hydrogen storage properties of mechanically alloyed Mg0.8Ti0.2-xMnxNi (x = 0, 0.025, 0.05, 0.1) type alloys, Int. J. Hydrogen Energy 47 (2022) 2511–2519, https://doi.org/10.1016/J.IJHYDENE.2021.10.174.
[174] Y. Sui, Z. Yuan, D. Zhou, T. Zhai, X. Li, D. Feng, et al., Recent progress of nanotechnology in enhancing hydrogen storage performance of magnesium-based materials: a review, Int. J. Hydrogen Energy 47 (2022) 30546–30566, https://doi.org/10.1016/J.IJHYDENE.2022.06.310.
[175] C. Suryanarayana, Mechanical alloying: a novel technique to synthesize, Adv. Mater. Res. 2019 (2019) 4219812, https://doi.org/10.34133/2019/4219812.
[176] S.J. Huang, M.P. Mose, High-energy ball milling-induced crystallographic structure changes of AZ61-Mg alloy for improved hydrogen storage, J. Energy Storage 68 (2023) 107773, https://doi.org/10.1016/J.EST.2023.107773.
[177] V. Khodaparast, M. Rajabi, Hydrogen desorption properties of MgH2-5 wt.% ti-mn-cr composite via combined melt spinning and mechanical alloying, Procedia Mater. Sci. 11 (2015) 611–615, https://doi.org/10.1016/J.MSPRO.2015.11.092.
[178] J.K. Bendyna, S. Dyjak, P.H.L. Notten, The influence of ball-milling time on the dehydrogenation properties of the NaAlH4–MgH2 composite, Int. J. Hydrogen Energy 40 (2015) 4200–4206, https://doi.org/10.1016/J.IJHYDENE.2015.01.026.
[179] X. Ou, J. Li, H. Lv, L. Wang, T. Yang, Effect of nanosized nickel diselenide on hydrogen storage properties of ball-milled magnesium hydride, Int. J. Hydrogen Energy 101 (2025) 594–604, https://doi.org/10.1016/J.IJHYDENE.2024.12.465.
[180] D. Zhou, C. Zheng, Y. Niu, D. Feng, H. Ren, Y. Zhang, et al., Hydrogen storage property improvement of ball-milled Mg2.3Y0.1Ni alloy with graphene, Int. J. Hydrogen Energy 50 (2024) 123–135, https://doi.org/10.1016/J.IJHYDENE.2023.06.255.
[181] H. Wu, Y. Ji, Y. Chen, Y. Zhang, H. Yong, Y. Zhang, Microstructure, hydrogen storage properties, and thermodynamic characterization of ball-milled Mg90Ni5Y5 alloy, J. Phys. Chem. Solid. 195 (2024) 112284, https://doi.org/10.1016/J.JPCS.2024.112284.
[182] C. Zheng, D. Zhou, D. Feng, H. Ren, Y. Zhang, Effect of Y content on the hydrogen storage properties of ball-milled Mg2.4-xYxNi (x = 0.05, 0.1, 0.15, 0.2) alloys, J. Phys. Chem. Solid. 178 (2023) 111320, https://doi.org/10.1016/J.JPCS.2023.111320.
[183] K.R. Cardoso, V. Roche, A.M. Jorge, F.J. Antiqueira, G. Zepon, Y. Champion, Hydrogen storage in MgAlTiFeNi high entropy alloy, J. Alloys Compd. 858 (2021) 158357, https://doi.org/10.1016/J.JALLCOM.2020.158357.
[184] M.O. de Marco, Y. Li, H.W. Li, K. Edalati, R. Floriano, Mechanical synthesis and hydrogen storage characterization of MgVCr and MgVTiCrFe high-entropy alloy, Adv. Eng. Mater. 22 (2020) 1901079, https://doi.org/10.1002/ADEM.201901079.
[185] R.C. Muduli, P. Kale, Synergetic effect of porous silicon–nickel composite on its solid-state hydrogen energy storage properties, Int. J. Hydrogen Energy 48 (2023) 35185–35196, https://doi.org/10.1016/J.IJHYDENE.2023.05.268.
[186] M. Lototskyy, J.M. Sibanyoni, R.V. Denys, M. Williams, B.G. Pollet, V.A. Yartys, Magnesium–carbon hydrogen storage hybrid materials produced by reactive ball milling in hydrogen, Carbon N Y 57 (2013) 146–160, https://doi.org/10.1016/J.CARBON.2013.01.058.
[187] A. Baran, T.R. Jensen, M. Polański, High-temperature high-pressure reactive ball milling synthesis of Mg-Ni-based solid-state hydrogen storage materials, J. Energy Storage 103 (2024) 114271, https://doi.org/10.1016/J.EST.2024.114271.
[188] M.S. El-Eskandarany, F. Al-Ajmi, M. Banyan, A. Al-Duweesh, Synergetic effect of reactive ball milling and cold pressing on enhancing the hydrogen storage behavior of nanocomposite MgH2/10 wt.% TiMn2 binary system, Int. J. Hydrogen Energy 44 (2019) 26428–26443, https://doi.org/10.1016/J.IJHYDENE.2019.08.093.

[189] M. Sherif El-Eskandarany, H.S. Almatrouk, E. Shaban, Hydrogenation/dehydrogenation kinetics study of reacted ball milled (MgH2)100-x/(Ni)y/(Nb2O5)z)x nanocomposite powders, Mater. Today Proc. 3 (2016) 2735–2743, https://doi.org/10.1016/J.MATPR.2016.06.020.
[190] L. Farina, S. Brutti, F. Trequattrini, O. Palumbo, S. Gatto, P. Reale, et al., An extensive study of the MgFeH material obtained by reactive ball milling of MgH2 and Fe in a molar ratio 3:1, Int. J. Hydrogen Energy 42 (2017) 22333–22341, https://doi.org/10.1016/J.IJHYDENE.2017.04.232.
[191] K. Mombini, K. Gheisari, M. Reihanian, Exploring novel magnetic behaviors in cobalt-doped magnetite synthesized by plasma arc discharge method, Mater. Today Commun. 41 (2024) 110550, https://doi.org/10.1016/J.MTCOMM.2024.110550.
[192] J. Mao, J. Zou, C. Lu, X. Zeng, W. Ding, Hydrogen storage and hydrolysis properties of core-shell structured Mg-MFx (M=V, Ni, La and Ce) nanocomposites prepared by arc plasma method, J. Power Sources 366 (2017) 131–142, https://doi.org/10.1016/J.JPOWSOUR.2017.09.015.
[193] Jianxin Zou, Magnesium-Based Energy Storage Materials and Systems, 2024.
[194] S. Long, J. Zou, Y. Liu, X. Zeng, W. Ding, Hydrogen storage properties of a Mg–Ce oxide nano-composite prepared through arc plasma method, J. Alloys Compd. 580 (2013) S167–S170, https://doi.org/10.1016/J.JALLCOM.2013.02.063.
[195] B. Yang, J. Zou, T. Huang, J. Mao, X. Zeng, W. Ding, Enhanced hydrogenation and hydrolysis properties of core-shell structured Mg-MOx (M = Al, Ti and Fe) nanocomposites prepared by arc plasma method, Chem. Eng. J. 371 (2019) 233–243, https://doi.org/10.1016/J.CEJ.2019.04.046.
[196] S. Long, J. Zou, X. Chen, X. Zeng, W. Ding, A comparison study of Mg–Y2O3 and Mg–Y hydrogen storage composite powders prepared through arc plasma method, J. Alloys Compd. 615 (2014) S684–S688, https://doi.org/10.1016/J.JALLCOM.2013.11.159.
[197] Q. Luo, J. Li, B. Li, B. Liu, H. Shao, Q. Li, Kinetics in Mg-based hydrogen storage materials: enhancement and mechanism-NC-ND license, J. Magnesium Alloys 7 (2019) 58–71, https://doi.org/10.1016/j.jma.2018.12.001. http://creativecommons.org/licenses/by-nc-nd/4.0/. PeerreviewunderresponsibilityofChongqingUniversity.
[198] D.J. Han, C. Kwon, Y.J. Cho, K. Sakaki, S. Kim, E.S. Cho, Tailoring hierarchical pore structures in carbon scaffolds for hydrogen storage of nanoconfined magnesium, Chem. Eng. J. 481 (2024) 148451, https://doi.org/10.1016/J.CEJ.2023.148451.
[199] D. Zhou, H. Sun, S. Guo, D. Zhao, J. Li, Y. Zhang, Hydrogen storage properties of Mg-based alloys modified with metal-organic frameworks and carbon-based porous materials: a review and summary, Int. J. Hydrogen Energy 57 (2024) 1373–1388, https://doi.org/10.1016/J.IJHYDENE.2024.01.127.
[200] B.A. Abdulkadir, Zaki RSR. Mohd, A.T. Abd Wahab, S.N. Miskan, A.T. Nguyen, D. V.N. Vo, et al., A concise review on surface and structural modification of porous zeolite scaffold for enhanced hydrogen storage, Chin. J. Chem. Eng. 70 (2024) 33–53, https://doi.org/10.1016/J.CJCHE.2024.03.001.
[201] Z. Ma, Q. Zhang, S. Panda, W. Zhu, F. Sun, D. Khan, et al., In situ catalyzed and nanoconfined magnesium hydride nanocrystals in a Ni-MOF scaffold for hydrogen storage, Sustain. Energy Fuels 4 (2020) 4694–4703, https://doi.org/10.1039/D0SE00818D.
[202] S.H. Kim, Y.E. Jeong, H. Ha, J.Y. Byun, Y.D. Kim, Ultra-small platinum and gold nanoparticles by arc plasma deposition, Appl. Surf. Sci. 297 (2014) 52–58, https://doi.org/10.1016/j.apsusc.2014.01.072.
[203] M. Chen, M. Hu, X. Xie, T. Liu, High loading nanoconfinement of V-decorated Mg with 1 nm carbon shells: hydrogen storage properties and catalytic mechanism, Nanoscale 11 (2019) 10045–10055, https://doi.org/10.1039/C8NR09909J.
[204] H.F. Sun, S.J. Liang, Z.X. Yu, W Bin Fang, Fabrication and hydrogen storage property of Mg-3Ni-2MnO2-nCNTS nanocomposites, 23:1467–1472, https://doi.org/10.1142/S0217979209061111, 2012.
[205] H. Yang, Z. Ding, Y.T. Li, S.Y. Li, P.K. Wu, Q.H. Hou, et al., Recent advances in kinetic and thermodynamic regulation of magnesium hydride for hydrogen storage, Rare Met. 42 (2023) 2906–2927, https://doi.org/10.1007/S12598-023-02306-Z/METRICS.
[206] L. He, X. Shi, X. Li, J. Huang, T. Cheng, X. Wang, et al., Severe plastic deformation through high-pressure torsion for preparation of hydrogen storage materials -A review, Mater. Trans. 64 (2023) 1575–1584, https://doi.org/10.2320/MATERTRANS.MT-MF2022039.
[207] R.B. Figueiredo, T.G. Langdon, Processing magnesium and its alloys by high-pressure torsion: an overview, Adv. Eng. Mater. 21 (2019) 1801039, https://doi.org/10.1002/ADEM.201801039;REQUESTEDJOURNAL:JOURNAL:15272648. PAGE:STRING:ARTICLE/CHAPTER.
[208] E. Rabkin, V. Skripnyuk, Y. Estrin, Ultrafine-grained magnesium alloys for hydrogen storage obtained by severe plastic deformation, Front. Mater. 6 (2019) 480812, https://doi.org/10.3389/FMATS.2019.00240/BIBTEX.
[209] F.J. Antiqueira, D.R. Leiva, T.T. Ishikawa, A.M.J. Junior, W.J. Botta, Severe plastic deformation and additive distribution in Mg-Fe to improve hydrogen storage properties, Mater. Res. 20 (2017) 61–70, https://doi.org/10.1590/1980-5373-MR-2017-0446.
[210] D.R. Leiva, D. Fruchart, M. Bacia, G. Girard, N. Skryabina, A.C.S. Villela, et al., Mg alloy for hydrogen storage processed by SPD, Int. J. Mater. Res. 100 (2009) 1739–1746, https://doi.org/10.3139/146.110225/MACHINEREADABLECITATION/RIS.
[211] J. Huot, Nanocrystalline metal hydrides obtained by severe plastic deformations, Metals (Basel) 2 (2012) 22–40, https://doi.org/10.3390/MET2010022.
[212] J. Huot, N.Y. Skryabina, D. Fruchart, Application of severe plastic deformation techniques to magnesium for enhanced hydrogen sorption properties, Metals 2 (2012) 329–343, https://doi.org/10.3390/MET2030329, 2012;2:329–43.
[213] Tiago Gao, I.A.S. Matias, A.P.C. Ribeiro, L.M.D.R.S. Martins, Application of ionic liquids in electrochemistry—recent advances, Molecules 25 (2020) 5812, https://doi.org/10.3390/MOLECULES25245812, 2020;25:5812.
[214] M. Nava, L.M. Zarnitsa, M.L.Y. Riu, The coupling of synthesis and electrochemistry to enable the reversible storage of hydrogen as metal hydrides, Precis. Chem. (2024), https://doi.org/10.1021/PRECHEM.4C00030/ASSET/IMAGES/LARGE/PC4C00030_0005.JPEG.
[215] Y. Xu, Y. Zhou, Y. Li, Y. Hao, P. Wu, Z. Ding, Magnesium-based hydrogen storage alloys: advances, strategies, and future outlook for clean energy applications, Molecules 29 (2024) 2525, https://doi.org/10.3390/MOLECULES29112525, 2525 2024;29.
[216] L. Ren, Y. Li, N. Zhang, Z. Li, X. Lin, W. Zhu, et al., Nanostructuring of Mg-Based hydrogen storage materials: recent advances for promoting key applications, Nano-Micro Lett. 15 (2023) 1–27, https://doi.org/10.1007/S40820-023-01041-5/FIGURES/4.
[217] Y. Oumellal, M. Courty, A. Rougier, G.A. Nazri, L. Aymard, Electrochemical reactivity of magnesium hydride toward lithium: new synthesis route of nano-particles suitable for hydrogen storage, Int. J. Hydrogen Energy 39 (2014) 5852–5857, https://doi.org/10.1016/J.IJHYDENE.2014.01.119.
[218] D. Vojtěch, B. Šuštaršič, M. Morľaniková, A. Michalcová, A. Veselá, Electrochemical hydriding as method for hydrogen storage? Int. J. Hydrogen Energy 34 (2009) 7239–7245, https://doi.org/10.1016/J.IJHYDENE.2009.06.064.
[219] J.M. Joubert, Thermodynamic modelling of metal–hydrogen systems using the calphad method, J. Alloys Compd. 645 (2015) S379–S383, https://doi.org/10.1016/J.JALLCOM.2014.12.105.
[220] M. Palumbo, E.M. Dematteis, L. Fenocchio, G. Cacciamani, M. Baricco, Advances in CALPHAD methodology for modeling hydrides: a comprehensive review, J. Phase Equilibria Diffus. 45 (2024) 273–289, https://doi.org/10.1007/S11669-024-01113-Y/FIGURES/2.
[221] T. Morino, M. Ode, S. Hirosawa, An explicit integration approach for predicting the microstructures of multicomponent alloys, Nat. Commun. 16 (2025) 1–9, https://doi.org/10.1038/S41467-025-61246-7/TABLES/5.
[222] R. Floriano, G. Zepon, K. Edalati, G.L.B.G. Fontana, A. Mohammadi, Z. Ma, et al., Hydrogen storage in TiZrNbFeNi high-entropy alloys, designed by thermodynamic calculations, Int. J. Hydrogen Energy 45 (2020) 33759–33770, https://doi.org/10.1016/J.IJHYDENE.2020.09.047.
[223] L. Bencze, G. Hasemann, D. Sergeev, V. Motalov, M. Müller, M. Krüger, Thermodynamic properties of refractory Mo-Nb-V-Ti high-entropy alloys (HEAs), J. Alloys Compd. 976 (2024) 173279, https://doi.org/10.1016/J.JALLCOM.2023.173279.
[224] N. Argaman, G. Makov, Density functional theory: an introduction, Am. J. Phys. 68 (2000) 69–79, https://doi.org/10.1119/1.19375.
[225] K. Klyukin, M.G. Shelyapina, D. Fruchart, DFT calculations of hydrogen diffusion and phase transformations in magnesium, J. Alloys Compd. 644 (2015) 371–377, https://doi.org/10.1016/J.JALLCOM.2015.05.039.
[226] A. Kumar, N. Vyas, A.K. Ojha, Hydrogen storage in magnesium decorated boron clusters (Mg2Bn, n = 4–14): a density functional theory study, Int. J. Hydrogen Energy 45 (2020) 12961–12971, https://doi.org/10.1016/J.IJHYDENE.2020.03.018.
[227] E. Halpren, X. Yao, Z.W. Chen, C.V. Singh, Machine learning assisted design of BCC high-entropy alloys for room temperature hydrogen storage, Acta Mater. 270 (2024) 119841, https://doi.org/10.1016/J.ACTAMAT.2024.119841.
[228] J. Hu, J. Zhang, H. Xiao, L. Xie, G. Sun, H. Shen, et al., A first-principles study of hydrogen storage of high entropy alloy TiZrVMoNb, Int. J. Hydrogen Energy 46 (2021) 21050–21058, https://doi.org/10.1016/J.IJHYDENE.2021.03.200.
[229] S.J. Huang, M.P. Mose, S. Kannaiyan, Artificial intelligence application in solid state Mg-Based hydrogen energy storage, J. Compos. Sci. 5 (2021) 145, https://doi.org/10.3390/JCS5060145, 145 2021;5.
[230] K. Batalović, J. Radaković, B. Kuzmanović, M. Medić Ilić, B. Paskaš Mamula, Machine learning-based high-throughput screening of Mg-containing alloys for hydrogen storage and energy conversion applications, J. Energy Storage 68 (2023) 107720, https://doi.org/10.1016/J.EST.2023.107720.
[231] O. Morrison, E. Uteva, G.S. Walker, D.M. Grant, S. Ling, Long time scale molecular dynamics simulation of magnesium hydride dehydrogenation enabled by machine learning interatomic potentials, ACS Appl. Energy Mater. 8 (2025) 492–502, https://doi.org/10.1021/ACSAEM.4C02627/ASSET/IMAGES/LARGE/AE4C02627_0008.JPEG.
[232] T. Liu, L. Xue, B. Cheng, Y. Zhao, M. Paredes, L. Song, et al., Digital twin machine learning-driven alloy digital design for hydrogen storage: a review): Machine learning-driven alloy digital design for hydrogen storage: a review, machine learning-driven alloy digital design for hydrogen storage: a review. https://doi.org/10.1080/27525783.2025.2511889, 2025.
[233] P. Zhou, Q. Zhou, X. Xiao, X. Fan, Y. Zou, L. Sun, et al., Machine learning in solid-state hydrogen storage materials: challenges and perspectives, Adv. Mater. 37 (2024) 2413430, https://doi.org/10.1002/ADMA.202413430;JOURNAL:JOURNAL:15214095;PAGEGROUP:STRING:PUBLICATION.
[234] M. Witman, G. Ek, S. Ling, J. Chames, S. Agarwal, J. Wong, et al., Data-driven discovery and synthesis of high entropy alloy hydrides with targeted thermodynamic stability, Chem. Mater. 33 (2021) 4067–4076, https://doi.org/10.1021/acs.chemmater.1c00647.
[235] M.D. Witman, S. Ling, M. Wadge, A. Bouzidi, N. Pineda-Romero, R. Clulow, et al., Towards Pareto optimal high entropy hydrides via data-driven materials discovery, J. Mater. Chem. A Mater. 11 (2023) 15878–15888, https://doi.org/10.1039/d3ta02323k.

[236] P. Hannappel, M.T. Curnan, G.H. Gu, M. Palumbo, M. Balcerzak, T. Weißgärber, et al., Generalized first-principles prediction of hydrogen para-equilibrium thermodynamics in metal hydrides, npj Comput. Mater. 12 (1) (2025) 21, https://doi.org/10.1038/s41524-025-01902-0, 2025;12.
[237] H.S. AlMatrouk, F. Al-Ajmi, N.S. Do, V. Chihaia, V. Alexiev, The pressure-temperature phase diagram assessment for magnesium hydride formation/decomposition based on DFT and CALPHAD calculation, Mod. Approach. Mater. Sci. (MAMS) 4 (2021) 467–478.
[238] M. Palumbo, E.M. Dematteis, L. Fenocchio, G. Cacciamani, M. Baricco, Advances in CALPHAD methodology for modeling hydrides: a comprehensive review, J. Phase Equilibria Diffus. 45 (3) (2024) 273–289, https://doi.org/10.1007/s11669-024-01113-y, 2024;45.
[239] O. Morrison, E. Uteva, G.S. Walker, D.M. Grant, S. Ling, Long time scale molecular dynamics simulation of magnesium hydride dehydrogenation enabled by machine learning interatomic potentials, ACS Appl. Energy Mater. 8 (2024) 492–502, https://doi.org/10.1021/acsaem.4c02627.
[240] E. Alvares, Y. Shang, A. Santhosh, C. Pistidda, T.W. Heob, B. Sundmanc, P. Jerabeka, M. Dornheima, Ab-initio investigation and thermodynamic assessment of the FeTi hydrogenation, Calphad 9 (2021) 1.
[241] M.D. Witman, N.C. Bartelt, S. Ling, P.W. Guan, L. Way, M.D. Allendorf, et al., Phase diagrams of alloys and their hydrides via On-Lattice graph neural networks and limited training data, J. Phys. Chem. Lett. 15 (2024) 1500–1506, https://doi.org/10.1021/acs.jpclett.3c03369.
[242] P. Zhou, Q. Zhou, X. Xiao, X. Fan, Y. Zou, L. Sun, et al., Machine learning in solid-state hydrogen storage materials: challenges and perspectives, Adv. Mater. 37 (2025) 2413430, https://doi.org/10.1002/adma.202413430.
[243] X. Lu, S. Luo, J. Li, M. Chen, T. Yao, Z. Xu, et al., FIND: a forward–inverse navigation and discovery platform for hydrogen storage alloys powered by data-driven machine learning, J. Mater. Inf. 5 (2025) 48, https://doi.org/10.20517/jmi.2025.56, 2025;5:N/A-N/A.
[244] K. Batalović, B. Paskaš Mamula, M. Medić Ilić, B. Kuzmanović, J. Radaković, B. Stanković, et al., Review of computational advances in tailoring magnesium-hydrogen interactions: atomistic simulations meet machine learning, Int. J. Hydrogen Energy 90 (2024) 114–133, https://doi.org/10.1016/j.ijhydene.2024.09.454.
[245] G. Barkhordarian, T. Klassen, M. Dornheim, R. Bormann, Unexpected kinetic effect of MgB2 in reactive hydride composites containing complex borohydrides, J. Alloys Compd. 440 (2007) L18–L21, https://doi.org/10.1016/j.jallcom.2006.09.048.